Mechanisms of metal dusting corrosion

Hummelshøj, Thomas Strabo; Appel, Charlotte Clausen; Somers, Marcel A. J.; Christiansen, Thomas Lundin; Appel, Charlotte C.

Publication date:
2010

Document Version
Publisher's PDF, also known as Version of record

Mechanisms of Metal Dusting Corrosion

PhD Thesis

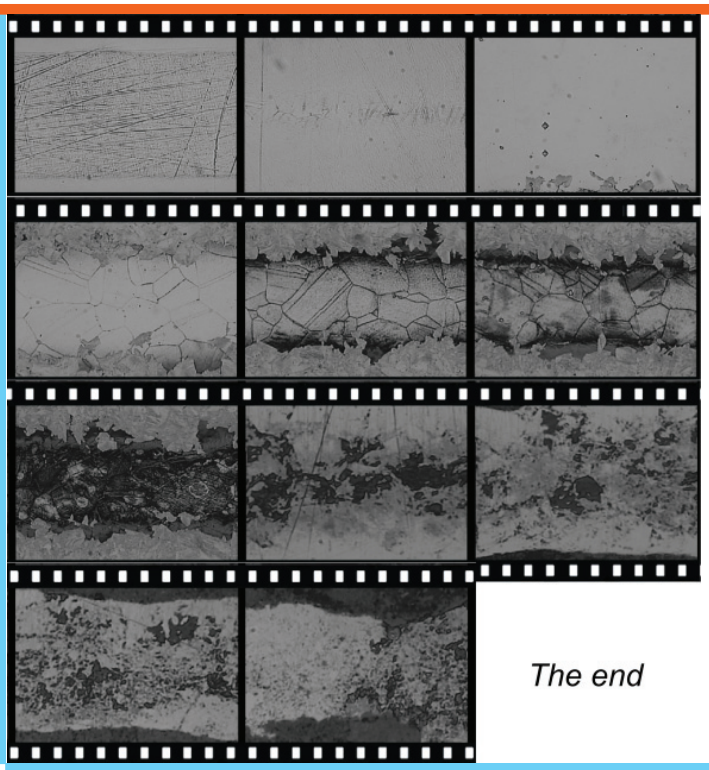

Thomas Strabo Hummelshøj
DCAMM Special Repport No. S115
December 2009

DTU Mechanical Engineering
Department of Mechanical Engineering

Mechanisms of metal dusting corrosion

Thomas Strabo Hummelshøj

Submitted in candidacy
for the degree of Doctor of Philosophy

December 2009

Department of Mechanical Engineering
The Technical University of Denmark

Preface

This thesis is submitted in candidacy for the Ph. D. degree from the Technical University of Denmark (DTU). It is based on the work carried out at the Department of Mechanical Engineering (MEK) from August 2006 to December 2009 under the supervision of Professor Marcel A. Somers, DTU, Thomas L. Christiansen, DTU and Charlotte C. Appel, Haldor Topsøe A/S. Financial support was provided by the Danish Research Council for Technology and Production Sciences under grants 274-05-0230 and 274-05-0367.

Thanks to Marcel Somers, for being an outstanding support. And mentor, not at least. Thank you Thomas Christiansen, for your great cooperation and fruitful discussions, also non-scientific. I thank both of you for your friendship. Thanks to Charlotte Appel, for many good discussions, and many thanks to Haldor Topsøe A/S for letting me use their ESEM. Also thanks to Flemming Grumsen for helping me out with FIB and TEM, and Kristian Dahl for the ThermoCalc calculations and Stine Søndergaard for her contribution to the oxidation experiments. Thank you Jenso for introducing me to Latex. Many thoughts and much love to my family for being there for me.

Abstract

In this thesis the early stages of metal dusting corrosion is addressed; the development of carbon expanded austenite, γ_C, and the decomposition hereof into carbides. Later stages of metal dusting corrosion are explored by a systematic study of stainless steel foils exposed to metal dusting conditions.

The lattice parameter of expanded austenite as a function of interstitially dissolved carbon is determined by carburization of thin stainless steel foils. For the first time this dependency is determined on unstrained austenite at room temperature. It is found that a linear relation holds between the lattice parameter, a, and the occupancy of the octahedral interstices, y_C. Furthermore, the maximum solubility of carbon in expanded austenite is determined at two temperatures. From controlled carburization of stainless steel foils it is found that the precipitation of chromium carbides is unavoidable for carbon contents above approximately 3.5wt% and that the maximum carbon content dissolvable in the f.c.c. lattice is 4.4wt% at 693K. Moreover, from controlled carburization of stainless steel flakes it is found that, the precipitation of chromium carbides is suppressed for carburizing temperatures at 613K and that the maximal dissolvable carbon content in the f.c.c. lattice is 5.3wt% at 613K. The hardness associated with the dissolved carbon, as measured on the metallographic cross sections, is shown to increase linearly with carbon content. Finally, for a low carburizing temperature it is shown that ferrite in heavily deformed stainless steel flakes is transformed to expanded martensite/austenite during low-temperature carburization.

Various experimental procedures to experimentally determine the concentration dependent diffusion coefficient of carbon in expanded austenite are evaluated. The most promising procedure for an accurate determination is shown to be stepwise gaseous carburization of thin foils in a gaseous atmosphere; the finer the stepsize, the more accurate the approximation of the diffusivity. Thermogravimetry was applied to continuously monitor the weight change of thin foils of AISI 316 during carburization in a CO-H_2 gas mixture. It was found that the diffusion coefficient of carbon in expanded austenite increases with carbon concentration.

The decomposition of carbon-saturated expanded austenite was studied by systematic differential thermal analysis on compositionally graded AISI 316L stainless steel powders and flakes. The nature of the decomposition products, carbides of the form $M_{23}C_6$ and M_7C_3, were evaluated by X-ray diffraction, light optical microscopy, scanning electron microscopy and thermodynamic modelling. The decomposition was found to be dependent on several parameters such as thermal history, carbon content, sample geometry and the presence of precursors and possibly the influence of compressive stresses.

A systematic study of AISI 316 stainless steel foils exposed to a mixture of C_2H_2 and H_2 at 823K (550°C) is treated. The applied metal dusting conditions results, firstly, in dissolution of carbon atoms in the surface region by carburization and the formation of carbon expanded austenite, γ_C. Secondly, carbides of the form $M_{23}C_6$ precipitates in the outermost surface region and along grain boundaries. Thirdly, a transformation of the $M_{23}C_6$ carbide layer and simultaneously the supersaturated alloy, into a diverse carbide network. Finally, the foils turn into metal dust accompanied by a thinning and disappearance of the foils. Investigations of TEM samples, prepared by means of FIB, on the carbide network revealed a lamellar structure with carbides and austenite.

Finally, the mutual influence of oxygen and carbon on the metal dusting corrosion is explored. The results indicate that exposure to metal dusting conditions have a detrimental effect on the resistance against oxidation and, conversely, that exposure to oxidation has a detrimental effect on the resistance towards metal dusting. Consequently, a combination of carburizing and oxidizing conditions has a strong mutual catalyzing effect on the metal dusting corrosion.

Resume

I denne afhandling undersøges de tidlige stadier af metal dusting korrosion, herunder dannelsen af kulstof ekspanderet austenit, γ_C, og nedbrydningen heraf i karbider. Senere stadier af metal dusting korrosion er studeret ved en systematisk undersøgelse af tyndfolier af rustfrit stål udsat for metal dusting betingelser.

Gitterparameteren af ekspanderet austenit er bestemt som funktion af kulstof indholdet ved karburering af tyndfolier. Det observeres at gitterparameteren afhænger lineært af kulstofindholdet, y_C. For første gang er denne afhængighed bestemt på spændingsfrie emner ved stuetemperatur. Desuden bestemmes den maksimale opløselighed af kulstof i ekspanderet austenit ved to temperaturer. Fra kontrolleret karburering af tyndfolier, konstateres det, at udskillelsen af karbider er uundgåelig, for kulstofindhold over ca. 3.5wt.%, og at det maksimale kulstofindhold opløst i f.c.c gitteret er 4.4wt.% ved 693K. Desuden fra kontrolleret karburering af flakes, konstateres det at udskillelsen af karbider er undertrykt ved karburerings temperaturer på 613K, samt at den maksimale opløselighed af kulstof i f.c.c gitteret er 5.3wt.% ved 613K. Hårdheden i forbindelse med det opløste kulstof, er vist at øge lineært med kulstofindholdet. Endelig vises det, at for karburering af stærkt deformerede flakes omdannes ferrite til ekspanderet austenite/martensite.

Forskellige eksperimentelle procedurer til eksperimentel bestemmelse af den koncentrationsafhængige diffusion koefficient af kulstof i ekspanderet austenit evalueres. Den mest lovende procedure for en nøjagtig bestemmelse har vist sig at være trinvis karburering af tyndfolier, jo finere trin, jo mere nøjagtig tilnærmelse af diffusionen. Termogravimetri blev anvendt til løbende at overvåge vægtændringer ved karburering af tyndfolier i en CO-H_2 gasblanding. Det blev konstateret, at diffusions koefficienten af kulstof i ekspanderet austenit stiger med kulstof koncentrationen.

Dekomponeringen af kulstof ekspanderet austenit blev undersøgt ved systematisk termisk ananlyse af karburerede pulvere med forskelligt kulstof indhold og kompositions profil. Nedbrydningsprodukterne, karbider af typen $M_{23}C_6$ of M_7C_3 blev evalueret med røngtendiffraktion, lys optisk mikroskopi, scanning elektronmikroskopi og termodynamisk modelering. Dekomponering af kulstof ekspanderet austenite viste sig at være afhængig af faktorer som termisk historie, kulstofindhold, emne geometri, samt tilstedeværelsen af precursors samt muligvis kompositons inducerede spændinger.

En systematisk undersøgelse af tyndfolier udsat for en blanding af C_2H_2 og H_2 ved 823K (550°C) er behandlet. De anvendte metal dusting betingelser resulterer, dels i opløsning af kulstofatomer i overfladen regionen ved karburering og dannelsen af kulstof ekspanderet austenit, γ_C. Dernæst udskillelsen af karbider af typen $M_{23}C_6$ i den yderste overflade region og langs korn grænser. Dernæst sker en transformation af $M_{23}C_6$ karbidlaget og samtidig den overmættede legering, i et mangfoldigt karbid-netværk. Endelig forvandles de karburerede folier til metalstøv ledsaget af en udtynding og forsvinden af folierne. Undersøgelser af TEM prøver, der er udarbejdet ved hjælp af FIB, afslører en lamelagtig struktur med karbider og austenit.

Endelig er den gensidige påvirkning af ilt og kulstof på metal dusting korrosion udforsket. Resultaterne tyder på, at eksponering for metal dusting betingelser har en negativ indvirkning på prøvens modstand mod oxidation, og omvendt, at eksponering for oxidation har en skadelig virkning på prøvens modstand mod metal dusting. Det kan dermed sluttes at en kombination af karburering og oxiderende betingelser har en stærk gensidig katalyserende effekt påmetal dusting korrosion.

Lyngby, December 22, 2009
Thomas Strabo Hummelshøj

Contents

List of Tables

List of Figures

1 Introduction

1.1 Metal dusting - definition and problem

Fe-based (steel) and Ni-based high chromium alloys are widely applied as high temperature materials in industries operating in environments of high-carbon activity. All Fe-based and Ni-based metals in high temperature process equipment that get into contact with carbon bearing gases are subjected to carburization, i.e. dissolution of carbon in the alloy and the development of carbides. Generally, such carburization may lead to a very aggressive corrosion phenomenon known as metal dusting (MD). Metal dusting can be described as catastrophic carburization which takes place in carbon-supersaturated gaseous environments containing CO, H_2 and/or hydrocarbons (C_xH_y), wherein the carbon activity a_c of the gas exceeds 1 (with graphite as a reference). Under such conditions it is thermodynamically possible for the gas to form carbon (graphite), and initiate metal dusting. In practice, the phenomenon has been reported to occur in the approximate temperature range 673K-1073K when the carbon potential in the gas is well above unity [4, 5, 6]. The metal dusting corrosion manifests itself as a mixture of fine carbides, metal particles and carbon dust - hence the term, metal dusting. The metal dusting corrosion can be in the form of pitting and general metal wastage.

Metal dusting is experienced in many industries where metallic alloys are used as structural components at elevated temperatures in environments of high-carbon activity. Synthesis (syngas) plants in which methane and other hydrocarbons are reformed to produce hydrogen, methanol and ammonia are major examples of where metal dusting is a problem. Also in the petrochemical industry and particularly, in the reforming units, metal wastage and metal dusting is a severe problem. Other processes wherein metal dusting occurs are: nuclear plants that employ carbon monoxide for cooling; recycle-gas loop equipment of coal-gasification units; tubes of fired heaters handling hydrocarbons, and in fuel cells using molten salts plus hydrocarbons. In the steel industry, metal dusting has occurred in plants with equipment for the direct reduction of iron ore and in blast furnaces. A consequence of the metal dusting process is that process equipment or pipes will be destroyed within relatively short time.

1.2 Metal dusting studies - state of the art

Metal dusting has received increasing attention over the last decade. A wealth of literature references can be given wherein the phenomenon is reported to occur in a large range of Fe- and Ni-based alloys and in various gaseous atmospheres. Various (mostly futile) solutions have been suggested for enhanced MD resistance, but the holy grale has not been found yet. Surprisingly, very few systematic investigations of the mechanism and the kinetics can be found. A few years ago Zeng et al. (2002) summarized the situation of MD research: Metal dusting has been studied for more than 50 years, but the mechanisms are not fully understood [7]. There are serious gaps in the understanding of MD mechanisms, which need to be addressed in order to advance materials development. Metal dusting studies focus on carbon-metal reaction thermodynamics and kinetics, as well as micro mechanisms that influence diffusion through surface layers. Research is broadly categorized in: pure metals, iron-based and nickel-based alloys. To summarize the effort to understand and prevent metal dusting, research programs have become world wide

extending from pre-1999 efforts centred primarily in Germany and the United States, now to several Scandinavian and European countries, New Zealand, Australia, Japan and China.

1.3 Classification of MD-mechanisms

The phenomenon of MD can be divided into three main mechanisms denoted Type I, Type II and Type III. In brief Type I involves decomposition of metastable cementite, Type II, may be described as disintegration of a carbon supersaturated phase by internal graphitization and Type III which involves selective oxidation of alloyed carbides.

1.3.1 Metal dusting in pure iron and low alloyed steels - Type I

Early research by Hochman and coworkers [8] on pure iron identified the role of metastable carbide, M_3C, in initiating metal dusting. Later work by Grabke and coworkers expanded on the formation-dissociation mechanism of the M_3C carbide [6, 9]. The most well known metal dusting mechanisms were proposed by Grabke for iron and Fe-based low alloys [5]. For the temperature range of 673K-923K and with a gas mixture consisting of H_2, CO and H_2O, the suggested mechanism, referenced to as MD mechanism Type I, develops as follows [4]:

1. Carburization of the meal phase by dissolution of carbon and oversaturation of the metal, i.e. $a(C) > 1$ in the metal with respect to graphite (perfect carbon lattice), see Figure 1.1a.

2. Precipitation of cementite Fe_3C at the surface and growth into the supersaturated metal phase, Figure 1.1b. The cementite acts as a barrier for further carbon ingress.

3. Nucleation of graphite on the cementite layer, Figure 1.1c. As soon as graphite develops the carbon activity drops to unity, whereby the metastable cementite decomposes near the cementite-graphite interface into pure Fe and graphite according to $Fe_3C \rightarrow 3\ Fe + C$.

4. From this point the steady state process has started when graphite continues to grow into the Fe-matrix which may be described as disintegration of supersaturated ferrite (or austenite) by graphite formation, denoted the Type II mechanism.

5. The graphite may establish fast diffusion paths for metal atoms along the widely spaced lattice planes of the hexagonal graphite lattice. This has been shown for pure Ni-particles during formation of carbon nanofibres [10]. At the surface, these metal particles catalyze carbon decomposition of the gas to form highly structured carbon nano-filaments which easily are removed as dust by the gas flow.

Many new micro-processes focusing on the catalysis step involving Fe_3C, have been put forward [11, 12, 13, 14, 15, 16, 17, 18] since the classic work by Grabke and others. Accordingly, there is disagreement about the mechanistic steps that affect the reaction rates of metal dusting.

1.3.2 Metal dusting in pure nickel and nickel base alloys (low Cr content) - Type II

In nickel and Ni-base alloys another mechanism is proposed by Pippel et al. [19], Grabke [5] and Schneider et al. [20] which involves the diffusion of carbon into the nickel lattice followed by graphite precipitation within the bulk. This leads to small Ni-particles embedded in graphite. Research indicates that carbon directly forms graphite or unstable Ni_3C [21], which immediately dissociates into graphite and Ni [22]. Ni atoms agglomerate at catalytic sites and on the outer surface of graphite to form Ni particles, which catalyze the formation of filamentous carbon and are carried away. Hence, graphite growth may start from the surface, in grain boundaries or in the bulk [21, 19]. The mechanism is referred to as MD mechanism Type II (see Figure 1.1h).

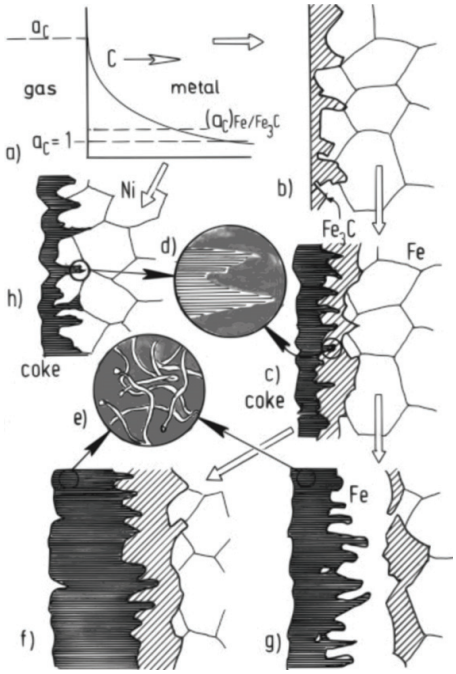

Figure 1.1: Schematic illustration of the processes in metal dusting of iron, low allow steels and nickel [4].

1.3.3 Metal dusting on austenitic stainless steels and Ni-base alloys - Type III

For Fe-based high alloy steels and Ni-base alloys some additional features are to be considered in the mechanism and kinetics of metal dusting. Grabke and coworkers extended their research to the mechanistic aspects of alloy corrosion, in particular, the break-up of surface oxide films in initiating localized attack [9]. Among researchers, the effect of alloying additions is fairly consistent; the presence of Cr and Al, if in high enough concentration, form stable oxide(s) on the surface [23]. The oxide film acts as a barrier for the transfer of carbon from an adsorbed state at the surface to a dissolved state in the solid, thus protecting the alloy against carburization. Metal dusting initiates only when and if the protective oxide film is damaged or becomes defective [24, 25, 26]. For Ni and Fe alloys with a high Cr content, a third mechanism has been suggested to work in conjunction with Type I and Type II. The mechanism has initially been indicated by several researchers which have discussed the possible active role of oxygen during metal dusting conditions in combination with high steam contents of 30 to 50% [27, 28]. The phenomenon was first mentioned by Schmid et al. [29] in gas atmospheres with low steam content (23%). The mechanism was later extensively investigated by Szakalos [30, 13]. De Bruyn et al. [31] took the idea further and drew attention to the occurrence of internal oxidation during metal dusting, at least in reformer gas with high water vapour content, and suggest that the phenomenon may also occur with low water vapour content.

The Type III mechanism is based on the concept of active corrosion under the influence of both carbon and oxygen. Carbon reacts with metal and metal carbides are formed. These carbides dissolve and oxidise selectively and free carbon is released which forms carbides/graphite and so forth. The possible active role of oxygen during metal dusting is the fundamental concept of, according to Szakalos classification [32], the Type III metal dusting mechanism which develops as follows:

1. The protective oxide scale fails at some weak point in the surface.
2. Carburization of the metal phase by dissolution of carbon into the metal surface.
3. Oversaturation of the metal matrix with dissolved carbon.

4. Carbon reacts with the alloying elements which initially form $M_{23}C_6$ carbides, then M_7C_3 and M_3C carbides form at higher carbon activity.

5. All carbides $M_{23}C_6$, M_7C_3 and M_3C are oxidized by selective oxidation under formation of spinels and other oxides and free carbon is released which forms carbides/graphite and so forth.

6. Simultaneously the supersaturated austenite is disintegrated by graphite formation into small austenitic metal dust particles (Type II mechanism).

Depending on alloy composition, temperature and gas environment the resulting sub-surface structure may vary significantly. For example in a Ni-base alloy exposed at 813K in a methanol plant, a discontinuously precipitated carbide network in the austenite on which the oxidation takes place develops. Alternatively, in an AISI 304L type stainless steel exposed at 923K in a $CO+H_2$-containing gas mixture, a Cr-depleted carbide-free austenite zone with graphite channels develops [32].

Summarizing, three main stages can be distinguished in the metal dusting mechanism of high chromium austenitic alloys. Firstly, the protective chromium oxide layer on the Fe-based and Ni-based alloys is attacked locally. The pit initiation, which implies local breakthrough of the (supposed protective) oxide layer, allows incorporation of carbon in the underlying metal. Secondly, carburization, i.e. reaction between the components of the alloys and carbon, ultimately leading to the formation of carbides. Finally, the dissolution of the alloyed carbides by selective oxidation in conjunction with a disintegration of the supersaturated austenitic lattice due to the graphitisation process. Consequently, the metal is transformed into a mixture of small metal particles, graphite, carbides (chromium), spinels and carbon nanotubes

1.4 Carburizing kinetics - Expanded austenite (γ_C)

Austenitic stainless steels are widely applied for their corrosion-resistant performance, both at atmospheric temperature and at elevated temperatures. Engineering these materials towards an improvement of the wear resistance while maintaining the corrosion resistance has been accomplished by deliberately dissolving large amounts of carbon into the surface by carburization at a temperature below, say <823K, at which effectively no carbides develop [33, 34]. The resultant carburized layer is characterized by a colossal supersaturated solid solution of carbon atoms residing in the octahedral interstices of the austenite lattice. The carburized zone of so-called expanded austenite has a high hardness and favourable anti-galling and wear resistant properties combined with the unaffected anti-corrosion properties. An AISI 316 stainless steel foil carburized in C_2H_2 and H_2 at 743K and the associated carbon expanded layer in the surface is depicted in Figure 1.2.

Expanded austenite was first recognized in the mid-80′es by Ichii et al. [35] and was at that time designated S-phase. The designation S-phase relates to the unidentifiable peaks in the X-ray diffraction patterns (arbitrarily) named S1-S5, i.e. peaks not listed in the ASTM index. In a recent study, homogeneous powder of stress-free nitrogen expanded austenite with different nitrogen contents was obtained by gaseous nitriding. From X-ray diffraction analysis it was possible to unambiguously prove that the expanded austenite has a face centred cubic structure (f.c.c) and that stacking faults contribute to systematic deviations of the X-ray line profiles from their fault free positions [36].

During carburization of stainless steel at temperatures sufficiently low to prevent the carbide development within reasonable carburizing time, i.e. under para-equilibrium conditions, a carbon concentration profile develops in the material, such that the highest carbon concentration occurs adjacent to the surface. The expansion of the lattice, caused by the misfitting, interstitially dissolved carbon atoms, is directly proportional to the carbon concentration. Consequently the lattice expansion is largest adjacent to the surface. The lattice expansion decreases similarly to the carbon concentration traversing deeper into the material. In expanded austenite layers on carburized austenitic stainless steel, compressive stresses of 2-3 GPas develop as a consequence of the carbon profile. A thorough recent investigation and quantification of compressive stresses of

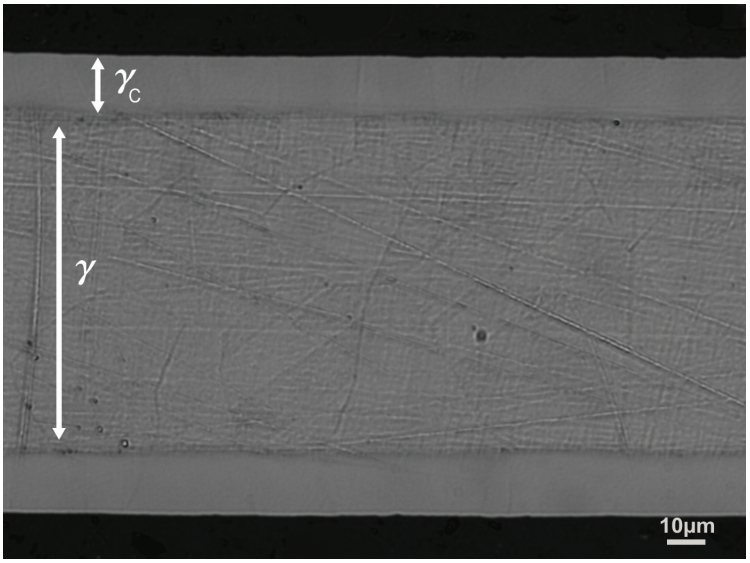

Figure 1.2: The development of carbon expanded austenite, γ_C, by carburization of an AISI 316 stainless steel 100μm foil in a mixture of C_2H_2 and H_2 at 743K.

this magnitude was presented in [37]. The associated expansion of the lattice by the interstitial dissolved carbon atoms is visualized in Figure 1.3, were stainless steel flakes have been carburized in C_2H_2 and H_2 at 613K. The figure illustrates that the carburized areas, marked γ_C, appear thicker in the light optical image as compared to the uncarburized austenitic lattice, γ.

Expanded austenite is thermodynamically metastable and will decompose upon thermal exposure leading to the formation of carbides. The thermal stability of expanded austenite with respect to carbide formation and associated Cr depletion of the surrounding matrix is of particular interest to maintain the advantageous corrosion properties of stainless steel as well as preventing the unwanted catastrophic corrosion, metal dusting. The carbides anticipated to develop upon the decomposition of expanded austenite are of type $M_{23}C_6$, M_7C_3 and M_3C_2, where M stands for a mixture of Fe and Cr atoms. Recently, the development of a M_5C_2 type (Hagg) carbide was reported [38]. Hitherto, the decomposition of carbon expanded austenite has not been associated with the metal dusting corrosion mechanism. Reported research has neither included the occurrence and subsequent decomposition of carbon expanded austenite, nor a description of the actual formation of carbides. Specifically the decomposition sequence in carbon expanded austenite has not been investigated. The process subsequent to the onset of metal dusting is in general referred to as ′carburization and carbide formation′. In order to be able to make reliable forecasts of the time to the onset of metal dusting, and possibly allow for a thorough investigation of the parameter influencing the kinetics of the (catastrophic) carburizing process it is necessary to include the development and decomposition of carbon expanded austenite.

1.5 This work

One of the inherent complications investigating the kinetics of metal dusting is distinguishing between the kinetics of pit initiation (the incubation time) and the carburizing kinetics after the development of pits. Also the wide range of incubation times, and consequently, specimen exposure times ranging from hours to several years further complicates the effort. Another complication by investigating the kinetics of carburizing in the second stage and the coking in the final stage is the application of straightforward techniques for the investigation of changes in the material microstructure, because of localized attacks. The microstructure changes are typically based on cross section investigations of single pits [39]. In the present study, a different approach

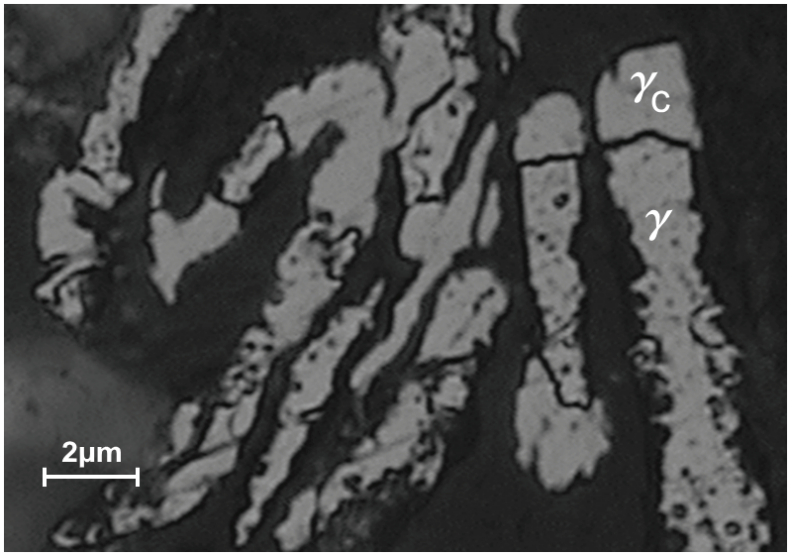

Figure 1.3: The development of carbon expanded austenite, γ_C, by carburization of AISI 316L stainless steel flakes in a mixture of C_2H_2 and H_2 at 613K.

to the investigation of metal dusting is followed. A recently patented method [40] developed for surface hardening of stainless steels is applied to "bypass" the incubation time. The advantage of this method is that the passive oxide film covering the stainless steel surface is removed instantaneously during the gaseous treatment. Consequently, the kinetics of pit initiation and carburizing kinetics are separated and can be studied individually. Another advantage is the non-stochastic attack, which practically means that the entire surface acts as a pit, which dramatically facilitates microstructure investigations. The reducing atmosphere further simplifies matters, in that the competition between metal dusting and oxidation which introduce complicating kinetics is avoided. However, it is realized that in addition to its role in forming protective oxide scales, oxygen may play an active role in the metal dusting mechanism. As Schmid et al. expressed "The hypothesis of alternating carburizing and oxidizing conditions is in our view a promising starting point for the elucidation of additional facets of the metal dusting mechanism" [29]. The hypothesis is tested and discussed in this thesis. Finally, the strongly accelerated process conditions featured by the patented method, which is due to a combination of superior surface activation and high carburizing potential, enables an actual investigation of the kinetics of carburizing and comparison of various alloy compositions, which has hitherto been obscured by the wide range of incubation times. Finding optimal alloys by trial and error is a time consuming strategy. Accordingly, the spectacularly reduced treatment periods allow targeted optimization of the alloys composition.

List of publications

Paper I
Determination of concentration dependent diffusion coefficients of carbon in expanded austenite.
T.S. Hummelshøj, T.L. Christiansen and M.A.J. Somers
Diff. Defect Forum, 2008, 273- 276, 306-311.

Paper II
Low temperature thermochemical treatment of stainless steel; bridging from science to technology.
T.L. Christiansen, T.S. Hummelshøj and M.A.J. Somers
Dansk Metallurgisk Selskab - Vintermødet (2010)

Paper III
Towards commercialization of fast gaseous nitrocarburising of stainless steel.
T.S. Hummelshøj, T.L. Christiansen and M.A.J. Somers
Dansk Metallurgisk Selskab - Vintermødet (2010)

Paper IV
Expanded austenite; crystallography and residual stress.
T.L. Christiansen, T.S. Hummelshøj and M.A.J. Somers
Surface Modification Technologies XXII, Proc. 22nd Inter. Conf. Surface Modification Technologies, Eds. T.S. Sudarshan, P. Nyln, 2009, pp. 199-206.

Paper V
Controlled dissolution of carbon in AISI 316 stainless steel.
T.S. Hummelshøj, T.L. Christiansen and M.A.J. Somers
To be submitted.

Paper VI
Decomposition kinetics of carbon expanded austenite.
T.S. Hummelshøj, T.L. Christiansen and M.A.J. Somers
To be submitted.

Paper VII
The influence of Mo on the decomposition kinetics of carbon and nitrogen expanded austenite.
T.S. Hummelshøj, T.L. Christiansen and M.A.J. Somers
To be submitted.

Paper VIII
Systematic studies of metal dusting corrosion.
T.S. Hummelshøj, T.L. Christiansen and M.A.J. Somers
To be submitted.

Paper IX
On the mutual influence of oxygen and carbon on metal dusting corrosion.
T.S. Hummelshøj, T.L. Christiansen, S. Søndergaard and M.A.J. Somers
To be submitted.

2 Experimental

Experiments presented in this thesis are subdivided in two areas; i) carburization of foils, flakes and powders for assessing thermodynamic parameters and kinetic data and ii) metal dusting experiments with and without pre-oxidation. A thermal analyzer was applied exclusively for the experiments in i). For the experiments in ii) the thermal analyzer and a dedicated metal dusting furnace were applied. Also the environmental scanning electron microscope (ESEM), a FEI XL 30, at Haldor Topsøe A/S was applied for the experiments in ii). For transmission electron microscopy (TEM), a Jeol 3000, located at Materials Research Division, Risø National Laboratory for Sustainable Energy (RISØ-DTU), was applied. Preparation of TEM samples by focused ion beam lift-out was carried out at Center for Electron Nanoscopy at DTU (CEN), with a FEI Quanta 200 3D FIB SEM Dual Beam instrument.

In this chapter, firstly the thermodynamics for gaseous carburizing are given followed by a short introduction to Thermogravimetry. Secondly, a detailed description of some relevant practical aspects related to the experimental work are provided and discussed.

2.1 Thermodynamics of gaseous carburizing

Carburizing in a gas mixture of C_2H_2 and H_2 where carbon is dissolved into the solid state occurs according to the reaction:

$$C_2H_2(g) \rightarrow 2[C] + H_2(g), \tag{2.1}$$

where $[C]$ represents C in solid solution. The equilibrium constant, K_1, of equilibrium 2.1 is expressed by the activities, $a()$, of the involved species. At low pressures (1 atmosphere) the fugacities, $f()$, are approximately equal to their partial pressures, $P()$, of the gaseous components:

$$K_1 = \frac{a(C)^2 \cdot f(H_2)}{f(C_2H_2)} = \frac{a(C)^2 \cdot P(H_2)}{P(C_2H_2)}. \tag{2.2}$$

It is noted that K_1 does not depend on the total pressure other than by the pressure dependence of $a()$. If local equilibrium exists between the gas phase and the surface of the solid solution of C, then the carbon activity, $a(C)$, is given by:

$$a(C) = \sqrt{K_1 \frac{P(C_2H_2)}{P(H_2)}}. \tag{2.3}$$

The value of the equilibrium constant K_1 is found considering the change in Gibbs energy associated with the reaction. Carburizing in a gas mixture of CO and H_2 the heterogeneous water-gas shift reaction can occur:

$$CO(g) + H_2(g) \rightarrow [C] + H_2O(g), \tag{2.4}$$

where [C] denotes carbon in solid solution. The equilibrium constant K_2 of equilibrium 2.4 is given by:

$$K_2 = a(C) \cdot \frac{P(H_2O) \cdot P(0)}{P(CO) \cdot P(H_2)}, \tag{2.5}$$

where $P(0)$ is the total pressure. And the carbon activity:

$$a(C) = K_2 \cdot \frac{P(CO) \cdot P(H_2)}{P(H_2O) \cdot P(0)}. \tag{2.6}$$

Note that in contrast to K_1, K_2 is directly dependent on the total pressure $P(0)$. The partial pressure of water vapour was not determined in this work, hence K_2 could not be determined.

2.2 Thermal analysis

2.2.1 Thermogravimetry (TGA)

Thermogravimetry is a method where, changes in the mass of a sample are continuously measured while the sample is subjected to a controlled temperature program. Generally, for kinetic analysis the temperature program is a linear increase in temperature, but isothermal studies can also be carried out. TGA is inherently quantitative, and gives no direct chemical information. However, reactions/transitions like desorption, absorption, sublimation, vaporization, oxidation and decomposition are generally associated with a change in mass and may therefore be monitored. The method of thermogravimetry provides information on the composition, thermal stability against thermal decomposition [41], and may be considered as a powerful thermal analysis technique in the present project.

Several factors influence the shape of the TGA curve (mass versus time). The primary factors are heating rate and sample size. An increase in heating rate tends to increase the temperature at which the maximum transformation occurs. Endothermic and exothermic reactions occurring in the sample cause deviation from the temperature program. This effect gets more pronounced as sample mass increases. The particle size of the sample material, the way in which it is packed, the crucible shape, and the gas flow rate can also affect the progress of the reaction. Consistency in the experimental details normally results in good repeatability.

2.2.2 Differential Thermal Analysis (DTA)

With differential thermal analysis (DTA), reactions/transitions not associated with a weight change are measurable. The technique involves the monitoring of the temperature difference $T_D(T_s - T_r)$ between the sample of interest and an inert reference material on simultaneous heating, or cooling, at a predetermined rate. The temperature difference is then plotted against time, or against temperature. Compared to thermogravimetry, more physical and chemical processes may be observed using differential thermal analysis. Reactions giving rise to such peaks in the DTA curve include: phase change, fusion, vaporization, sublimation, desorption, adsorption, oxidation, reduction reactions, dehydration, dissociation or decomposition reactions, gaseous reduction, crystalline transitions and other chemical reactions [42]. Both solids and liquids can be studied by differential thermal analysis. The principle of a DTA apparatus is shown in Figure 2.1a. Temperature changes occur in the sample due to endothermic or exothermic transitions or reactions. As enthalpic changes occur, T_D will be positive if the process is exothermic and negative if it is endothermic. An example of a DTA curve showing exothermic and endothermic transitions or reactions is shown in Figure 2.1b. The curve represents the isochronal annealing of a carburized stainless steel 20μm powder. Besides the DTA curve, the TGA and the differentiated TGA curves are also included. According to the DTA curve, three exothermic reactions occur around 923K, 1023K and 1103 K. Since no mass loss is associated, these reactions can solely be ascribed to transitions within the material. At 1153K, an endothermic reaction is detected. Comparing the DTA curve with the differentiated TGA curve shows that the position of the minimum in the differentiated TGA curve coincides with the endothermic reaction at 1153K. Accordingly, the endothermic peak is attributed to the release of carbon from the sample powder

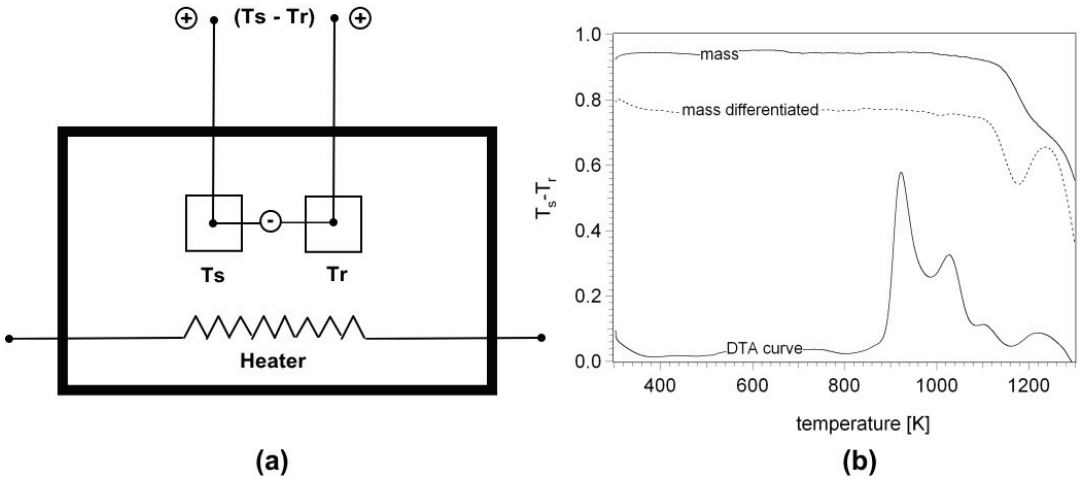

Figure 2.1: (a) principle of a DTA apparatus, (b) DTA, TGA and differentiated TGA curves during isochronal annealing of carburized AISI 316L 20μm powder in H_2.

and presumably due to development of CH_4 since the isochronal heating was performed in an atmosphere of H_2.

The shape of a DTA peak depends on sample weight and the heating rate used. Lowering the heating rate improves resolution and peaks representing maximum transformation rate are typically shifted towards lower temperatures. The area under the DTA curve is proportional to the corresponding heat of reaction, and therefore also to the sample weight. Hence, a larger sample mass improves the DTA signal and higher resolution is obtained. However sample mass is a compromise, since large samples are difficult to heat homogeneously leading to broader peaks, corresponding to a range of transformation temperatures. Figure 2.2 illustrates the effect of varying the heating rate, while keeping the sample mass constant. The reaction observed is the decomposition of carbon expanded austenite into carbides in stainless steel powder.

Kinetics from differential methods

The influence of heating rate on the peak shape and peak position can be used for kinetic analysis. One approach to deduce kinetic parameters from DTA curves is to relate the peak temperature/temperature of maximum transformation rate, T_m, at different heating rates, ϕ, to the activation energy of the transition. Almost all of the kinetic methods used in DTA are based on [42]:

$$\frac{d\alpha}{dt} = f(\alpha, T), \tag{2.7}$$

where $\frac{d\alpha}{dt}$ is the rate of reaction, $f(\alpha, T)$ is a function of the amount reacted, and T is the abolute temperature at time t. The activation energy E and the pre-exponential factor (frequency factor), A, may be calculated by the commonly used Kissinger method [41, 42]. Starting from the fundamental kinetic equation:

$$-\frac{1}{V} \cdot \frac{dx}{dt} = A \cdot e^{\frac{-E}{RT}} \cdot \left(\frac{x}{V}\right)^n, \tag{2.8}$$

where x is the number of particles of the starting substance, n is the reaction order and V is the volume. The equation applies for all temperatures, T, if T and x are measured simultaneously. Assuming that the temperature increases at a constant rate, $\frac{dT}{dt}$, the reaction rate increases to a maximum when $\frac{d}{dt}\left(\frac{dx}{dt}\right) = 0$, hence:

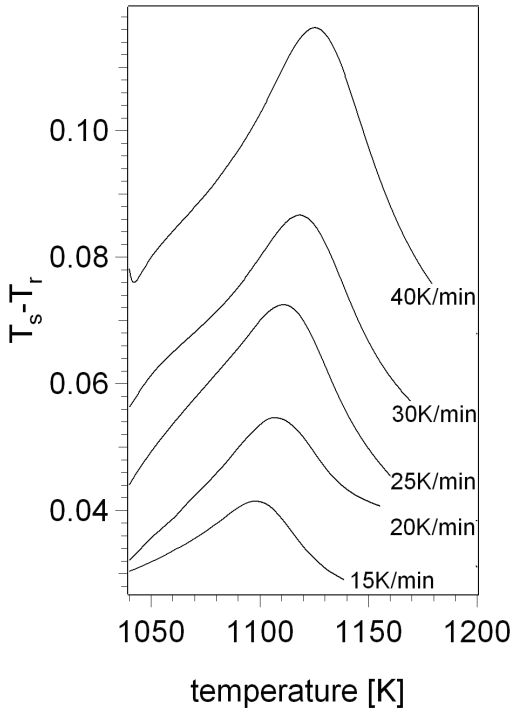

Figure 2.2: The influence of varying the heating rate on DTA peak position and intensity. The sample mass is constant.

$$\frac{d}{dt}\left(\frac{dx}{dt}\right) = \frac{dx}{dt}\left[\frac{E\cdot\frac{dT}{dt}}{R\cdot T^2} - A\cdot n\cdot\left(\frac{x}{V}\right)^{n-1}\cdot e^{\frac{-E}{RT}}\right] = 0, \tag{2.9}$$

and rewriting:

$$\frac{E\cdot\frac{dT}{dt}}{R\cdot T_m^2} = A\cdot n\cdot\left(\frac{x}{V}\right)_m^{n-1}\cdot e^{\frac{-E}{RT_m}}, \tag{2.10}$$

where T_m is the temperature at which the reaction rate is greatest. $\left(\frac{x}{V}\right)_m$ is the amount of substance which remains undecomposed at the moment of maximum reaction rate. Integration and solving for $n = 0$ and $n = 1$ gives:

$$n\cdot\left(\frac{x}{V}\right)_m^{n-1} = 1 + (n-1)\cdot\frac{2\cdot R\cdot T_m}{E}. \tag{2.11}$$

Assuming that T_m is independent of heating rate, which also means that $n\cdot\left(\frac{x}{V}\right)_m^{n-1}$ is independent of heating rate and is approximately equal to unity, then substitution into Equation 2.10 and taking logarithms and differentiating finally gives:

$$\frac{-E}{R} = \frac{dln\left(\frac{dT/dt}{T_m^2}\right)}{d\left(\frac{1}{T}\right)}, \tag{2.12}$$

Several DTA curves are recorded at different heating rates, $\frac{dT}{dt}$, and values of T_m are determined. A plot of $\ln(\frac{dT}{dt}/T_m^2)$ versus $1/T_m$ should give a straight line, of which the slope is equal to $\frac{-E}{R}$ and the activation energy, E, can be obtained.

2.2.3 Thermal analyser

For thermal analysis a thermobalance is applied for continuous measurement of weight changes as a function of temperature or time. The essential components of a thermobalance, are a microbalance, a furnace, a temperature programmer, a sample holder, an enclosure for establishing the required atmosphere, and a means of recording and displaying the data. Measurements can be performed in a chosen atmosphere with or without flow. However, it is recommended to use a constant flow to obtain a more controlled and stable gas environment around the sample. The temperature is measured by a thermocouple close to the sample.

The thermobalance applied in the present work was a Netzsch STA 449C Jupiter thermal analyzer which allows simultaneous thermogravimetric analysis (TGA) and differential thermal analysis (DTA). Gasses are led into the lower section of the furnace chamber via electronic gas flow controllers. The gas flow can be varied in the range 1.0 to 100 mL/min with a minimum adjustable step of 0.4 mL/min. The thermobalance requires a flow of inert gas to protect the electronics from reactive gasses (e.g. C_2H_2). Typically N_2 or Ar with a flow rate of 5 mL/min was used for this purpose. The protective gas is mixed with the reactive gas at the lower section of the furnace chamber, hence the sample is exposed to both reactive gas and protective gas. After the gas has passed the outlet in the upper part of the furnace, gas is let through water-free oil to prevent any accidental backward flow of oxygen. The furnace temperature operating range is room temperature to 1873 K and measured with type S thermocouples (Pt10%Rh-Pt). Heating rates are within the range 0.1 to 50 K/min. Balance sensitivity is 0.1μg, with a total capacity of 5g. The sample holder material and crucibles are made of alumina. The furnace cover of the thermobalance is water cooled in order to keep the ambient temperature constant. The connected vacuum pump is able to reduce the pressure to 8 mbar. The instrument is controlled by a computer from where temperature programs are constructed. The instrument is depicted in Figure 2.3.

Figure 2.3: The Netzsch STA 449C Jupiter thermobalance.

2.3 Carburizing experiments

Different sample geometries were used in the investigations presented in this thesis; powders with grain sizes ranging from 5μm to 150μm, thin flakes with thickness 1.2μm, foils with thicknesses from 7.5μm to 100μm and finally bulk samples were used. The investigated materials are stainless steel AISI 316 and AISI 316L. The nominal composition of the materials is given in Table 2.1.

Alloy	C	Cr	Ni	Mo	Mn	Si	Fe
AISI 316	0.08 max	16-18	10-14	2-3	2 max	1 max	Bal.
AISI 316L	0.03 max	16-18	10-14	2-3	2 max	1 max	Bal.

Table 2.1: Nominal composition of the investigated stainless steels in wt.% (balance Fe) applied in this thesis.

2.3.1 Surface activation

Generally, samples were annealed before the carburizing experiments. This was done to ascertain the same material conditions in each experiment. During austenitizing, samples were heated to 1353K in H_2 at a heating rate of 20K/min and immediately cooled upon reaching this temperature. Cooling rates were approximately 50K/min. The austenitizing procedure was either performed as a step before the actual experiment in the thermobalance, or performed in an external furnace. During austenitizing in the thermobalance, the gas flow of H_2 was not known as the electronic mass flow controller was fully opened (thus not controllable). During austenitizing in the external furnaces the gas flow of H_2 was 2 l/min. During austenitizing deformation-induced martensite, introduced upon the manufacturing of the foils, flakes or powders, was completely removed and transformed into austenite as confirmed by X-ray diffraction. Some difficulties were experienced during austenitizing of the micrometer thin flakes. Sintering occurred at temperatures above 1273K, thus for the flakes the austenitizing temperature did not exceed 1273K.

Under practical circumstances the protective oxide scale on stainless steel delays the onset of the carburizing reaction, which implies that deliberate carburization of stainless steel surfaces requires an activation step wherein the protective oxide layer is removed or by-passed. The removal of the protective oxide layer on the powders and flakes was another objective of the austenitizing procedure in H_2. Due to the dense packing of the powders and flakes, oxygen impurities in the gas were not able to repassivate the surface during cooling to carburizing temperature. A similar surface activation of foils was not possible. Therefore, after austenitization of the foils, a patented pre-treatment method was applied [43]: the native oxide layer covering the stainless steel surface was electrochemically replaced by a thin Ni-deposit in a Woods nickel bath, consisting of $NiCl_2$, $NiSO_4$ and H_2SO_4. The metal layer prevents the surface from forming a protective oxide scale and catalyzes the surface reaction necessary to liberate carbon atoms from carbon-containing species in the gas mixture. The thickness of the deposited Ni layer was in the order of 20 nm, as calculated from the total electric energy transferred, and contributes to maximally 0.5 % of the total sample mass. The solubility of carbon in the deposited Ni layer is negligible compared to the solubility in austenite. The surface activation made it possible to conduct carburizing experiments in CO atmospheres.

2.3.2 Process parameters

Optimal flow conditions were found to be foils hanging vertically from a specially designed holder in the thermobalance. This setup in combination with an appropriate flow assured a homogeneous interaction with the foils and the carbon-bearing gasses. The optimal combination was verified by examining the cross section of all foils and sides. As for the powders and flakes residing in ceramic crucibles, optimal carburizing conditions were obtained if the crucibles were not filled completely. In this way inhomogeneous carburization was minimized. Bulk specimens were placed like foils and no problems that were caused by the flow conditions were observed. The carburizing temperature was selected in order to avoid carbide precipitation during carburization. It was realized that the carburizing temperature had to be chosen lower for thinner samples. This subject will be addressed in a later chapter of this thesis. Two different gas compositions were used; $CO+H_2$ and $C_2H_2+H_2$. Using CO as carburizing agent, it was observed that the presence of H_2 increased the carbon uptake markedly. Hence surface kinetics did play a significant role. A CO/H_2 flow of 50/50 gave the fastest carbon uptake. This was probably due to the favouring of the heterogeneous water-gas shift reaction (2.4) where a 1:1 stoichiometry for CO and H_2

applies. Evidently, deviation from the 1:1 stoichiometry affects the reaction rate at the surface. In the case of C_2H_2, increasing the relative amount of H_2, had the expected effect of reducing the carbon potential and the carbon uptake and, accordingly, had a non-sooting effect.

Before the carburizing treatment, the furnace was evacuated and filled with N_2 at least twice in order to remove oxygen. Subsequently, the process gas was led into the furnace, simultaneously with the protective gas through the measurement compartment. A protective gas flow of 5 mL/min, was applied for all experiments. The time-temperature program was not initiated until the weight was constant (i.e. when a stationary gas composition was attained in the furnace). Heating to the carburizing temperature was carried out at a rate of 20 K/min, or as cooling from the austenitizing temperature. Due to buoyancy forces attributed changes in the gas composition a correction run was required for each sample run. The correction run entailed an identical time-temperature-gas program but with a dummy sample. Examples of the various curves are shown in Figure 2.4.

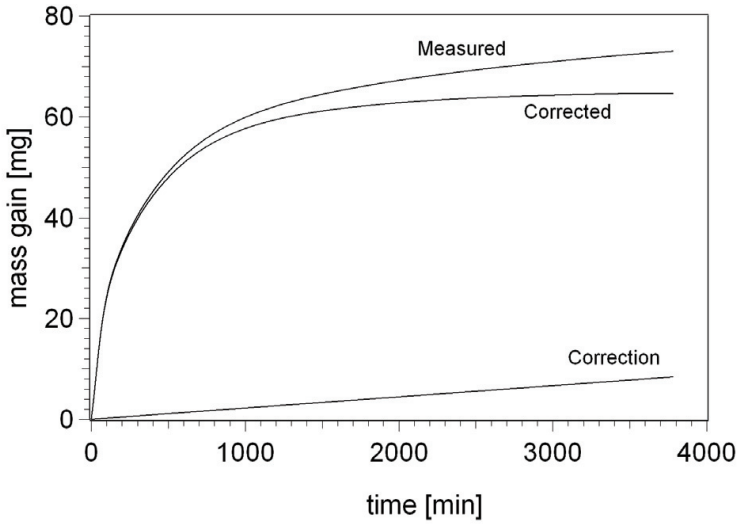

Figure 2.4: TGA curve showing the measured mass gain, the correction curve and the corrected mass-gain curve.

2.4 Metal dusting experiments

2.4.1 In thermombalance

Metal dusting experiments conducted in the thermobalance were performed in a gas mixture of C_2H_2+H_2 at 823K with a flow of C_2H_2 of 2 mL/min and a flow H_2 of 100 mL/min unless otherwise stated. Foils of 100μm thickness were applied. It was believed that carburization from both sides of the foil would accelerate the metal dusting process due to a faster carbon concentration build up. It was anticipated that by means of the accelerated process (partly due to the aggressive gascomposition and the use of foils) it was possible to capture the whole process ranging from dissolution of carbon in the austenite lattice to eventually all sample material was transformed into metal particles and dust. A metal dusting sequence was terminated after 337 hours at a point where thinning of the foils was observed. Due to limitations on sample weight and geometry (thermobalance restrictions), a dedicated metal dusting furnace was constructed in order to do metal dusting experiments on larger bulk samples.

2.4.2 In dedicated metal dusting furnace

The dedicated metal dusting furnace was made of an horizontal alumina tube terminated by flanges made of aluminium. Gasses were mixed before entering the furnace and exiting the furnace in the other end where the thermocouple is also connected. The outlet gas is terminated in a water-bath as precaution to prevent backflush of oxygen. The dedicated metal dusting furnace is designed to be as simple as possible, thus no pump was connected for evacuating before experiments. It was found that flushing the furnace with nitrogen or hydrogen for a few minutes before the beginning of the experiment was satisfactory. Samples are loaded on an aluminium bed and placed in the centre of the ceramic tube. The thermocouple measures the temperature directly beside the samples. It was realized that more favourable flow conditions were maintained in the dedicated metal dusting furnace in comparison to the thermobalance. Irrespective of sample position and orientation, the samples were homogeneously attacked. This was probably due to an increase in the relative amount of C_2H_2 gas. The applied gas composition in the dedicated metal dusting furnace was always 5 mL/min C_2H_2 and 15 mL/min H_2. The metal dusting experiments generally resulted in heavy carbon deposits. For consistency the metal dusting furnace was heated under ambient conditions to 973K before each experiment, thus burning off the carbon deposits to CO_2.

2.4.3 In environmental scanning electron microscope (ESEM)

It was attempted to perform in situ metal dusting experiments using the Environmental Scanning Electron Microscope (ESEM) at Haldor Topsøe A/S. The idea was to saturate stainless steel thin foils with carbon prior to the investigations in the ESEM. On subsequent carburization in the ESEM, growth of carburizing pits was hopefully to be observed. Unfortunately, the carburizing gas applied (2%C_2H_4+95%H_2+5%Ar) were either; i) not reducing enough to prevent the sample from oxidizing, or ii) not aggressive enough (too low carburizing potential) to resume carburization. Another in situ experiment was designed to follow the further development of microstructures observed on cross section of foils obtained during the metal dusting experiments. Restrictions on sample geometry in the ESEM heating stage sample holder, typically 3·3 mm, imposed some experimental difficulties. The difficulties relate the polishing of the foils without embedding them in resin, since the foils would then be unreachable. A specially designed stainless steel preparation holder was manufactured, in which foils could be suspended during polishing. Afterwards, foils were released from the preparation holder and mounted in a carbon (conductive) cylinder-shaped holder with a slit so foils maintained an upright position. Finally the carbon cylinder was mounted in the ESEM heating stage. It was assumed that the microstructure changes in the centre of the foils were related to decomposition of carbon expanded austenite and precipitation of carbides, and less to the interaction with the carbon bearing gasses at the surface. Thus the microstructure changes were primarily thermally induced. Accordingly, the experiment should reveal the effect of subsequent heating at a temperature similar to the carburizing temperature. Unfortunately, a heavy oxide formation on the surface obscured any possible features evolving on the surface. The required partial pressure of H_2 necessary to keep the sample from oxidizing was too high to keep the gas pressure around the Field Emission Gun (FEG) at an acceptably low level.

2.5 Oxidation experiments

Oxidation experiments were carried out prior to and after exposure to metal dusting conditions. The oxidation tests were conducted in a horizontal laboratory furnace with a gas mixture of argon and 46% H_2O(g). The relatively high steam content was chosen because a large oxygen partial pressure was desirable. It was presumed that it would develop a pronounced internal oxidation zone and thereby provide insight in the effect of oxide-metal surfaces on metal dusting. A water vapour content of 46% in argon was obtained by leading the argon through a water bath heated to 353K. The water bath temperature was calculated from thermodynamics to adjust the partial pressure of steam corresponding to the desired value. It was assumed that the gas mixture would behave like an ideal gas, which is in accordance to thermodynamic considerations

at low pressures and temperatures. The applied water was deionised to prevent any reaction with the possibly present ions. After the samples were positioned, the furnace was flushed at room temperature with argon for at least 24 hours prior to the heat treatment. The heater for the water bath and the furnace were started simultaneously. The heating time for the furnace was approximately 50 minutes and the cooling time was approximately 12 hours. The exposure time was 169 hours for all oxidation experiments, not including the heating- and cooling time.

2.6 Sample post-treatment

Treated samples were examined by means of cross section investigations. This was carried out by embedding the specimens in a resin using an Prontopress. The mounting material was typically chosen to be Duofast or a high carbon content resin such as PolyFast. The high carbon content resin was chosen if SEM investigations were to be applied on the cross sections, since this type of resin has a high conductivity in order to minimize charging effects due to the interaction with the electron beam. Foils and bulk specimens were placed in an upright manner. Obviously, this was not possible with flakes or powders, which were placed randomly. Due to the large number of flakes and powders, a part of the flakes did maintain an upright position allowing a true cross section investigation. The embedded samples were ground using an Abramin grinding machine. Foils and bulk samples were ground with successively finer emery paper in the range 220, 320, 500, 1000 and 4000 until a mirror-like finish was obtained. Finally the samples were polished with 3μm and 1μm diamond paste. In the case of powders and flakes the first polishing step entailed grinding with 1000 mesh emery paper. Finally, in order to emphasize the microstructures, samples were etched for 5-20 seconds in Kallings reagent no.1. The etchant affects the base alloy differently than areas supersaturated with carbon, so layers of carbon expanded austenite are easily distinguished from the base material. Roughly, the etching time is proportional to the contrast observed by light optical microscopy. Also affecting the contrast is the sensitization of the material, which indicates a loss of corrosion resistance due to precipitation of chromium carbides. If the chromium content in the depleted zone decreases below a critical value, the zone will lose its corrosion resistance and the material becomes sensitive to intergranular corrosion [44]. Hence, when comparing the metal dusting attack of foils exposed for different amounts of time, the effect of etching was indicative for the advancement of the metal dusting attack. Thus the etching time was carefully chosen and kept constant throughout the sequence, so that any changes in contrast could be attributed to the increased sensitization

2.7 Lift-out by Focused Ion Beam (FIB)

Stainless steel 100μm foils exposed to metal dusting conditions were investigated by Transmission electron microscopy (TEM). TEM examinations were carried out at Materials Research Division, Risø National Laboratory for Sustainable Energy (RISØ-DTU). TEM samples were prepared by a Focused Ion Beam (FIB) instrument located at Center for Electron Nanoscopy at DTU (CEN).

The FIB instrument has three functions: imaging, cutting and deposition. The FIB instrument, a FEI Quanta 200 3D FIB SEM Dual Beam, is a so-called Dual Platform instrument which incorporates an ion column and in addition, an electron column (i.e. an SEM). There are certain advantages to combined FIB/SEM systems. The main benefit is that the electron beam can be used for imaging of the sample without concern of sputtering of the sample surface. The Quanta 200 3D consists of a vacuum system and chamber, a liquid metal ion source, an ion column, a sample stage, detectors, gas delivery system (W and Pt), an electron column, camera, omniprobe, and a computer to run the instrument. The Ion beam (I-beam) is used to remove material with Ga^+ ions, or when used in conjunction with gas source, to deposit metal. The W gas source is used with the I-beam for W film deposition. Usually it is applied to protect surfaces from I-beam damage but it can also be used as welding material. Normally the Pt gas source, used with I-beam for Pt film deposition is applied to weld since more flexible joints are obtained compared to W-welded joints. The electron beam is used to non-destructively imaging of sample surface. The omniprobe is a 2μm thick W needle used for micromanipulation, e.g. TEM lift-out.

The camera provides live in-chamber view. Finally, the detector detects secondary electrons from E- or I-beam scans. It can also be used to image backscattered electrons.

3

Dissolution of carbon in expanded austenite

In this chapter the lattice parameter as a function of interstitially dissolved carbon is determined by carburization of thin stainless steel foils. For the first time this dependency is determined on unstrained austenite at room temperature. It is found that a linear relation holds between the lattice parameter, a, and the occupancy of the octahedral interstices, y_C. Furthermore, the maximum solubility of carbon in expanded austenite is determined at two temperatures. From controlled carburization of stainless steel foils it is found that the precipitation of chromium carbides is unavoidable for carbon contents above approximately 3.5wt% and that the maximum carbon content dissolvable in the f.c.c. lattice is 4.4wt% at 693K. Moreover, from controlled carburization of stainless steel flakes it is found that, the precipitation of chromium carbides is suppressed for carburizing temperatures of 613K and that the maximal dissolvable carbon content in the f.c.c. lattice is 5.3wt% at 613K. The hardness associated with the dissolved carbon, as measured on the metallographic cross sections, is shown to increase linearly with carbon content. Finally, for a low carburizing temperature it is shown that ferrite in heavily deformed stainless steel flakes is transformed to expanded martensite or expanded austenite during low-temperature carburization.

3.1 Introduction

Austenitic stainless steels are widely used as corrosion-resistant materials. Engineering these materials towards improvement in wear and corrosion resistance could be accomplished by interstitial dissolution of large amounts of carbon and/or nitrogen into the surface by carburization, nitriding or nitrocarburizing at a temperature below which effectively no carbides or nitrides develop. This brings about a supersaturated solid solution of interstitials in austenite, so-called expanded austenite, which is stabilized by carbon and nitrogen [33, 34]. The challenge is to avoid the precipitation of carbides during the surface hardening process to maintain good corrosion properties. This can be circumvented by choosing a low temperature where substitutional atoms do not diffuse over distances longer than a few atomic spacings within process duration. The maximum allowable carburising temperature for transformation of the surface into carbon expanded austenite is normally reported to lie within the temperature range 773-823K [45], depending on the desired case depth and associated carburizing time. This is at least 50K higher than for low temperature nitriding where nitrogen expanded austenite develops [46]. In both scenarios the processing temperature is high enough for interstitially dissolved carbon/nitrogen atoms to retain considerable mobility but low enough to limit the mobility of the substitutional atoms to a level where the metal atoms are virtually immobile as compared to nitrogen and carbon. Consequently, no carbide or nitride precipitation can occur. Expanded austenite is thermodynamically metastable and tends to decompose upon thermal exposure, leading to the formation of the thermodynamically stable phases, viz. carbides or nitrides. Such decomposition is highly unwanted for surface engineered stainless steels, because as a consequence the good anticorrosive performance is lost.

Regardless of whether the purpose of dissolution of carbon or nitrogen in stainless steel

is surface engineering of materials or scientific research on homogeneous samples, it is not a straightforward task, because the passive oxide film that covers the surface, and which accounts for the good corrosion properties, has to be effectively removed before carbon and/or nitrogen atoms can be dissolved in the interstices of the lattice. Plasma-assisted processes in which the passive film is sputtered away have traditionally been applied for this purpose. However, the thermodynamics are ill-defined and reliable thermodynamic results have therefore not been obtained. In this study, a recently patented method [40] developed for surface hardening of stainless steels is applied. The advantage of this method is that the passive oxide film that protects the stainless steel surface is removed during the gaseous treatment. Accordingly, studies for assessing thermodynamic parameters and kinetic data, or mechanical properties pertaining to carbon expanded austenite are rendered possible. As for example, when determining the lattice parameter of expanded austenite by X-ray diffraction it should be realized that a weighted average is obtained over a certain depth range, and that this weighted average depends on the absorption of the applied radiation in the materials probed. The major difficulty with the vast majority of the samples hitherto investigated with X-ray diffraction is that they suffer from compositional inhomogeneity within the depth range investigated with X-rays [47]. In the present work this is circumvented by a homogenization step following the carburizing process as to redistribute the adsorbed carbon atoms throughout the sample, such that the effect of composition induced stresses on the peak positions can be ruled out.

3.2 Experimental

3.2.1 Gaseous carburizing by thermogravimetry

Thin foils of stainless steel AISI 316 and flakes of stainless steel AISI 316L, with thickness 7.5μm and 1.2μm, respectively were used for carburizing. Gaseous carburizing was performed in a Netzsch 449C simultaneous thermal analyzer, which allows thermogravimetric analysis (TGA) simultaneously with differential thermal analysis (DTA). Gaseous carburizing was performed in atmospheres of acetylene, hydrogen and nitrogen[1]. The flows were adjusted by Brooks electronic mass flow controllers to: 0.2 ml or 50 mL C_2H_2/min, 50 mL H_2/min and 5 mL N_2/min.

AISI 316 foils

For recrystallization and austenitization the stainless steel foils were heated to 1353 K at a heating rate of 30 K/min and upon reaching this temperature immediately cooled in pure H_2. During austenitization any deformation-induced martensite formed by manufacturing of the materials was entirely transformed to austenite. The austenitization was conducted in a separate, for this purpose, dedicated furnace in order to make larger batches. Subsequently the foils were mounted in the thermobalance for carburizing. The foils were heated to a carburizing temperature of 693K in pure hydrogen and nitrogen reaching the carburizing temperature within approximately 20 min. Upon reaching the carburizing temperature, the gas composition was changed to the mixture of C_2H_2, H_2 and N_2. In order to obtain different carbon contents, and to follow the development of expanded austenite, ten carburizing experiments were performed on thin foils yielding samples with different average carbon contents in the range [0.5-6 wt%]. Subsequently the gas composition was changed to pure Ar followed by immediate cooling. In order to correct for the influence of buoyancy effects, an identical temperature-time-gas composition program was run with empty crucibles. In order to establish the relation between dissolved carbon and lattice parameter, six of the as-carburized foils were subsequently treated in pure Ar for 5 h at a temperature of 773K ($500^{\circ}C$) to redistribute the absorbed carbon atoms over the entire thickness of the foil. The homogenization time was estimated with the model in [48] using the value for the diffusion coefficients determined in [49], i.e. $4.10 \cdot 10^{-16} m^2 s^{-1}$. The thermobalance allowed continuous monitoring of the sample weight, securing that no decarburization occurred during the homogenization.

[1]For protecting the balance chamber from acetylene, high-purity nitrogen was led through the measurement compartment and thereafter the carburizing compartment, hydrogen and acetylene were directly led into the carburizing compartment

AISI 316L flakes

For recrystallization and austenitization the stainless steel flakes were heated to 1273 K at a heating rate of 30 K/min and, as to prevent sintering, upon reaching this temperature cooled to the carburizing temperature of 613K in pure H_2 to prevent the development of carbides at the very large surface. Upon reaching the carburizing temperature, the gas composition was changed to the mixture of C_2H_2, H_2 and N_2. Five carburizing experiments were performed on such austenitized stainless steel flakes, yielding samples with different average carbon contents in the range 1-6 wt% within carburizing times in the range 10 min to 18 h. Subsequently the gas composition was changed to pure Ar followed by immediate cooling. In order to correct for the influence of buoyancy effects, an identical temperature-time-gas composition program was run with empty crucibles. Furthermore four carburizing experiments were performed on as-delivered, i.e. heavily deformed, stainless steel flakes at 613K in a mixture of C_2H_2, H_2 and N_2. The four carburizing experiments yielded four different batches with carburizing times in the range 150 min to 24 h.

3.2.2 X-ray diffraction

X-ray diffraction was applied for the identification of the as-prepared and carburized material. The applied instrument was a Bruker AXS (Bruker AXS GmbH, Germany) D8 X-ray diffractometer, equipped with a Cr anode and a set of Göbel mirrors in the incident beam. The carburized foils were mounted on carbon tape and placed in the instrument. The carburized flakes were submerged in ethanol, and the slurry was smeared onto a glass-plate and, after evaporation of the ethanol, placed in the instrument. Positions of the Bragg peaks in the X-ray diffraction patterns were obtained from fitting a pseudo-Voigt peak shape function through the measured intensities forming the peak. In the fitting procedure corrections for $K\alpha 2$, Lorentz-polarization and absorption factors were included. Due to a strong crystallographic texture in the foils, the lattice parameter was determined from the position of the $\gamma_C(220)$ peaks only.

3.2.3 Microhardness measurements

The carburized foils were mounted in resin and prepared by standard metallographic techniques. Microhardness measurements were performed on the metallographic cross-sections of the homogenized foils with six different carbon contents. Approximately 80 micro indents with a load of 1g were made on each foil. The necessity of many hardness values was due to the relatively thin foil (7.5μm) and the associated uncertainty when performing the micro indents close to the edge and the relatively large spread when performing microhardness measurements at low loads. The size of the micro indents was measured with scanning electron microscopy at a magnification of 10,000x.

3.3 Results and interpretation

3.3.1 Lattice parameter of carbon expanded austenite

X-ray diffraction patterns of the as-carburized AISI 316 foils and the austenitized reference are given in Figure 3.1a. Due to a strong crystallographic texture in the foils, only the $\gamma_C(220)$ reflections are shown and used for interpretation. A peak shift of f.c.c. peaks to lower diffraction angles is observed for all carburised specimens; this is a direct consequence of the expansion of the f.c.c. lattice by the dissolution of carbon atoms, i.e. the development of γ_C.

As verified by the broadening and splitting of the $\gamma_C(220)$ peaks a pronounced carbon concentration profile exist in the as-carburized foils. X-ray diffraction patterns of the foils after homogenization are presented in Figure 3.1b. Evidently the homogenization-procedure results in more symmetric peaks and disappearance of the peak associated with the uncarburized substrate, indicating that a redistribution and levelling of the carbon atoms over the thickness of the foil has occurred indeed. The lattice parameter, a, of $\gamma_C(220)$ was determined from the position of the $\gamma_C(220)$ line profile. No correction can be made for the presence of stacking faults in

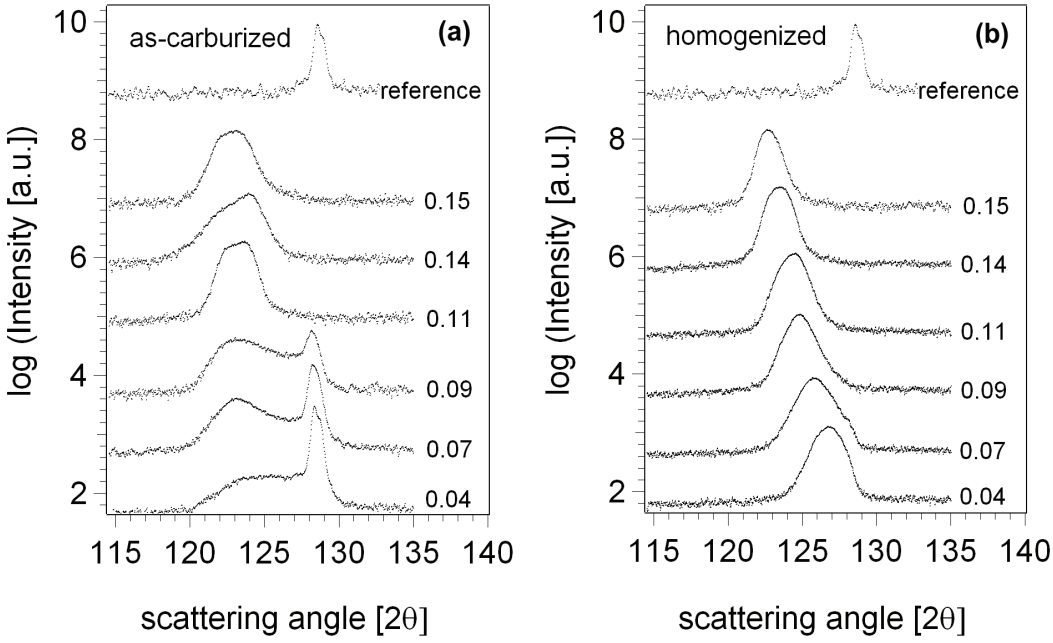

Figure 3.1: X-ray diffraction patterns of the carburized- (a) and homogenized (b) AISI 316 foils with six different carbon contents in the range y_C=0.04 to y_C=0.15. The austenitized reference is also included.

this case, because only one peak position is available. Since the interstitial contents that can be realized in γ_C are substantially lower than in γ_N, the probability of deformation-induced stacking faults is expected to be appreciably lower than for γ_N. As shown for γ_N samples, peak shifts associated with stacking faults in expanded austenite are limited to < 0.2 degrees 2θ (for high N contents) [36].

In Figure 3.2 the lattice parameter of $\gamma_C(220)$ is presented as a function of the number of carbon atoms per metal atom residing in the interstitial sublattice that is formed by the octahedral interstices. Clearly, a linear relation holds between the lattice parameter, a, and the carbon content, y_C.

Literature data relating carbon dissolved in Fe-austenite to the lattice parameter is generally determined from retained austenite in as-quenched martensitic specimens. Cheng et al. [50] suggested that stresses in the majority of the martensite can introduce pronounced compressive stresses in the retained austenite in Fe-C specimens, consequently leading to a compressive strain of about 0.4% in retained austenite. Literature data are collected in Figure 3.3 and compared to the present findings. Literature relations apply for carbon contents up to 1.4 wt.% C (y_C=0.067), hence extrapolations of literature data are applied in order to compare to the findings in the present work.

Evidently, the reported data can roughly be subdivided in two classes: i) high partial molar volume of carbon (solid lines) and ii) low partial molar volume of carbon (dashed lines). The reported values for lattice expansion of austenite due to carbon dissolution range from 0.0028 (nm/wt.% C) as determined in the present work and by Kahn et al. [51] for unstrained austenite, to the highest value determined from carburized specimens without accounting for stress effects; 0.0054 (nm/wt.% C) [34]. In order to obtain the dependence of austenite lattice parameter on carbon content for unstrained austenite Cheng et al. [50] included data for iron-carbon specimens measured at elevated temperature, where the specimens are fully austenitic (and thus strain-free) and extrapolated to room temperature. Both dependencies, strained and unstrained are included in Figure 3.3. Similarly, in the most recent study by Kahn et al. [51] the dependencies for strained austenite and, after correcting for stress effects, unstrained austenite, are included. Ridley et al.

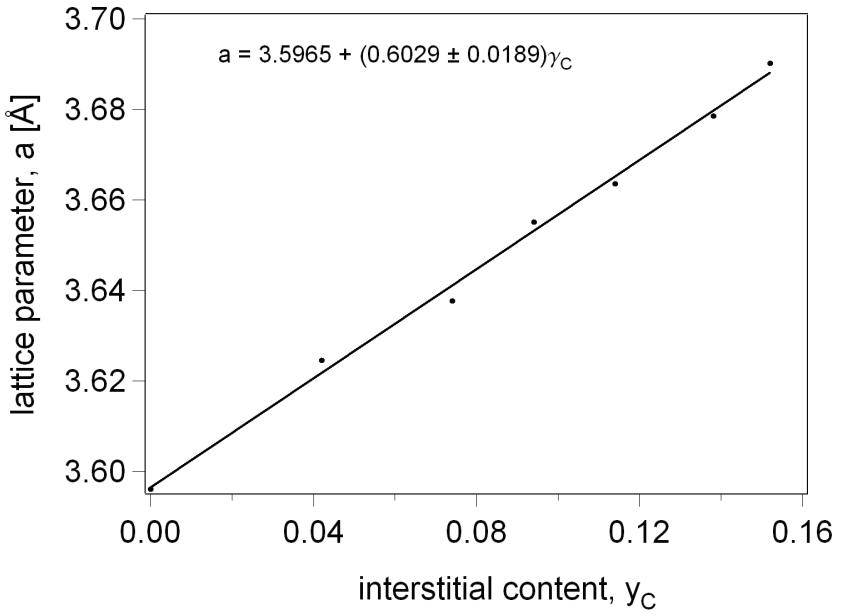

Figure 3.2: Lattice parameter, a, of expanded austenite as a function of the number of carbon atoms per metal atom (y_C) in γ_C.

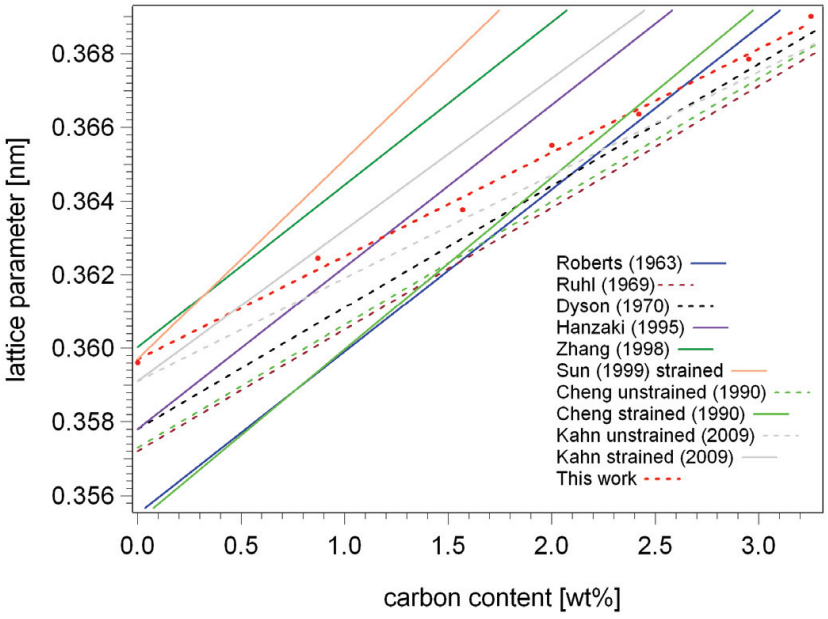

Figure 3.3: Literature data relating the lattice parameter, a, of γ_C as a function of carbon content (wt.%) The relation determined in the present work is included.

[52] suggested that the smaller lattice parameters observed for retained austenite, particularly in the lower carbon content range where the amount of retained austenite is small, could be due to (hydrostatic) compressive strains arising from the transformation. Alternatively, carbon depletion has occurred due to precipitation which would be facilitated by the high dislocation densities formed during the transformation. A high dislocation density will dissolve additional carbon without affecting the lattice parameter to a large degree. When comparing the data from the present work with literature data, clearly a much better overall agreement is obtained with relations for unstrained austenite than for strained austenite. For expanded austenite the present work is the first that assesses the entire lattice parameter dependence merely on a series of strain free samples with different carbon contents.

3.3.2 Solubility of carbon in stainless steel foils (693K)

X-ray diffractograms of as-carburized AISI 316 foils and the austenitized reference are given in Figure 3.4. The patterns for carbon contents in the range 0.87 wt.% (y_C=0.04) to 3.25 wt.% (y_C=0.15) are identical to those presented in Figure 3.1. For average carbon contents in the range 0.87 wt.% to 2.00 wt.% reflections of uncarburized austenite are identifiable, which implies that through-carburising of the foils has not occurred. The γ_C peaks become narrower with increasing average carbon content, which can be attributed to a more uniform carbon distribution of C in y_C. An explanation for this observation is provided by a larger flux of carbon atoms into the foil with increasing carbon activity in the gas phase. This larger flux is caused by the larger initial concentration gradient and the higher carbon diffusivity for higher carbon contents. At 4.16 wt.% reflections pertaining to $M_{23}C_6$ become significant, at 58, 68 and 75 degrees 2θ (Figure 3.4 left). At 4.72 wt.% reflections pertaining to M_7C_3 becomes visible, at 61, 66 and 69 degrees 2θ. From 4.16 wt.% to 5.31wt.% no further shift of $\gamma_C(220)$ to lower Bragg angles is observed (Figure 3.4 right), which indicates that no further dissolution of carbon atoms in the f.c.c. lattice is possible. Due to the poor intensities of the Bragg reflections (strong crystallographic texture) in the 2θ regime 50-90 degrees, it is difficult to be specific about the exact form of the carbides. An investigation dedicated to the precipitation of carbides will be treated in Chapter 5.

The mass gain curve for the 5.31 wt% experiment is presented in Figure 3.5. Evidently, a stationary carbon content has been reached. The corresponding 2θ value for $\gamma_C(220)$ is 120.9 degrees (Figure 3.4), which from the correlation between peak shift and dissolved carbon interstitials (Figure 3.2) corresponds to a dissolved carbon content of 4.4 wt.% (y_C=0.211). Thus the maximum solubility of carbon in expanded austenite in metastable equilibrium with M_7C_3 is 4.4 wt.% (y_C=0.211) at 693K. The maximum achievable carbon content dissolved in the f.c.c. structure without the presence of carbides is approximately 3.5 wt.% (y_C=0.164) at 693K.

3.3.3 Solubility of carbon in stainless steel flakes (613K)

A series of carburizing experiments was performed at 613K on austenitic stainless steel flakes with a thickness of 1.2μm. X-ray diffraction patterns of the as-carburized AISI 316 flakes and the austenitized reference are given in Figure 3.6. It was observed that flakes in the upper part of the crucible were not as thoroughly carburized as the rest of the flakes. This was due to an inefficient surface activation of these flakes during austenitizing. Hence, the signal pertaining to the austenite substrate which remains identifiable can be attributed to the sluggish carburized part of upper flakes. The effect of prolonged carburization (18 hours) merely resulted in a narrowing of the X-ray peaks, and not to further shift. The lowest 2θ value for $\gamma_C(220)$ is 119 degrees (insert in Figure 3.6), which from the correlation between peak shift and dissolved carbon interstitials (Figure 3.2) corresponds to a dissolved carbon content of 5.30wt.% (y_C=0.252). This indicates a maximum solubility of carbon in solid solution of 5.30wt.% at 613K in stainless steel flakes.

The mass gain curve corresponding to the experiment with a duration of 18 hours is presented in Figure 3.7. As observed, stationary mass has been reached at a mass gain of 6wt.%. According to the X-ray diffractogram in Figure 3.6, no carbides (incoherent) have precipitated, hence the discrepancy between the carbon content, as determined from the maximum shift of the $\gamma_C(220)$ peak (5.30wt.%), and the stabilized value at 6wt.% of the mass gain curve cannot be explained by

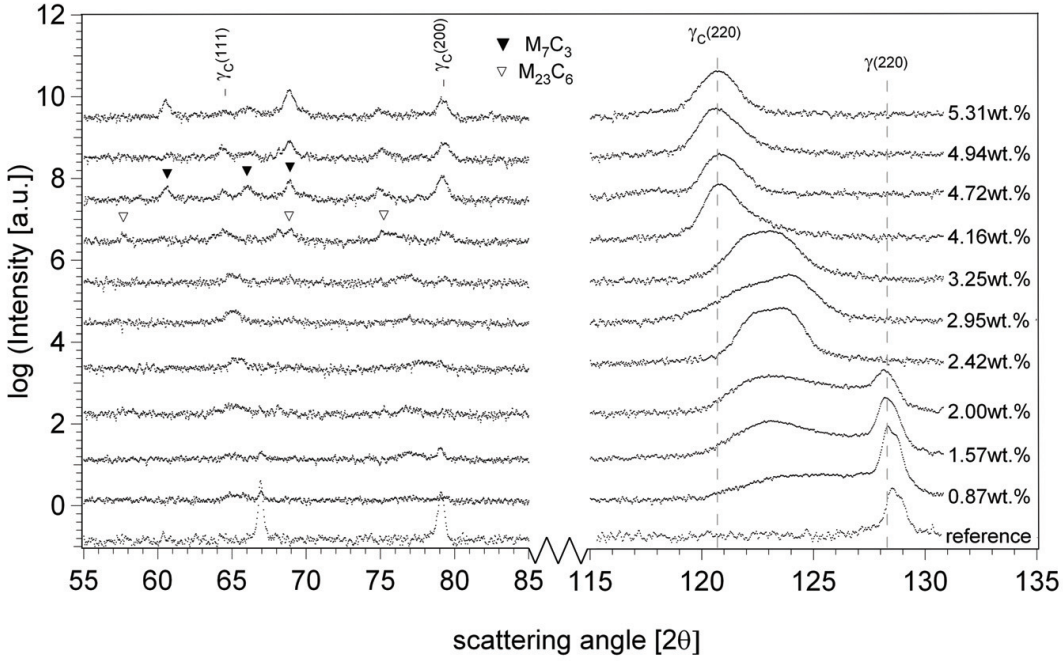

Figure 3.4: X-ray diffraction patterns of the carburized AISI 316 foils. Precipitation of carbides of the form $M_{23}C_6$ and M_7C_3 are indicated. From the established (a, y_C)-correlation the maximum shift of the $\gamma_C(220)$ peak indicates a maximum achievable carbon content dissolved in the f.c.c. structure in metastable equilibrium with M_7C_3 of 4.4wt% (y_C=0.211) at 693K.

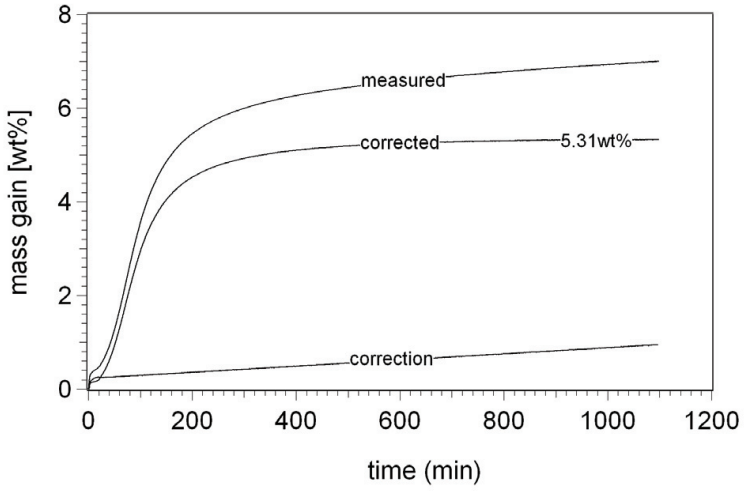

Figure 3.5: Thermogravimetric mass gain curve measured during carburization of AISI 316 foils at 693K in a gas mixture of C_2H_2 and H_2. The curve corrected for buoyancy stabilizes at 5.31wt%.

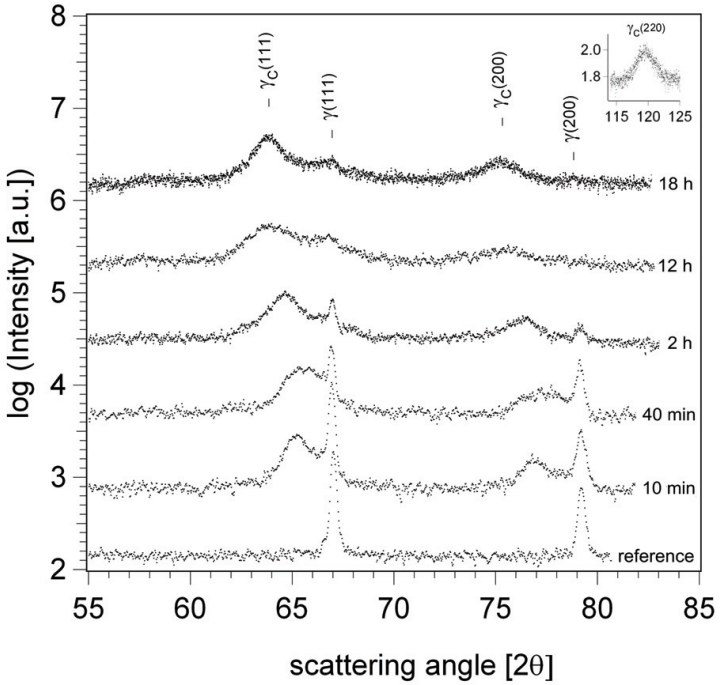

Figure 3.6: X-ray diffraction patterns of the carburized AISI 316 flakes. From the established (a, y_C)-correlation the maximum shift of the $\gamma_C(220)$ peak indicates a maximal achievable carbon content dissolved in the f.c.c structure of 5.30wt.% (y_C=0.252) at 613K. The signal pertaining to the austenite substrate which remains identifiable can be attributed to a non-carburized part of the flakes.

carbon bound in incoherent carbides. It is speculated that the discrepancy is caused by a small amount of unidentified deposits on the surface of the flakes or carbon bound in unidentifiable (by X-ray diffraction) coherent carbides formed during carburization.

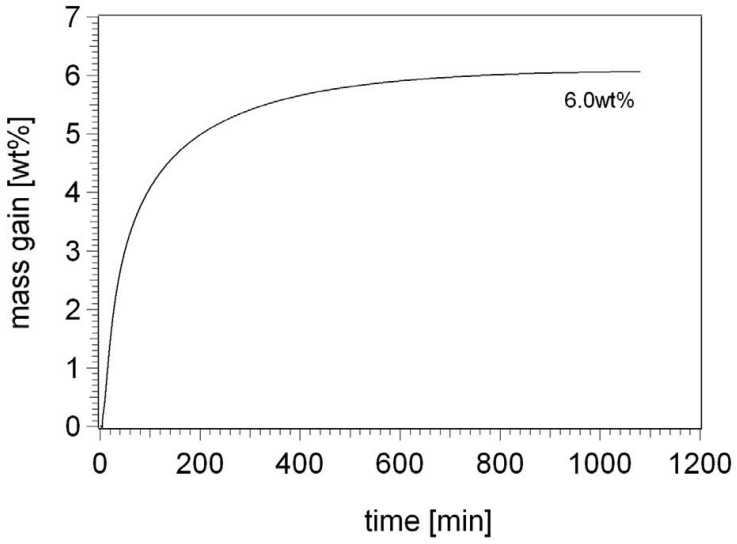

Figure 3.7: Thermogravimetric mass gain curve measured during carburization of AISI 316 flakes at 613K for 18 hours in a gas mixture of C_2H_2 and H_2. The curve corrected for buoyancy stabilizes at a mass gain of 6wt%.

The thermogravimetric mass gain curve measured during carburization of flakes reaches a higher maximum than carburization of foils (Figure 3.5). Presumably, the superior dissolution of carbon in the flakes is due to the lower carburizing temperature (613K vs. 693K) which suppresses the Cr diffusion and thus carbide formation, implying that higher carbon contents can be dissolved before actual precipitation occurs (a higher driving force for carbide formation can be accommodated).

3.3.4 Microhardness as a function of carbon content

The hardness values of homogenized foils with six different carbon contents in the range y_C= 0.04 to y_C= 0.15 are shown in Figure 3.8 as a function of the square root of the solute content. The microhardness values were measured on polished cross sections of the stress free foils.

The hardness associated with the dissolved carbon, as measured on the metallographic cross sections, is shown to increase linearly with carbon content.

3.3.5 Transformation of ferrite to expanded austenite/martensite by dissolution of carbon

X-ray diffraction patterns of the heavily deformed as-delivered flakes reveal the presence of ferrite, i.e. deformation induced martensite (Figure 3.9). To explore the isothermal ferrite to austenite transformation, the heavily deformed as-delivered flakes were subjected to carburization at 613K in a mixture of C_2H_2, H_2 and N_2. Four carburizing experiments yielded four different batches with carburizing times in the range 150 min to 24 h. As is observed in the X-ray diffractograms in Figure 3.9, on prolonged carburization the $\alpha(110)$ peak develops a continuous peak with the $\gamma_C(111)$ peak with a gradually higher carbon content. This observation could be interpreted as a shift of both austenite and ferrite peaks, indicating that, in addition to the development of expanded austenite, also expanded martensite develops. This martensite would be tetragonal. However, a spitting of the (110) ferrite peak in (110) and (101) martensite peaks is obscured

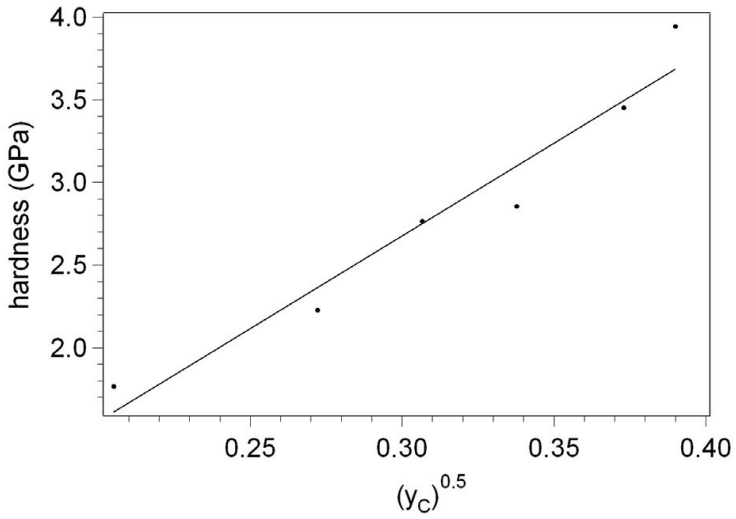

Figure 3.8: Relation between carbon content and Vickers hardness as measured with Vickers hardness indents on polished cross sections.

by the range of carbon contents present in the sample. Alternatively, the observation could be interpreted as a transformation of ferrite solely into expanded austenite.

A recent study by Michal et al. indicated a carburization-induced isothermal ferrite to austenite phase transformation [53]. It was demonstrated that the surface zone of an AISI 301 alloy containing approximately 40 vol.% ferrite was completely transformed into expanded austenite during carburization at 750K. For this transformation to occur the eutectoid temperature has to be lowered below the carburization temperature. Michal et al. further showed by applying a compound energy-based interstitial solid solution model that the predicted eutectoid temperature is reduced to 615K in AISI 301 due to the alloying additions. For the present case of AISI 316 it can be expected that the eutectoid temperature is higher than for AISI 301, which would be consistent with the stability of ferrite and its conversion to expanded martensite by the dissolution of carbon at 613 K.

3.4 Conclusion

The lattice parameter, a, of expanded austenite was for the first time determined experimentally on unstrained austenite at room temperature from a range of stress-free carburized foils of uniform composition and assessed to be linearly dependent on the occupancy of the octahedral interstices, y_C, according to: a = 3.5965 [Å] + (0.6029±0.0189)y_C or as a =0.3596 [nm] + (0.0028±9.07·10^{-5})x [wt.% C], which is in good agreement with existing literature data for unstrained ferrous austenite. At 693K, the maximum solubility of carbon in expanded austenite was determined to be 4.4wt.% and the precipitation of chromium carbides was observed to be unavoidable for carbon contents above approximately 3.5wt%. At 613K the precipitation of chromium carbides is suppressed and the maximal achievable carbon content dissolved in the f.c.c. structure is 5.3wt.%. The microhardness was shown to increase linearly with carbon content. Finally, it was shown that the isothermal ferrite transformation to expanded martensite or expanded austenite is induced by low-temperature carburization of heavily deformed as-delivered flakes.

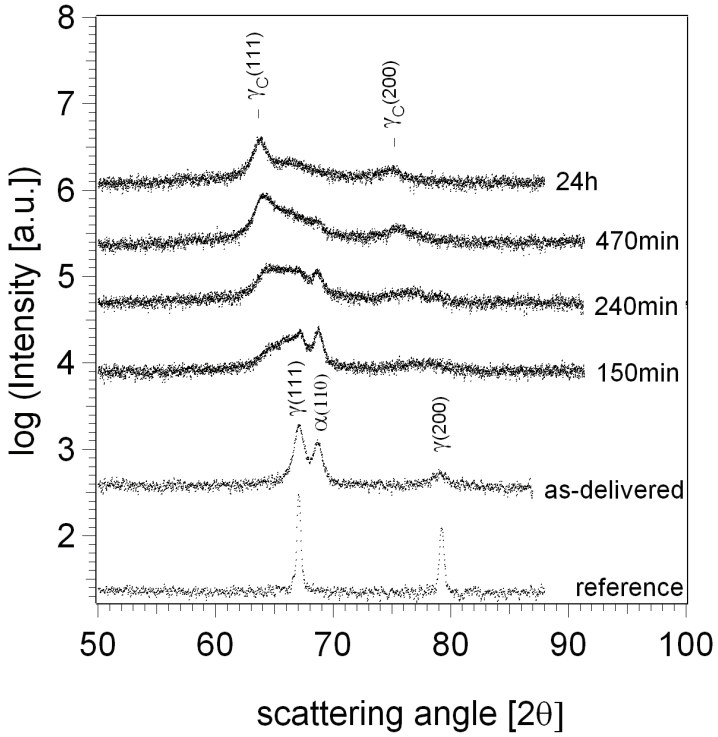

Figure 3.9: X-ray diffractograms of the increasingly carburized AISI 316 flakes. The ferrite present in the as-delivered flakes is transformed into expanded austenite or expanded martensite by carburization at 613K.

4

Diffusion of carbon in expanded austenite

In this chapter various experimental procedures to experimentally determine the concentration dependent diffusion coefficient of carbon in expanded austenite are evaluated. To this end thermogravimetric carburization was simulated for various experimental conditions and the evaluated composition dependent diffusivity of carbon derived from the simulated experiments was compared with the input data. The most promising procedure for an accurate determination is shown to be stepwise gaseous carburizing of thin foils in a gaseous atmosphere; the finer the stepsize, the more accurate the approximation of the diffusivity. Thermogravimetry was applied to continuously monitor the weight change of thin foils of AISI 316 during carburizing (at 793K) in CO-H_2 gas mixtures for one of the simulated experimental procedures. Furthermore, inverse modeling of a mass gain curve obtained on C_2H_2 low temperature carburized flakes (613K) applying a finite difference method [54] were carried out. The presented experimental results indicate that the diffusion coefficient of carbon in expanded austenite increases with carbon concentration. Furthermore, it is suggested, that the concentration dependent diffusion coefficient obtained by carburizing in CO atmospheres is influenced by surface kinetics, and hence must be considered as an effective diffusion coefficient.

4.1 Introduction

Process equipment in the petrochemical industry commonly suffers from metal dusting. This aggressive interaction between stainless steels (as well as nickel alloys) and carbon-bearing gases has been subjected to many studies [32, 55], however, so far, no accurate simulation of the carburizing stage prior to the actual metal dusting stage has been presented. A prediction of the carburizing kinetics involved in surface engineering as well as metal dusting of stainless steels demands fundamental knowledge concerning the diffusion of carbon in expanded austenite, i.e. austenite with a high supersaturation of carbon. So far very few studies have focused on and succeeded in obtaining reliable thermodynamic (i.e. carbon solubility in terms of carbon activity) and kinetic (i.e. diffusion) data on expanded austenite stabilized by carbon.

Generally, under practical circumstances the protective oxide scale on stainless steel delays the onset of the carburizing reaction. This implies that the initiation of so-called metal dusting pits is stochastic in nature. One of the strategies in materials design is therefore the improvement of the oxide layers stability in a carburizing environment and thereby prolonge the incubation time for metal dusting initiation. The stochastic nature of oxide layer breakthrough also implies that deliberate carburization of stainless steel surfaces requires an activation step, wherein the protective oxide layer is removed or by-passed. A successful pretreatment method was recently patented: the native oxide layer is electrochemically replaced by a very thin (10-20 nm) metal layer, which prevents the surface from forming a protective oxide scale and which catalyzes the surface reaction necessary to liberate carbon atoms from carbon-containing species in the gas mixture [43]. In the present work this pretreatment method is applied to the evaluation of the composition dependent diffusion coefficient of carbon in expanded austenite from sorption curves determined on thin foils of austenitic stainless steel with thermogravimetry. Another recently patented method [40] developed for surface hardening of stainless steels allows for carburization without pretreatment. In the present work this method is followed to carburize stainless steel

flakes with thickness 1.2μm and inverse modeling of the obtained mass gain curve is applied to determine the concentration dependent diffusion coefficient of carbon in expanded austenite.

Firstly, the initial rate method originally proposed by Crank is briefly discussed. Thereafter three measurement strategies for an experimental assessment are evaluated by simulation of the sorption curves and determination of the diffusion coefficients according the initial rate method applied to these sorption curves. Finally, the concentration dependent diffusivity of carbon in expanded austenite is experimentally determined for one of the three evaluated measurement strategies. The results are compared to the results by inverse modeling on a sorption curve obtained on C_2H_2 low temperature carburized flakes.

4.2 Initial rate method for determination of diffusion coefficient

Consider a slab of material with thickness l, wherein the diffusion coefficient of the diffusing species j is designated by D_j. For the early stages of diffusion-controlled sorption of component j, the total amount of component j, M_t, incorporated in the slab at time t, amounts to [56]:

$$\frac{M_t}{M_\infty} = \frac{4}{\pi^{1/2}} \left(\frac{D_j t}{l^2} \right)^{1/2}, \tag{4.1}$$

where M_∞ is the total amount of component j that has entered the sample after infinitely long sorption time. In a sorption (carburization) experiment the initial slope in a plot of M_t/M_∞ vs. $(t/l^2)^{1/2}$ is directly proportional to the diffusion coefficient D_j. If the diffusivity D_j depends on the concentration, C, of component j and the concentrations of component j prior to and after sorption are C_0 and C_s, respectively, the value obtained can be conceived as an average diffusion coefficient $\bar{D}_j$ [56]:

$$\bar{D}_j \left(\frac{C_s + C_0}{2} \right) = \frac{1}{C_s - C_0} \int_{C_0}^{C_s} D_j(C) dC. \tag{4.2}$$

Obviously, the narrower the composition range $C_s - C_0$, the closer the value for $\bar{D}_j \left(\frac{C_s + C_0}{2} \right)$ approaches the actual diffusivity $D_j \left(\frac{C_s + C_0}{2} \right)$.

4.3 Simulation of thermogravimetric sorption curves and reconstruction of diffusivity of carbon in expanded austenite

Thermogravimetric sorption curves of carbon during carburization of iron were simulated by solving Ficks second law and adopting a concentration dependent diffusivity of carbon in austenite. For the computational details see [57]. To the sorption curves the initial rate method was applied to evaluate the (presumed constant) carbon diffusivity in various composition ranges, in order to simulate the determination of the composition dependence of the diffusivity of carbon. Three different cases were investigated:

i the surface concentration was held constant at 7 at.% C and the starting concentration of carbon in the slab was stepwisely increased by 1 at.% C in each step.

ii series of slabs with initially no carbon were combined with surface concentrations ranging from 1 to 7 at.% C.

iii the maximum difference between C_s and C_0 was taken as 1 at.% C and the composition range was stepwisely changed from C_s=1 to C_s=7 at.% with a stepsize of 1 at.%.

In the simulations the concentration dependent diffusivity of carbon in austenitic slabs with a thickness of $2 \cdot 10^{-3}$m was taken as that determined for Fe-C austenite at 1400 K [58]. The sorption curves for these cases are given in Figure 4.1a-c. The composition dependent diffusivity of C in austenite used as input data in the simulations is compared with the values for $\bar{D}_j \left(\frac{C_s + C_0}{2} \right)$ derived with the initial rate method from the sorption curves. Obviously, an excellent agreement is obtained for case iii, whereas cases i and ii yield carbon diffusivities which deviate the more from the input data the larger the composition range used for the sorption curve.

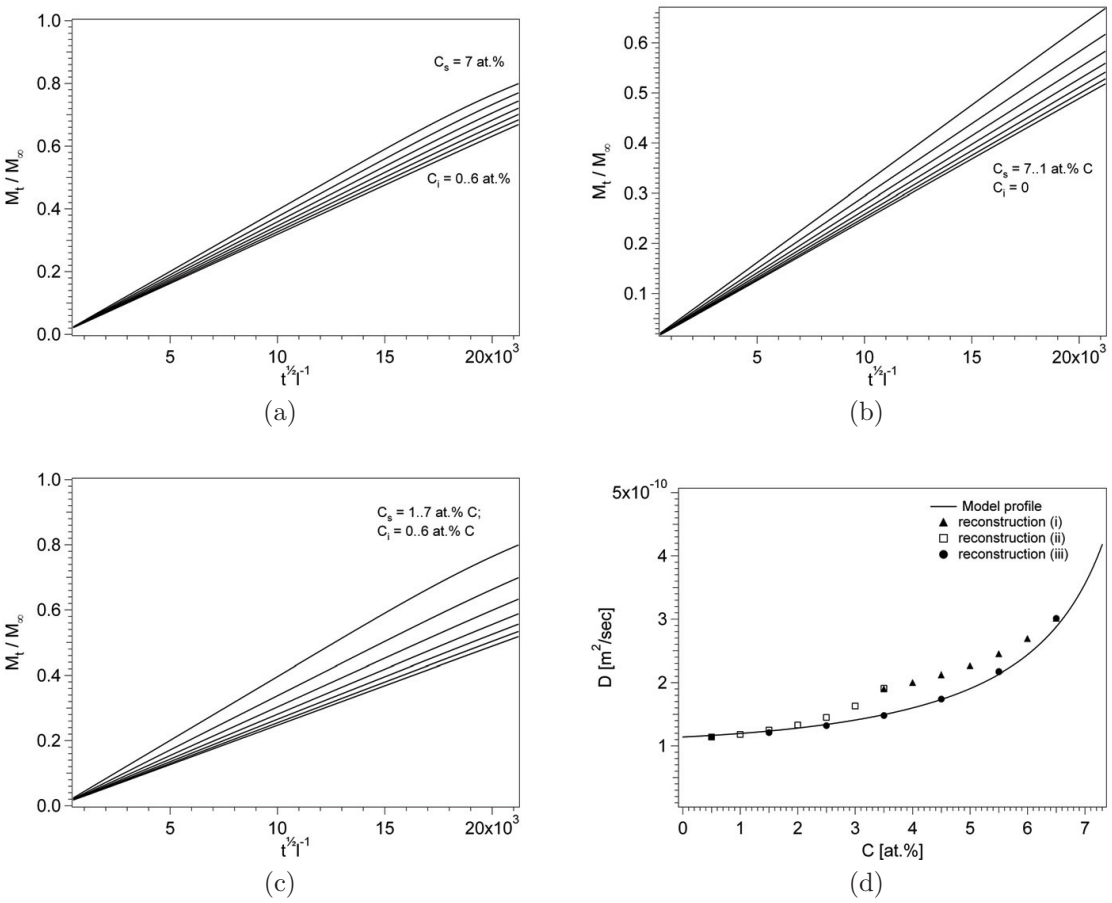

Figure 4.1: Simulated sorption curves for C in iron at 1400 K for cases (a) i, (b) ii and (c) iii (see text), (d) evaluated diffusion coefficients from applying the initial rate method to the sorption curves in a)-c) are compared to composition dependent coefficient used as input data for the simulated sorption curves.

4.4 Inverse modeling for determination of diffusion coefficient

A finite difference method was applied to simulate the sorption curve obtained during carburization of stainless steel flakes. The concentration dependent diffusion coefficient of N-atoms in nitrogen expanded austenite was obtained by the finite difference model in [48]. In modeling diffusion of N-atoms, trapping of N atoms is to be accounted for. In this work it is assumed that trapping of C-atoms does not occur. Furthermore it is assumed that the sorption is fully diffusion controlled. It is assumed that the concentration dependent diffusion coefficient can be described as:

$$D = \frac{D_0}{1 + 2a \cdot y_C + b \cdot y_C^2}, \tag{4.3}$$

where D_0 is the diffusion coefficient at y_C=0 and a and b are parameters which determine the shape of the curve. The values for a and b are assumed to be $a = 2.16$ and $b = 4.95$, that is, the shape of the curve is assumed to be identical to the shape for nitrogen diffusion in expanded austenite. In the simulation, the surface concentration is kept constant at the saturation level y_C=0.2896. Accordingly, the only fit parameter in the inverse modeling is D_0. For more details on finite difference modeling, the reader is referred to [54].

4.5 Experimental

4.5.1 Carburizing by thermogravimetry

Thin foils and flakes of stainless steel AISI 316, with thickness 7.5 μm and 1.2μm, respectively were used for carburizing. Gaseous carburizing was performed in a Netzsch 449C simultaneous thermal analyzer, which allows simultaneous thermogravimetric analysis (TGA) and differential thermal analysis (DTA). The samples were austenitized by heating to 1353 K [1] at a heating rate of 20 K/s in pure H_2 followed by immediate cooling to fully transform all deformation induced martensite, originating from cold rolling of the foils and the fabrication of flakes, into austenite.

Foils

After austenitization the passive oxide film covering the stainless steel foil surface was electrochemically replaced by a thin Ni-deposit in a Woods nickel bath, consisting of $NiCl_2$, $NiSO_4$ and H_2SO_4. The thickness of the deposited Ni layer was in the order of 20 nm and contributes to maximally 0.5% of the total sample mass. The solubility of carbon in the deposited Ni layer is negligible compared to the solubility in austenite. The foils were heated to a carburizing temperature of 793 K in pure H_2. Upon reaching the carburizing temperature, the gas composition was changed to a mixture of 20% CO and 80% H_2. Carburizing was continued until the weight gain of the sample corresponded to approximately 1.9 at.%. Subsequently the gas composition was changed to pure H_2 for 30 min as to redistribute the absorbed carbon atoms over the entire thickness of the foil. The homogenization time was estimated with the model in [9] using the anticipated value for the diffusion coefficients to be determined in the present work, i.e. $4.10 \cdot 10^{-16} m^2/s$. The cycle of boost carburization and homogenization of the carbon profile was repeated until a total mass gain corresponding to ca. 16 at.% carbon was reached. In order to correct for the influence of buoyancy effects, an identical temperature-time-gas composition program was run with empty crucibles.

Flakes

After austenitization, stainless steel flakes were immediately cooled in pure H_2 to the carburizing temperature of 613K. Upon reaching the carburizing temperature, the gas composition was changed to the mixture of C_2H_2, H_2 and N_2. Carburizing was maintained for 18 hours yielding a sample with a carbon content of 6 w.t%. Subsequently the gas composition was changed to

[1] Stainless steel flakes were only heated to 1273K to prevent sintering.

pure Ar followed by immediate cooling. In order to correct for the influence of buoyancy effects, an identical temperature-time-gas composition program was run with empty crucibles.

4.6 Results and interpretation

4.6.1 Foils

During the sorption experiment nine carburizing steps were realized. All carbon sorption curves determined at 793 K are presented in Figure 4.2a. The values for D determined from the sorption curves are given Figure 4.2b for various average carbon contents in the foils.

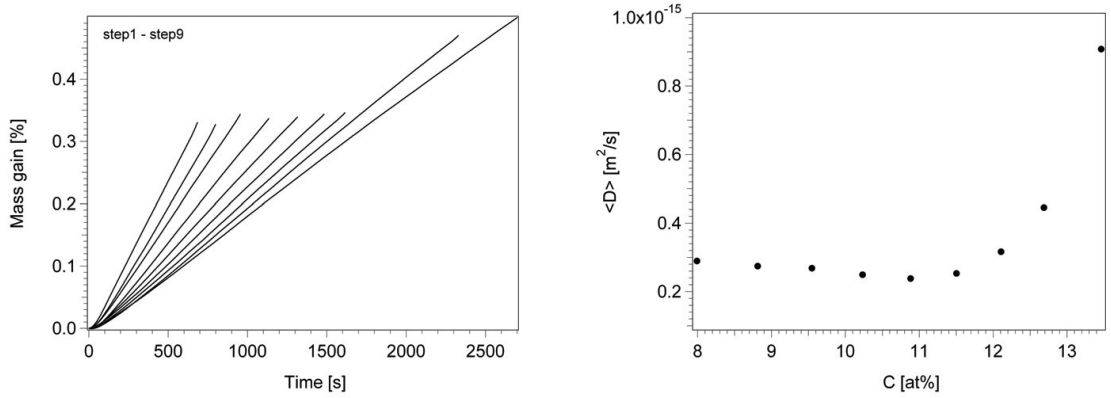

(a) (b)

Figure 4.2: (a) Initial part of sorption curves obtained during carburizing in CO-H_2. Each sorption stage was succeeded by a homogenization stage in H_2 before the next carburizing stage. (b)Weighted-diffusion coefficients of carbon in 316 stainless steel at 793 K obtained from the initial rates of carburizing (method i).

The applicability of the method presented in Section 4.3 relies on the presumption that diffusion controlled kinetics prevail during carburization, i.e. local equilibrium between the gas phase and the solid state is obtained instantaneously upon changing the gas composition. The sorption curves show that a linear relationship between $\frac{M_t}{M_\infty}$ and $t\frac{1/2}{l}$ is obtained shortly after adjusting the gas composition (at $t = 0$), which suggests that fast local equilibrium at the surface is obtained. This would be expected since the heterogeneous water-gas shift reaction occurring at the catalyzing Ni-surface and providing C to the sample is known to proceed fast [59]. However, the slight decrease of the diffusion coefficients in the composition range 8-11 at.% might indicate that some influence of the surface kinetics on the carbon uptake cannot be neglected. If surface kinetics would (partially) govern the carbon uptake, the diffusion coefficient will be underestimated.

4.6.2 Flakes

A carburizing experiment was performed on austenitic stainless steel flakes with thickness 1.2μm. The shift of the $\gamma_C(220)$ reflection indicates a carbon content in solid solution of 5.30 wt.%, as deducted from the correlation between peak shift and dissolved carbon interstitials (see Chapter 3). The mass gain curve is presented in Figure 4.3. As observed a stationary mass has been reached at a mass gain of 6 wt%. Since no carbides (incoherent) have precipitated, the discrepancy between the carbon content, as determined from the maximum shift of the $\gamma_C(220)$ peak, and the stabilized value at 6 wt.% of the mass gain curve cannot be explained by carbon bound in incoherent carbides. It is speculated that the discrepancy is caused by a small amount of unidentified deposits on the surface of the flakes or carbon bound in unidentifiable (by X-ray diffraction) coherent carbides formed during carburization.

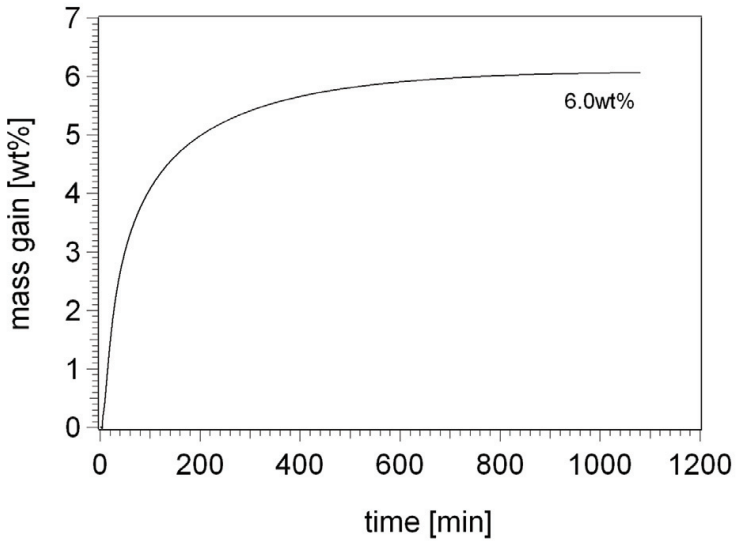

Figure 4.3: Thermogravimetric mass gain curve measured during carburizing of AISI 316 flakes at 613K in a gas mixture of C_2H_2 and H_2. The curve corrected for buoyancy stabilizes at a mass gain of 6 wt.%.

A finite difference method was applied to simulate the sorption curve. Good agreement between the measured and simulated sorption curve was obtained for a value of $D_0 = 8.0 \cdot 10^{-18}$ for y_C<0.17. For higher carbon concentrations (y_C>0.17), the experimental measured sorption curve deviates from the simulated sorption curve, which results in an overestimation of the diffusion coefficient for the simulated sorption curve. The determined concentration dependent diffusion coefficient is depicted in Figure 4.4, in which the diffusivity is observed to increase with the interstitial content in expanded austenite as expected.

4.7 Discussion

4.7.1 Foils

Strictly speaking the temperature ranges used in the simulations in Section 4.3 and the experiments described in Section 4.6.1 are incompatible and consequently the diffusivities in Figure 4.1d and Figure 4.2b differ by a factor 106. In this respect it should be mentioned that the thickness of the slab in the simulations (2 mm) and the thickness of the foils used in the experiments (7.5 μm) differ accordingly. Hence, the assumption lying at the basis of Equation 4.1 is justified in both the simulations and in the experimental part. Then, the conclusions drawn from the simulations in Section 4.3 have general validity, despite incompatible temperature ranges in simulations and experiments. As compared to the simulations in Section 4.3, the method pursued in the experimental part will provide an overestimation of the diffusivity of carbon in expanded austenite.

The obtained values for the diffusion constant are compared to the very few reported literature values. In Figure 4.1d (model profile) diffusion data of carbon in austenite at high temperatures is depicted [58]. Generally, the same trend in composition dependence is observed in Figure 4.1d and Figure 4.2b. Similarly, diffusion of nitrogen in expanded austenite shows similar trends, i.e. the diffusivity increases with the interstitial content in expanded austenite [48]. The dissolution of carbon (or nitrogen) atoms in the octahedral interstices of the f.c.c. lattice causes an isotropic expansion of the lattice. Accordingly the distance between the metal atoms in the closed packed lattice will increase thereby lowering the activation energy for migration of C atoms from one octahedral interstice to a tetrahedral interstice, which is considered the activated state of in-

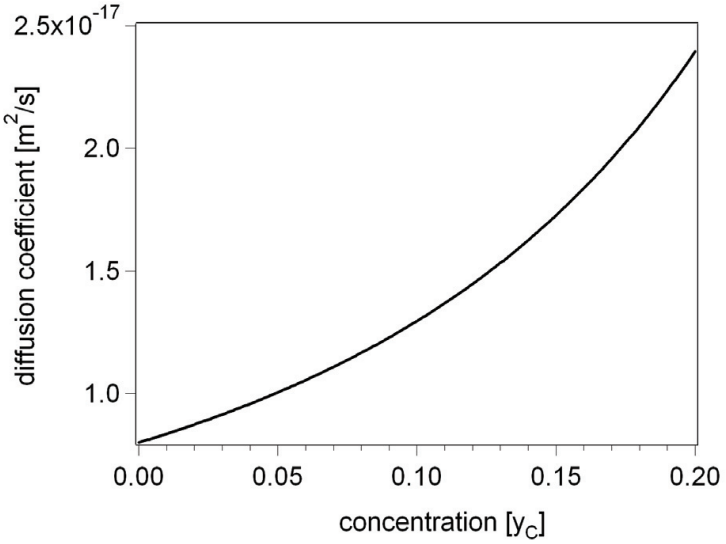

Figure 4.4: Diffusion coefficients of carbon in 316L stainless steel flakes at 613K obtained by inverse modeling of the sorption curve.

terstitial diffusion in an f.c.c. lattice. Consequently, the diffusion coefficient increases with the carbon content in the lattice.

4.7.2 Flakes

As previously hypothesized in Section 3, tiny carbides, diffracting coherently with the matrix, could be present in C_2H_2 carburized flakes. This is in accordance with the observed overestimation (by simulation) of the diffusion coefficient for carbon concentrations above γ_C>0.17, indicating that tiny carbides are nucleating and effectively hinder the diffusion of carbon atoms. Consequently, the diffusion coefficient obtained at 613K for carburizing in C_2H_2 may be interpreted as an effective diffusion coefficient encompassing the presence of coherent carbides.

It is assumed that the carburizing kinetics in the chosen C_2H_2/H_2 mixture is less controlled by the rate of the surface reaction as compared to the chosen CO/H_2 mixture. However, from a coupling between the lowering in temperature (180K) and reduction in diffusion coefficient (factor 100), it is difficult to conclude whether the diffusion coefficient obtained at 613K is relatively high.

4.8 Conclusion

Three methods for the determination of composition dependent diffusion coefficients by measuring the initial rate of sorption were analyzed by simulation of the sorption behavior at high temperature. The simulations revealed that the best approximation of the composition dependent diffusivity is obtained for an incremental sorption method, in which the surface composition is successively increased by small increments and where each increment is preceded by a homogenization of the carbon profile in the sample. The presented experimental results indicate that the diffusion coefficient of carbon in expanded austenite increases with carbon concentration, in agreement with trends observed in the literature for diffusion of carbon in Fe-C austenite and the diffusion of nitrogen in expanded austenite. Moreover, from inverse modeling, it is suggested that nucleation of coherent carbides occurs for carbon contents above γ_C>0.17, which results in a lowering of the concentration dependent diffusion coefficient.

5 Decomposition of expanded austenite

In this chapter the decomposition of carbon-saturated expanded austenite was studied by systematic differential thermal analysis (DTA) on compositionally graded AISI 316L stainless steel powders and flakes. The nature of the decomposition products, carbides of the form $M_{23}C_6$ and M_7C_3, were evaluated by X-ray diffraction, light optical microscopy, scanning electron microscopy (SEM) and thermodynamic modelling. It was found that if precipitation of $M_{23}C_6$ occurs, it precedes the precipitation of M_7C_3 and that the carbides were a mixture of Cr and Fe carbides. Moreover, the formation of M_7C_3 is possible only for carbon contents above a certain threshold value (1wt.%), in accordance with ThermoCalc calculations. The rate limiting step for decomposition is suggested to be the diffusion of substitutional metal atoms significantly influenced by nucleation of precursors. The influence of thermal history, carbon content, sample geometry and compressive stresses is evaluated.

5.1 Introduction

Investigating the carburization of stainless steel and the associated microstructural changes in the carburized case are of importance for optimising the deliberate surface engineering of these materials as well as preventing the unwanted catastrophic corrosion, metal dusting [4, 30]. At relatively low temperatures, say <823K, austenitic stainless steel can be deliberately carburized in para-equilibrium with a gaseous environment, leading to the development of an austenitic zone supersaturated with carbon, without the development of carbides [33, 34]. This zone of expanded austenite has a high hardness and favourable anti-galling and wear resistant properties combined with the unaffected anti-corrosion properties. The thermal stability of expanded austenite with respect to carbide formation and associated Cr depletion of the surrounding matrix, is of particular interest to maintain the advantageous corrosion properties of stainless steel. The carbides anticipated to develop upon the decomposition of expanded austenite are of type $M_{23}C_6$, M_7C_3 and M_3C_2, where M stands for a mixture of Fe and Cr atoms. Recently, the development of a M_5C_2 type (Hagg) carbide was reported [38]. Carbide development also occurs in the stage prior to catastrophic carburizing (metal dusting), where it can be in competition with oxide formation, depending on the composition of the carburizing atmosphere, i.e. oxidizing or reducing [29, 31, 32]. Hitherto, the metal dusting corrosion mechanism has not been associated with the development and subsequent decomposition of carbon expanded austenite, even though carburization and carbide formation are significantly involved in the metal dusting mechanism.

Several effects are likely to have an impact on the decomposition kinetics of carbon expanded austenite: i) compressive stresses developing in the carburized zone as expanded austenite layers are growing into an uncarburized substrate, ii) the thermal history of the material since the decomposition is a thermally activated process, iii) the carbon content of the investigated material is to be accounted for since there is a larger driving force towards precipitation because of a larger supersaturation iv) geometric effects such as the surface, interfaces and grain boundaries, v) hypothetical coherent precipitates formed during carburization would act as precursors and promote the precipitation during the subsequent heat treatment. Thus the interpretation is at least affected by the interplay of these five parameters.

In order to be able to make reliable forecasts of the time to the onset of metal dusting,

and possibly allow for a thorough investigation of the parameter influencing the kinetics of the (catastrophic) carburizing process it is necessary to include the development and decomposition of carbon expanded austenite. The chapter is subdivided in two sections. In the first section, kinetic parameters relating to the decomposition of carbon expanded austenite are obtained. Secondly, the isolated effect of compositionally induced stresses on the decomposition kinetics is touched upon.

5.2 Experimental

5.2.1 Gaseous carburizing by thermogravimetry

Powders and flakes of stainless steel AISI 316L were used for investigating the stability of expanded austenite. Five different powder sizes were used: max 1.2μm (flakes), max 5μm, max 20μm, max 45μm and max 150μm. Gaseous carburizing was performed in a Netzsch STA 449C thermal analyzer. For recrystallization and austenitization the stainless steel powders were heated to 1353K [1] at a heating rate of 30 K/min and upon reaching this temperature immediately cooled in pure H_2 to the carburizing temperature. During austenitization any deformation-induced martensite formed by manufacturing of the samples, was totally transformed to austenite. Furthermore, as a consequence of the heat treatment in pure H_2, the powder surfaces were activated to allow gaseous carburizing. The carburizing atmosphere contained a mixture of CO, H_2 and N_2 or C_2H_2, H_2 and N_2. The flows of carbon mono-oxide and hydrogen were adjusted with mass flow controllers: 20 ml CO/min, 30 ml H_2/min and 5 mL N_2/min, and of acetylene and hydrogen; 50 ml C_2H_2/min, 50 ml H_2/min and 5 mL N_2/min. Powders were carburized at 743K for different amounts of time ranging from 4-50 hours, flakes were carburized at 613K for different amounts of time ranging from 2-18 hours. Accordingly various carbon contents were obtained. All average carbon contents in the as-carburized materials as well as their thermal history are given in Table 5.1.

Material	Duration (h)	Temp. (K)	Gas	y_C	[C] (at.%)	[C] (wt.%)
1.2μm flakes	2	613	C_2H_2	0.120	10.7	2.5
	12	613	C_2H_2	0.250	20.0	5.2
	18	613	C_2H_2	0.280	22.2	6.0
5μm	8	743	CO	0.070	6.5	1.5
20μm	4	743	CO	0.056	5.3	1.2
	8	743	CO	0.092	8.4	1.9
	16	743	CO	0.150	13.1	3.2
45μm	16	743	CO	0.055	5.2	1.2
	30	743	CO	0.094	8.5	2.0
	50	743	CO	0.188	15.8	3.99
150μm	20	743	CO	0.071	6.6	1.5
	43	743	CO	0.074	6.9	1.6

Table 5.1: Material, carburizing time, temperature, applied carburizing agent and average carbon content expressed as y_C, the number of carbon atoms per 100 metal atoms (or, equivalently, the fraction of occupied octahedral interstices in f.c.c), as at.% C and as wt.% C.

5.2.2 Thermal analysis

Isochronal annealing of the expanded austenite powders and flakes was performed in the Netzsch STA449C thermal analyzer using various heating rates. Experiments were carried out in an inert Ar atmosphere with a flow of 20 mL/min. Constant heating rates within the range 10-35 K/min were applied thus enabling kinetic analysis. The starting temperature was 300K and the end

[1] Stainless steel flakes were only heated to 1273K to prevent sintering.

temperature was 1353K for all isochronal annealing experiments. The typical sample mass used for each experiment was 100 mg. A baseline was recorded by heating the decomposed sample according to the gas/temperature program of the first run. Hence, instrumental and buoyancy effects could be corrected for. The 45μm powder which had been carburized for 30 hours at 743K was subdivided in 20 portions and subsequently heated to 20 temperatures covering the temperature range where decomposition occurred, followed by immediate cooling. Temperature steps of 10K were applied. Heating was carried out at a rate of 20 K/min and cooling at a rate of 50 K/min. X-ray diffraction was applied on the 20 annealed portions in order to reveal the decomposition as a function of temperature. A similar temperature resolved analysis was performed on AISI 316L stainless steel flakes which had been carburized to saturation content, 5.3wt.%, in C_2H_2+H_2 at 613K for 18 hours. Kinetic analysis was carried out applying a Kissinger-like method. For details about kinetic analysis the interested reader is referred to [41, 42].

5.2.3 X-ray diffraction

X-ray diffraction was applied for the identification of the as-prepared and carburized material. The instrument was a Bruker AXS (Bruker AXS GmbH, Germany) D8 X-ray diffractometer, equipped with a Cr anode and a set of Göbel mirrors in the incident beam. The carburized powders/flakes were submerged in ethanol, and the slurry was smeared on a glass-plate. After evaporation of the ethanol the samples were investigated with XRD.

5.3 Results and Interpretation

5.3.1 Carburized powders

X-ray diffractograms of the as-carburized AISI 316L powders and the austenitized reference powder are given in Figure 5.1. A shift of the austenite f.c.c reflections to lower diffraction angles is observed for all carburised specimens; this is a direct consequence of the dissolution of carbon atoms, i.e. the development of γ_C. The peak shift is also influenced by i) compressive stresses which give rise to an hkl dependent peak shift to lower diffraction angles and ii) the occurrence of stacking faults which give rise to an hkl dependent peak shift with either negative or positive sign [36].

Broad $\gamma_C(111)$ and $\gamma_C(200)$ diffraction peaks are observed for the 45μm and 150μm powder. The broadening can be attributed to variations in carbon content in the volume probed by the incident X-ray beam in the various size fractions of the carburised powder and the asymmetry can be ascribed to composition gradients. Relatively small particles can be homogeneously carburized with carbon content depending on their size, where relatively large particles can be carbon-free in their core. The uncarburized austenite core is somewhat identifiable which implies that the information depth exceeds the extent of the carburised layer, hence the through-carburising of the powder has not occurred for all particles. X-ray diffraction peaks of the 20μm powder are slightly broadened, especially the $\gamma_C(220)$ is asymmetrical towards higher diffraction angles. As compared to the 45μm and 150μm powder the carbon distribution is fairly homogeneous. The effect of longer carburizing times, thus higher carbon content, can be observed to give rise to a larger peak shift towards lower Bragg angles. Concurrently, the γ_C peaks become narrower; this can be attributed to a more uniform carbon distribution in y_C, i.e. the composition gradient (and the concomitant stress gradient) becomes shallower.

5.3.2 Isochronal annealing of carbon expanded austenite

The DTA curves at a heating rate of 25 K/min for the 20μm and 45μm powders with different carbon contents and thermal exposures are depicted in Figure 5.2. Also shown in Figure 5.2 are the DTA curves at a heating rate of 25 K/min for the 150μm powder with similar carbon content but different thermal exposures. All samples contain an exothermic signal which spans over a range from approximately 800K to 1200K. The exothermic signal is apparently a superposition of three curves with peak positions approximately at T_1= 950K, T_2=1050K and T_3=1120K for a heating rate of 25K/min. The peak positions will be designated $Peak_1$, $Peak_2$ and $Peak_3$.

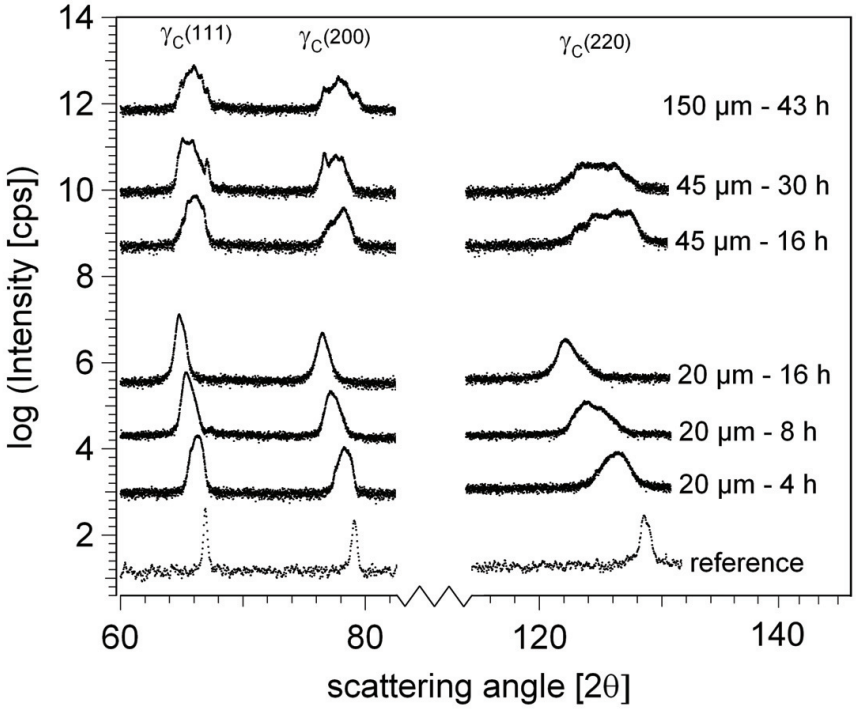

Figure 5.1: X-ray diffractograms of the austenitized reference and carburized (743K in CO/H_2) 20μm, 45μm and 150μm powders.

The exothermic signals have a main peak defining the temperature at which the maximum rate of transformation occurs in the material. Evidently, the main peak is shifted towards lower temperatures as the thermal exposure and hence the carbon content is increased. The shift is increasingly pronounced as the powder size decreases. The width of the main DTA-peak is affected by differences in carbon content due to the powder size distribution. Since no weight loss/gain occurred during the isochronal annealing the DTA peaks are solely attributed to solid state phase transformations within the samples.

5.3.3 Decomposed powders

The decomposed powders investigated with X-ray diffraction had been heated twice to 1353K, once for the actual decomposition and once for the acquisition of a baseline. X-ray diffractograms of the decomposed AISI 316L powers are given in Figure 5.3 for annealing in Ar. Generally, decomposed AISI 316L powders consist of carbides and austenite; expanded austenite is no longer present. The X-ray diffractograms of the decomposed low carbon content samples, the 20μm carburized for 4 h and the 45μm carburized for 16 h, indicate the presence of carbides of the type $M_{23}C_6$ and a small amount of M_7C_3 type. In the 20μm sample carburized for 8 h and in the 45μm sample carburized for 30 h, carbides of the type M_7C_3 and a small amount of $M_{23}C_6$ type is observed. In the 150μm sample carburized for 43 h comparable amounts of carbide of type $M_{23}C_6$ and of type M_7C_3 are present. In the high carbon content 20μm sample carburized for 16 h the only carbide present is of M_7C_3 type.

As compared to the indicated peak positions for $M_{23}C_6$, the experimental Bragg peaks are shifted to higher scattering angles and a better correspondence with $Cr_{15}Fe_8C_6$ is evident. This indicates that approximately 34% of the metallic part in this carbide is iron. Similarly, as compared to the indicated peak positions for M_7C_3, the experimental Bragg peaks are shifted to higher scattering angles which also indicate the presence of iron in these carbides. Since no reference X-ray diffractograms exist of $(Cr_xFe_y)C_3$, it is difficult to estimate the iron content

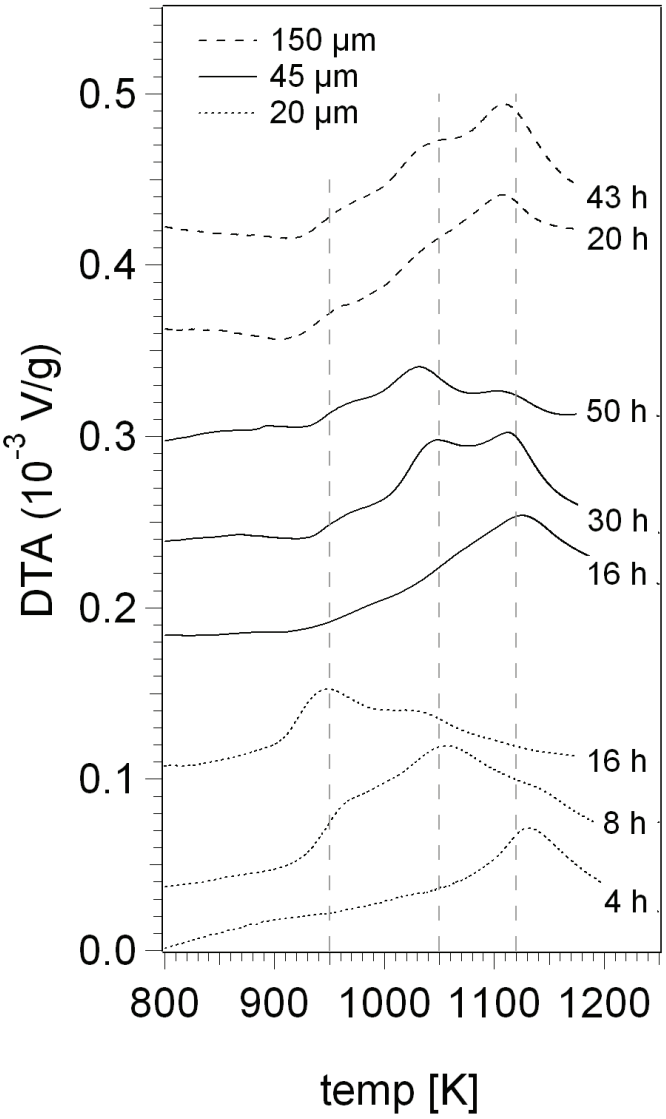

Figure 5.2: DTA experiments on AISI 316L 20μm, 45μm and 150μm powders carburized in CO/H_2 at 743K. DTA curves correspond to a heating rate of 25K/min. The dashed vertical lines indicates positions of $Peak_1$(950K), $Peak_2$(1050K) and $Peak_3$(1120K).

in this carbide. In general, the carbides are mixed chromium-iron carbides of type $(Cr_xFe_y)C_z$ [17] and the carbides are therefore referred to as $M_{23}C_6$ and M_7C_3. It is interesting to note that the reflection at approximately 60 degrees (M_7C_3) in the 20μm powder is shifted to higher diffraction angles as the carbon content is enhanced. The same trend, although less pronounced, is observed for the 45μm powder. This indicates that the iron content in the carbides is increasing with carbon content as expected, since more carbon is present, but the Cr content is limited.

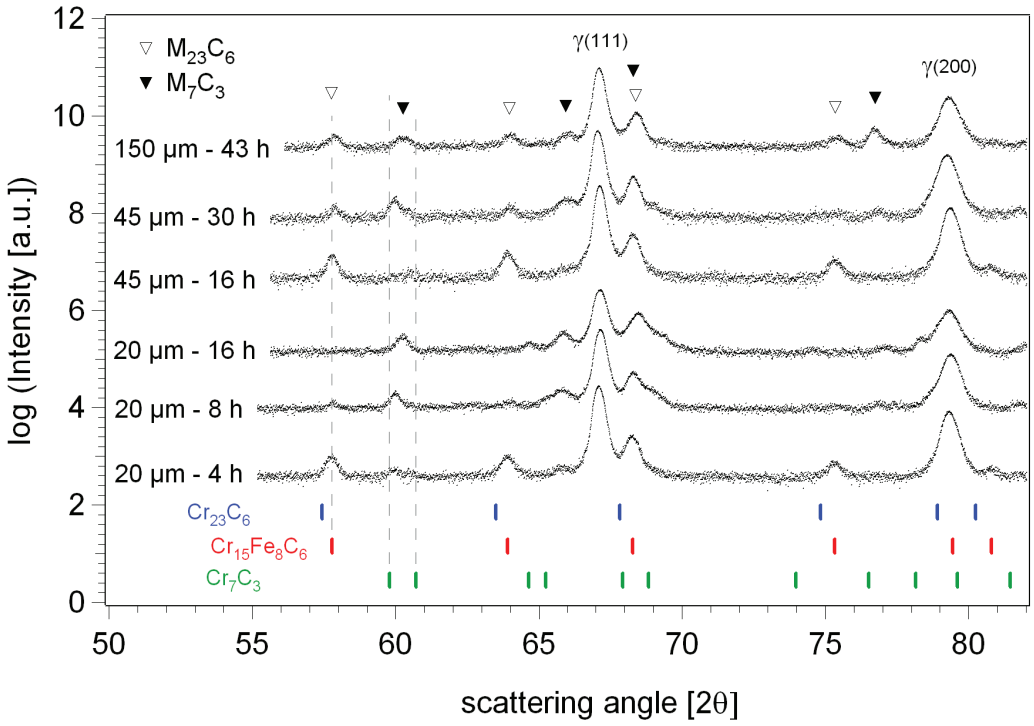

Figure 5.3: X-ray diffractograms of decomposed AISI 316L powders with different carbon contents. Also indicated are the peak positions for $M_{23}C_6$, M_7C_3 and $Cr_{15}Fe_8C_6$.

In Figure 5.4, X-ray diffractograms of the 45μm powder which had been carburized for 30 hours at 743K, subdivided in twenty portions and subsequently decomposed at twenty different temperatures are presented. The figure illustrates the development of carbide precipitation as a function of temperature. The temperature resolved analysis allows for a detailed insight into the chronology of carbide precipitation. Several occurrences are remarked; the precipitation of $M_{23}C_6$ happens gradually from 920K to 1040K, this is verified by the reflection around 58 degrees increasing in intensity in this temperature range. The gradual precipitation or coarsening fits well with the exothermic signal of the corresponding DTA curve in Figure 5.2 (left shoulder on $Peak_2$). The reflection at 58 degrees increases in intensity passing 1050K ($Peak_2$). This reflects the first main peak in the DTA curve which on this basis can be assigned to the formation of $M_{23}C_6$.

At 1090K an XRD reflection appears at 60 degrees which can be assigned to M_7C_3. In the temperature range from 1090K to 1110K the precipitation of M_7C_3 is gradually developing until at 1110K where the intensity of the XRD reflection at 69 degrees increases in intensity. Comparison to the DTA curve in Figure 5.2, allows relating the second main DTA peak ($Peak_3$) for 45μm 30 h to the precipitation of M_7C_3. At 1353K the decomposed powder contains mainly M_7C_3 and a small amount of $M_{23}C_6$. Notice that the iron content in the M_7C_3 carbide has decreased at 1353K as compared to the X-ray diffractogram collected at 1113K. From the temperature resolved analysis it is evident that the two main exothermic signals in the DTA curve can be ascribed to the formation of the carbides of the type $M_{23}C_6$ and M_7C_3. No temperature resolved

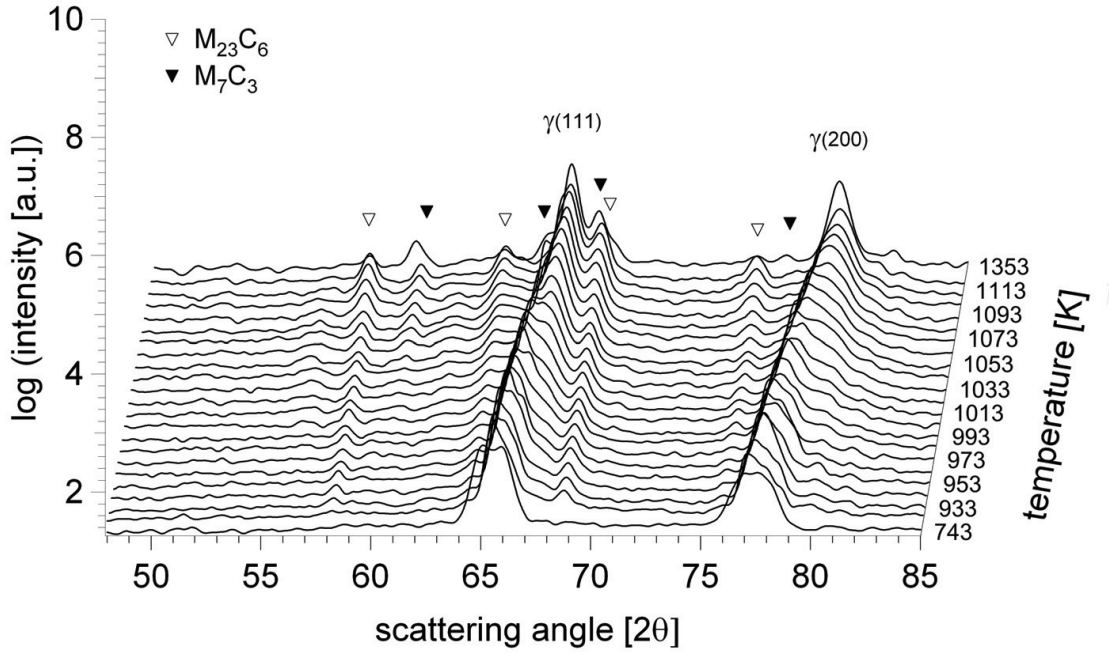

Figure 5.4: X-ray diffractograms of 45μm powder which had been carburized for 30 hours at 743K, and subsequently annealed at twenty different temperatures in the decomposition range.

analysis of the decomposition for the remaining powders was performed. Thus, the assignment of the exothermic peaks to the precipitation of distinct carbides is based on the final decomposition product(s) and thermodynamic calculations.

5.3.4 Thermodynamic calculations

In order to arrive at an interpretation of the observed effects, equilibrium calculations for carburized samples with different carbon contents, 1wt.% C, 2wt.% C and 4wt.% C were made with ThermoCalc [60]. Such calculations predict the preferred equilibrium decomposition products as a function of carbon content and temperature and are given for three carbon contents in Figure 5.5. Phases other than f.c.c, b.c.c, liquid, $M_{23}C_6$ and M_7C_3 have been suppressed in the calculations. The evolutions of the compositions of the carbides are also shown; the equilibrium compositions of the carbides, i.e. Fe and Cr contents follow also from ThermoCalc and are included in Figure 5.5. Clearly, in the powders with low carbon contents (1wt.%) predominant precipitation of $M_{23}C_6$ can be expected during the DTA investigation (Figure 5.5a). The content of M_7C_3 in these samples should be limited and its development could have occurred in regions with higher C content than average at the highest temperature reached, in accordance with the results given in Figure 5.3. In powders with higher carbon content (>2wt.%) both $M_{23}C_6$ and M_7C_3 can develop at low temperatures up to approximately 800 K (Figure 5.5c). Beyond this temperature $M_{23}C_6$ is expected to be converted to M_7C_3. It is tempting to attribute the exothermal heat effect at 1050 K ($Peak_2$) in Figure 5.2 to this conversion of $M_{23}C_6$ developed at lower temperature. Then, the exothermic reaction at lower temperature for the powders with higher carbon content should be attributed to the simultaneous development of $M_{23}C_6$ and M_7C_3. This interpretation is consistent with dominance of M_7C_3 in the diffractogram for the decomposed powders with higher carbon contents.

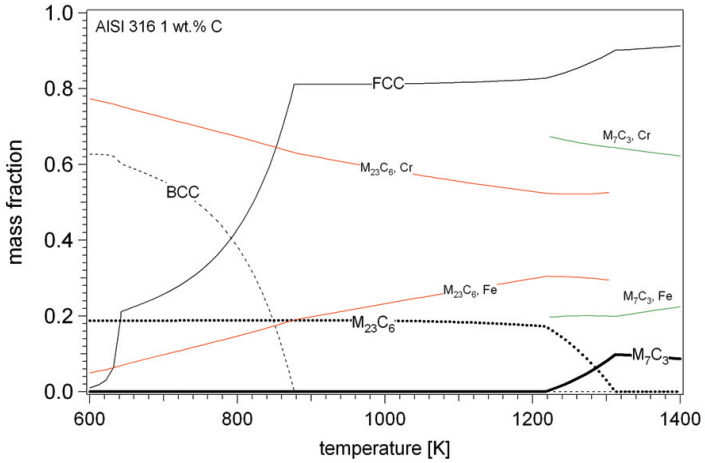

a) AISI 316 1wt.% C

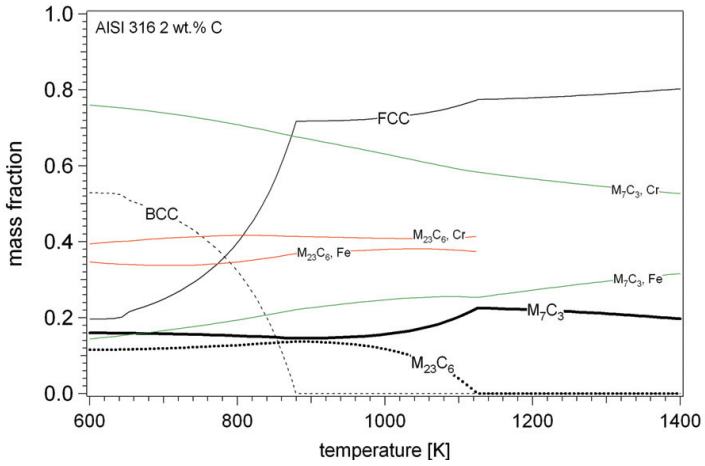

b) AISI 316 2wt.% C

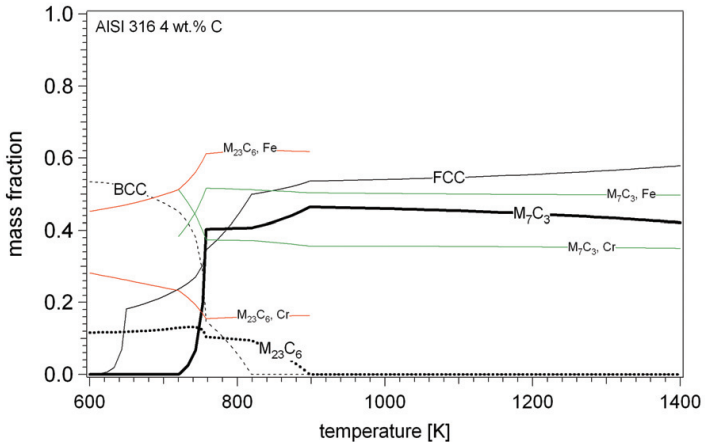

c) AISI 316 4wt.% C

Figure 5.5: ThermoCalc equilibrium calculations illustrating the stable phases in carbon expanded austenite (a. 1wt.% C, b. 2wt.% C and c. 4wt.% C) as a function of temperature. Included are also the evolutions of the compositions of the carbides, i.e. Fe and Cr contents.

5.3.5 Kinetic analysis

Kinetic analysis was carried out for the two identified reactions i.e. the decomposition reaction involving the development of the two carbides $M_{23}C_6$ and M_7C_3. Plots of $\ln\frac{T_m^2}{\phi}$ versus $\frac{1}{T_m}$ for the decomposition reactions are given in Figure 5.6. The DTA peak positions (T_m) used in the formula were found by fitting the DTA signal with a Gaussian function incorporating the superposition of three exothermic peaks. From the slopes of the fitted straight lines the activation energies collected in Table 5.2 were obtained.

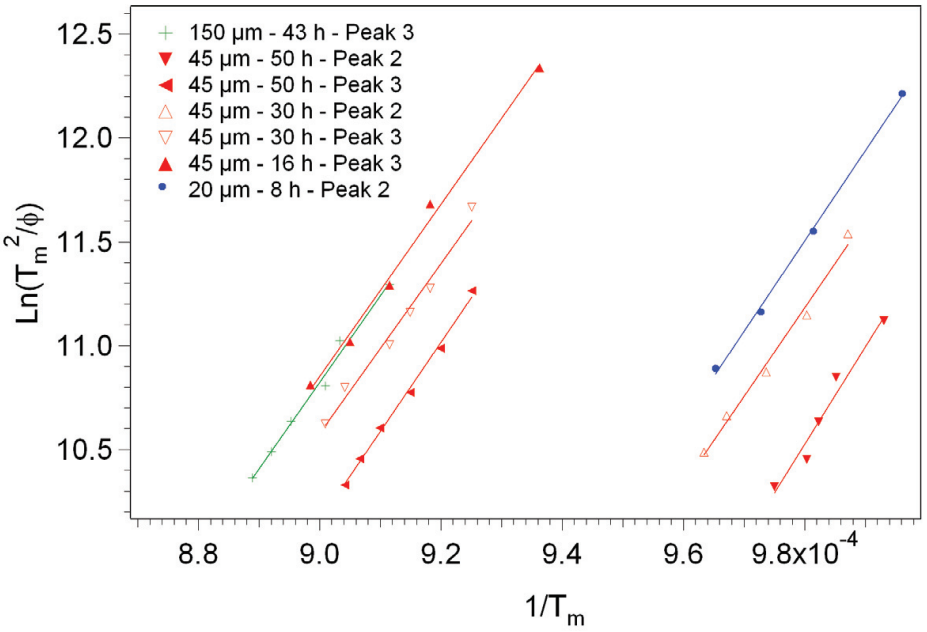

Figure 5.6: Plots of $\ln\frac{T_m^2}{\phi}$ versus $\frac{1}{T_m}$ for the decomposition of carbon expanded austenite in AISI 316L powders.

Sample	Peak$_2$ (kJ/mol)	Peak$_3$ (kJ/mol)	Peak position (K)
150μm 43h		345±18	1107
45μm 50h	299±58	357±12	1030/1110
45μm 30h	390±45	340±22	1050/1110
45μm 16h		344±16	1125
20μm 16h			950
20μm 8h	361±11		1050

Table 5.2: Activation energies for the decomposition reactions. All powders have 350kJ/mol as a possible activation energy.

Literature values for activation energies for volume and grain boundary diffusion of Cr and Fe in stainless steel alloys are listed in Table 5.3. The established activation energies are systematically higher than those for volume diffusion, which indicates that nucleation plays a role. The influence of thermal exposure during carburization is supposed to affect the first exothermic reaction. Accordingly, the lowest activation energy is found for the 45μm powder exposed for 50h.

Element	Volume (kJ/mol)	Grain b. (kJ/mol)
Cr	263.8	152.2
Fe	279.2	177.2

Table 5.3: Activation energies for substitutional diffusion [1, 2].

5.4 Discussion

As previously mentioned, several effects are likely to have an impact on the decomposition kinetics of carbon expanded austenite. In the following it is attempted to clarify the isolated effect of the parameters; geometry, carbon content, thermal exposure and carburizing agent. The possible effect of residual stresses is treated in a subsequent section.

5.4.1 Geometric effects

The decomposition of expanded austenite involves the precipitation of carbide precipitates. Precipitates are formed on favourable nucleation sites as surfaces, grain boundaries and stacking faults and must be incorporated in the analysis. Since reducing the powder size increases the relative surface area, it would be expected that precipitation is enhanced on 20μm powders as compared to 45μm powders. The influence of surface area is observed in Figure 5.2 for CO carburized powders. For low carbon contents (approx. 1.5wt.%), the 20μm 4h and 45μm 16h powders show comparable DTA curves. At medium carbon contents (approx. 2.5wt.%) the 20μm 8h and 45μm 30h DTA curves differ more significantly in that the nucleation of carbides is shifted to lower temperatures in the 20μm powder, irrespective of the prolonged thermal exposure of the 45μm powder. This is a clear effect of the surface area. This effect becomes even more pronounced in the high carbon content samples (approx. 3.5wt.%), and simultaneously, the effect of thermal exposure becomes less significant.

In Figure 5.7, X-ray diffractograms of carburized 20μm 16h and 5μm 8h powders are shown. The samples have been carburized in an identical mixture of CO and H_2 at 743K. As verified by inspection of Figure 5.7, precipitation of carbides has not occurred in the 20μm sample during carburization. On the other hand, in the 5μm carburized for 8 hours, precipitation of carbides has occurred as verified by the presence of reflections pertaining to carbide of the form $M_{23}C_6$. This illustrates how precipitation is strongly favoured in the high surface area sample indicating that nucleation at the surface is taking place. Notice that the carbon content in the 5μm samples is 1.5wt.% which is lower than in the 20μm sample, 3.2wt.%. It puts into perspective the relatively low significance of the carbon content and the thermal exposure as compared to the total surface area. It is expected that fewer compositionally induced stresses are present in the 5μm powder. If volume changes are associated with carbide precipitation, the nucleation at free surfaces is affected and may explain the strongly favoured nucleation in the 5μm powder.

5.4.2 Carbon content

The thermogravimetrically measured carbon uptake during carburization represents an average value. However, since the carbon atoms are usually not uniformly distributed, unless a homogenization step has succeeded the carburization, it is difficult to asses the actual carbon content in the carburized zone. Moreover, as a consequence of the powder size distribution, smaller particles are expected to have higher (average) carbon content than larger particles. In order to estimate the effect of carbon content on carbide precipitations the composition gradient has to be minimized. Accordingly, it was attempted to produce two powders with different carbon contents and similar thermal exposure. To this end, the 20μm 8h powder was annealed for 8 hours at 743K in a flow of inert argon as to reach the same thermal exposure as the 20μm 16 h. The thermal treatment of the 20μm 8 h powder resulted in the precipitation of carbides of type $M_{23}C_6$, and as a consequence, f.c.c. reflections were shifted to higher Bragg angles, consistent with a lower carbon content in γ_C. X-ray diffractograms of the 20μm powders are shown in Figure 5.8. No obvious explanation exists for the reason as to why the precipitation/nucleation is favoured in

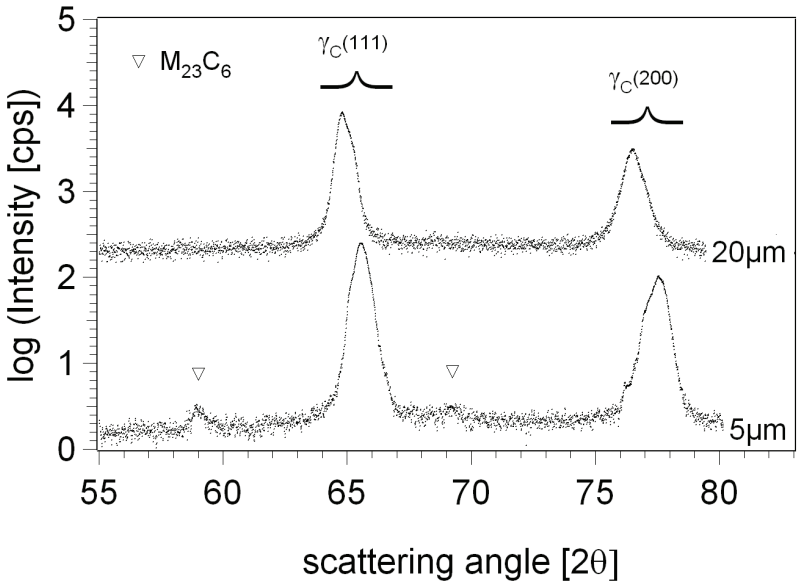

Figure 5.7: X-ray diffractograms of carburized 20μm (3.2wt.%)- and 5μm (1.5wt.%) powders. The 5μm powder has been carburized for 8 hours and the 20μm for 16 hours. Powders were carburized in a identical mixture of CO(20mL/min) and $M_{23}C_6$(30mL/min) at 743K. A geometric effect causes precipitation of $M_{23}C_6$ carbides in the 5μm powder.

the situation without the applied carburizing gas. With regard to nucleation at the surface, the presence of carbon containing gas species at the surface could prevent surface diffusion of Cr and Fe and the involved surface reconstruction. Furthermore, a carbon containing gasflow around the sample may cancel out spontaneous lateral fluctuations in carbon content on the surface that are necessary for nucleation. For nucleation at grain boundaries the flux of carbon through the grain boundaries might influence the segregation effects adjacent to the boundaries, which play a role of importance in the nucleation mechanism at these locations. Otherwise, intermediate cooling and re-heating to the annealing temperature could offer an explanation. Anyway, since decomposition had already occurred, it was meaningless to perform the isochronal annealing experiment for comparison. Hence, it is difficult/impossible to distinguish between the effect of carbon content and thermal exposure.

5.4.3 Thermal exposure

Since the decomposition of expanded austenite is a thermally activated process, an extended thermal exposure is bound to shift the precipitation temperature to lower temperatures. In order to quantify the effect of thermal exposure on precipitation temperature, DTA experiments were carried out on 150μm powders and flakes (1.2μm). In Figure 5.2, DTA curves were compared for two 150μm powders with an average carbon content of approximately 1.5wt.% exposed differently during carburization for 20 and 43 hours. It is observed that the exothermic peak at 1050K is more pronounced for the sample exposed for 43 hours. The shift of precipitation towards lower temperatures may be attributed the presence of carbide precursors formed during the prolonged carburizing/thermal exposure. Also notice that the main peak at 1107K is not shifted significantly.

In Figure 5.9 DTA curves during isochronal annealing of C_2H_2 carburized flakes are depicted. The main DTA exothermic peak of the flakes which have been carburized for 2 hours is around 1050K, coincident with $Peak_3$ for the powders. Prolonged carburizing for 12 hours and 18 hours results in a shift of the main exothermic peak to what appears to be a maximum shift, or minimum precipitation temperature, around 775K. Included in Figure 5.9 is the DTA curve on

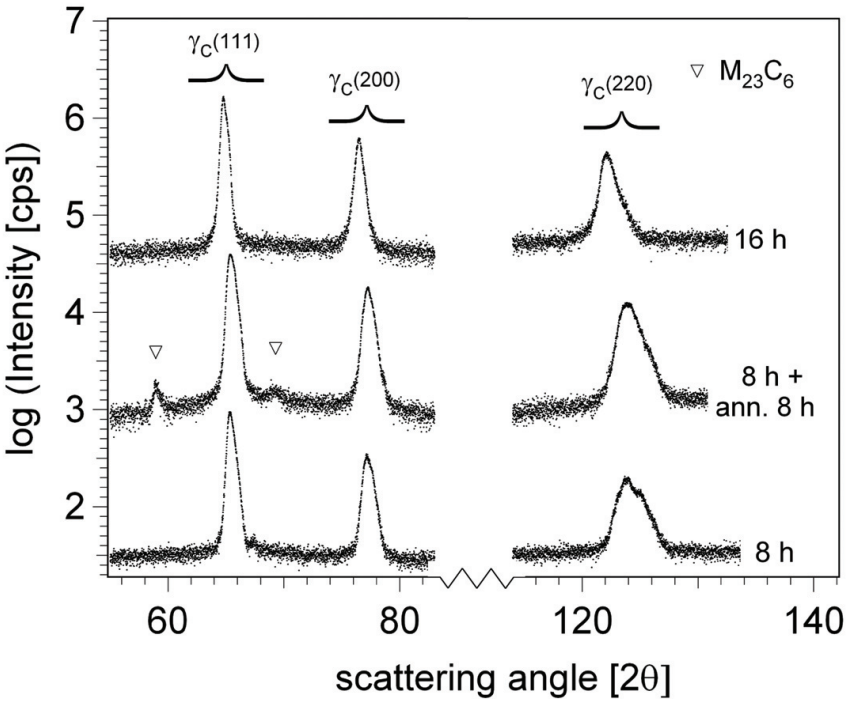

Figure 5.8: X-ray diffractograms of the 20μm powders carburized at 743K for 8h and 16h and the subsequent annealed 20μm sample.

AISI 316L 20μm powder carburized in CO at 743K for 16 hours. Apparently, the precipitation temperature during isochronal annealing of C_2H_2 carburized flakes is shifted to an even lower temperature as an extension of the trend observed in Figure 5.2 for CO carburized powders.

The mass gain curve obtained during carburization of the flakes were shown in Figure 3.7. It is observed that that no further mass gain is obtained on prolonged exposure from 12 hours to 18 hours. Consequently, the shift in precipitation temperature observed for prolonged exposure from 12 hours to 18 hours cannot be ascribed to an increase in carbon content. Merely the prolonged exposure leads to an levelling of the carbon atoms over the thickness of the flakes as indicated by the more symmetric X-ray diffraction peak on prolonged exposure, presented in Figure 3.6. Accordingly, the shift in precipitation temperature can entirely be ascribed to the effect of thermal exposure.

5.4.4 Carburizing agent

Several observations indicated the possible influence of the carburizing agent on the decomposition of carbon expanded austenite. In this section the hypothesis that coherent carbides, or carbon clusters, are precipitating during carburization in an atmosphere of C_2H_2/H_2 is tested. To this end, AISI 316L stainless steel flakes were carburized in C_2H_2/H_2 at 613K. It was necessary to apply a carburizing temperature as low as 613K to avoid precipitation of carbides in the flakes during carburization in C_2H_2/H_2, which in principle could be ascribed the carburizing agent and/or the relative increased surface area of the 1.2μm thin flakes as compared to the previously discussed powders.

Generally it is observed that X-ray diffraction peaks obtained on C_2H_2 carburized samples at 613K are broad compared to samples carburized in CO at 743K. At first glance this could be attributed to a lower level of homogenization due to the significantly lower carburizing temperature applied for C_2H_2 carburization. However, even after a subsequent homogenization interval the X-ray diffraction peaks remain broad. In Figure 5.10, X-ray diffractograms of the previously described C_2H_2 (18h) carburized flakes and 20μm powder carburized in CO at 743K for 16 hours

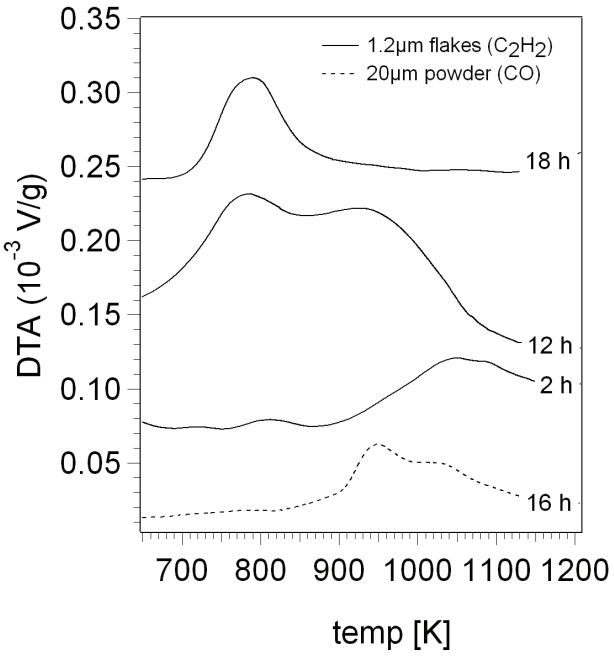

Figure 5.9: Isochronal annealing of carburized AISI 316L stainless steel flakes. The flakes have been carburized for 2, 12 and 18 hours at 613K. Included is DTA curve on AISI 316L 20μm powder carburized in CO at 743K for 16 hours. DTA curves correspond to a heating rate of 25K/min. Prolonged exposure causes a shift in the precipitation of carbides towards lower temperatures.

are compared.

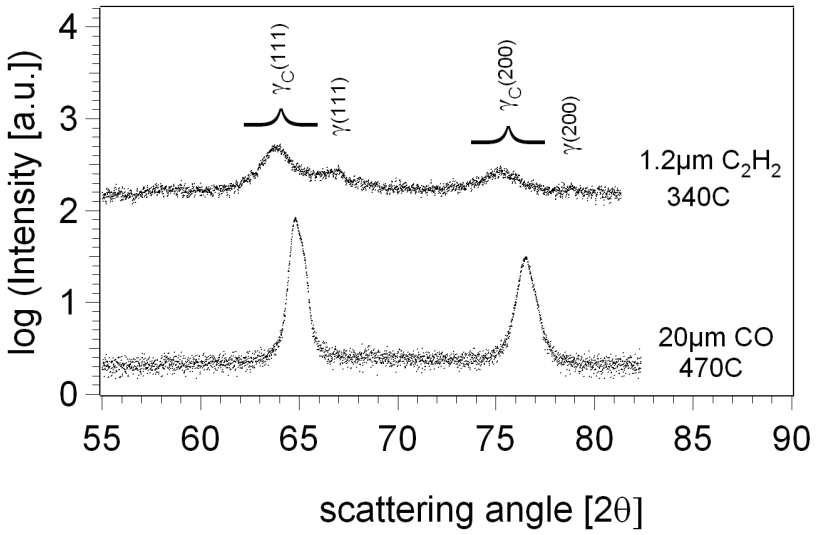

Figure 5.10: X-ray diffractograms of AISI 316L flakes carburized at 613K for 18h in a mixture of C_2H_2/H_2 and 20μm powder carburized in a mixture of CO/H_2 at 743K for 16h.

In the CO carburized sample, the $\gamma_C(111)$ reflection outset at 64.2 degrees and rises steeply. In contrast, the $\gamma_C(111)$ reflection of the C_2H_2 carburized sample, which begins at 61.8 degrees, has a distinct left shoulder and rises less steeply. It is anticipated that tiny carbides are precipitating already during carburization in C_2H_2. Due to their tiny size they diffract coherently with the matrix and the carbides are not observed as diffraction peaks, thus are not identifiable with XRD. The left shoulder on the $\gamma_C(111)$ reflection of the C_2H_2 carburized sample could represent coherent or tiny carbides. The carbon atoms bound in coherent carbides and/or the accompanied expansion would lead to an apparent increase in carbon solubility. This could contribute to the explanation of increased solubility in C_2H_2 carburized flakes as compared to CO carburized powders. If tiny carbides are formed during carburization in C_2H_2 they might act as precursors for carbides formed during isochronal annealing. It is expected that the presence of precursors would enhance the precipitation, and consequently contribute to the early main exothermic peak observed during isochronal annealing of C_2H_2 carburized flakes (Figure 5.9). The large difference in driving force towards carbide nucleation is further emphasized by comparing the maximal solubility of carbon without precipitation of carbides in C_2H_2 carburized 7.5μm foil and CO-carburized 20μm powder. Within the C_2H_2-carburized 7.5μm foil, the maximal solubility of carbon in the f.c.c. structure was 3.5wt.%. In the relative high surface area CO-carburized 20μm powder, the maximal solubility was 3.8wt.%. Despite the much larger density of nucleation sites, and the significantly higher carburizing temperature (743K vs. 693K), the CO atmosphere prevents nucleation of carbides for prolonged carburizing (16h vs. 80min). The early carbide nucleation during carburization in C_2H_2 could be explained by the instantaneous build up of carbon in the near surface zone caused by the enormous carburizing potential and/or fast decomposition of C_2H_2. In contrast, the catalytic decomposition of CO on the sample surface could be too sluggish and the associated carburizing potential relatively low. Moreover, the presence of oxygen in the CO molecule may retard the Cr-carbide nucleation due to the high affinity of Cr to O.

In Figure 5.11, X-ray diffractograms of 1.2μm flakes which had been carburized to saturation (6.0wt.%) for 18 hours at 613K, subdivided in twenty portions and subsequently decomposed at twenty different temperatures are presented. The figure illustrates the development of carbide precipitation as a function of temperature. Precipitation of M_7C_3 occurs around 800K as verified

by the reflections at 60 and 69 degrees increasing in intensity. The precipitation temperature is in agreement with the exothermic signal of the corresponding DTA curve in Figure 5.9, which can be ascribed to the formation of M_7C_3. Observe that M_7C_3 is the preferred decomposition product as predicted by the Thermocalc calculations presented in Figure 5.5c.

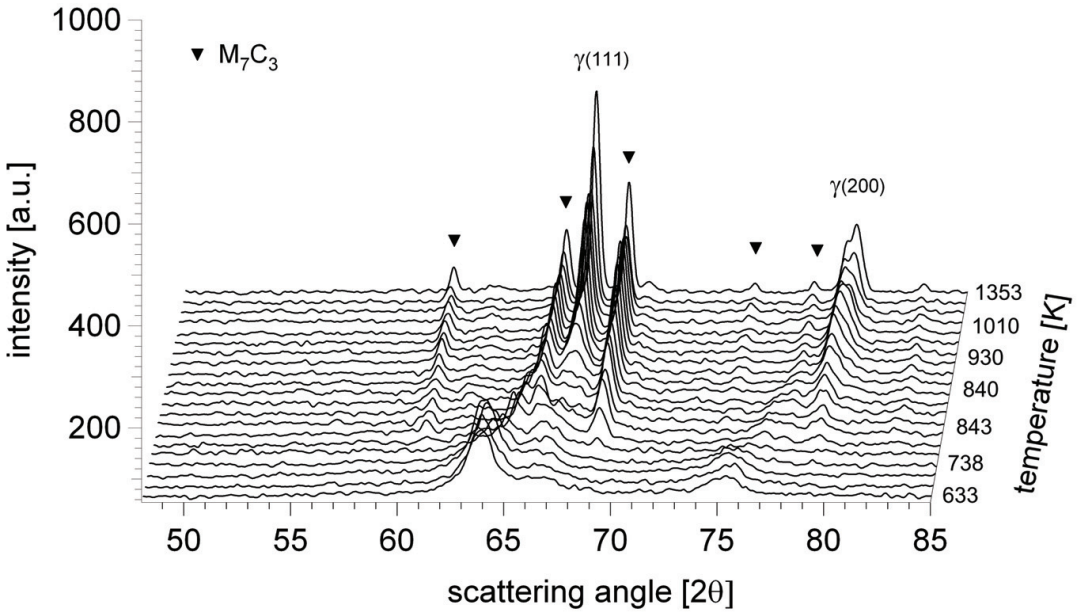

Figure 5.11: X-ray diffractograms of 1.2μm flakes which had been carburized to saturation (6.0wt.%) for 18 hours at 613K, and subsequently annealed at twenty different temperatures in the decomposition range.

5.5 Conclusion

The decomposition of expanded austenite, γ_C, into austenite and carbides of the type $M_{23}C_6$ and M_7C_3 was investigated for AISI 316L flakes and powders with different particles sizes and carbon contents. It was observed that if precipitation of $M_{23}C_6$ occurs, it precedes the precipitation of M_7C_3. Moreover, the formation of M_7C_3 is possible only for carbon contents above a certain threshold value (approx. 1wt.%). This was observed to be in accordance with ThermoCalc calculations. The formed carbides were a mixture of Cr and Fe carbides with a maximum iron content of approximately 34% iron of the metal part in the $M_{23}C_6$ type and unknown iron content in the M_7C_3 type. The activation energies calculated from the DTA peak positions suggested that substitutional diffusion of metal atoms is the limiting step for decomposition and also, that nucleation of precursors is involved.

The decomposition was anticipated to be influenced by at least four parameters; thermal history, carbon content, sample geometry and the presence of precursors. The influence of compressive stresses is treated in the next section. In CO carburized samples, the surface area becomes increasingly important as the carbon content increases. But already at low carbon content in 5μm powder the surface area is a dominant factor. At high carbon contents (approx. 3.5wt.%), surface area and consequently, the presence of more nucleation sites, is the most decisive parameter. For low carbon contents (approx. 1.5wt.%) the thermal exposure has little influence. The precipitation temperature determined from DTA experiments experiences a maximum shift for high carbon contents to approximately 950K in CO carburized samples. In C_2H_2 carburized flakes the nucleation of carbide clusters is strongly promoted and thermal exposure has a strong influence on the precipitation temperature, which apparently experiences a maximum shift to

approximately 775K. The low precipitation temperature in C_2H_2 carburized flakes is affected by the larger carbon content (5wt.%), the increased density of surface nucleation sites and the possible presence of carbon clusters already formed during carburization. It was suggested that the enormous carburizing potential and/or the superior surface activation of the C_2H_2 carburizing gas was responsible for nucleation of the carbon clusters during carburization. Conversely, the carburizing potential of a CO carburizing gas is relatively low and the presence of oxygen in the CO molecule may retard the Cr-carbide nucleation due to the high affinity of Cr to O.

5.6 Influence of composition induced stresses

5.6.1 Experimental

Stainless steel AISI 316L powder with a particle size <20μm was used for investigating the stability of expanded austenite. For recrystallization and austenitization the stainless steel powder was heated in pure H_2 to 1353 K at a heating rate of 30 K/min and upon reaching this temperature immediately cooled to the carburizing temperature. As a consequence of the annealing, deformation-induced martensite that had formed during the manufacturing of the powders, transformed into austenite. Furthermore, the heat treatment in pure H_2 leads to an activation of the surface of the particles, by reducing the oxide layer and thus removing the main barrier for carburization in a gaseous atmosphere.

Gaseous carburizing by thermogravimetry

Gaseous carburizing was performed in a Netzsch 449C thermal analyzer, which allows simultaneous thermogravimetric analysis (TGA) and differential thermal analysis (DTA). Gaseous carburizing was performed in CO/H_2 or C_2H_2/H_2 atmospheres. The composition of the carburizing gases was controlled by adjusting the flow rates with Brooks electronic mass flow controllers to: 20mL CO/min, 30mL H_2/min and 5mL N_2/min, and 50mL C_2H_2/min, 50mL H_2/min and 5mL N_2/min. Carburizing was performed at 743 K in $CO/H_2/N_2$ for 4 and 16 hours and at 654 K in $C_2H_2/H_2/N_2$ for 30min. Accordingly, three different samples were made: one sample with an average of y_C=0.056 (denoted as LC for Low Carbon) in solid solution, one sample with an almost uniform composition of y_C=0.15 (denoted as HCu for High Carbon uniform) and one sample with an average y_C=0.138 and a distinguishable case of expanded austenite on a carbon free core (denoted as HCg for High Carbon gradient). After ended carburization the samples were cooled in pure Ar. The carburizing conditions and carbon contents are summarized in Table 5.4. Since the same gas mixture is used for the LC and HCu samples, it can be concluded from a coupling between carburizing time and carbon content, that the carburizing kinetics in the chosen CO/H_2 mixture is predominantly controlled by the rate of the surface reaction.

Sample	Duration (h)	Temperature (K)	y_C	wt.%	at.%	gas
LC	4	743	0.056	1.17	5.3	CO/H_2
HCu	16	743	0.150	3.21	13.1	CO/H_2
HCg	0.3	653	0.138	2.97	12.1	C_2H_2/H_2

Table 5.4: Designation, carburizing time and temperature and carbon content expressed as y_C, wt.% and as at.% C.

Thermal analysis

Isochronal annealing of the expanded austenite containing powders was performed in the Netzsch STA449C thermal analyzer applying a constant heating rate of 20 K/min. Experiments were carried out in a flow of 20 mL/min of Ar. The starting temperature was about 300 K and the final temperature was 1353 K for all isochronal annealing experiments. The typical sample mass used for the decomposition experiments was 100 mg. A reference baseline was recorded

by heating the decomposed sample according to the gas/temperature program of the first run. Hence, instrumental effects could be corrected for.

X-ray diffraction

X-ray diffraction with a Bruker AXS D8 X-ray diffractometer was applied for identification of the as-carburized and the thermally decomposed powders. The instrument used was equipped with a Cr anode and a set of Göbel mirrors in the incident beam. Bragg-Brentano scans were made at a step size of $0.01°2\theta$ and a counting time of 12 seconds per step.

5.6.2 Results and interpretation

Carburized powders

X-ray diffractograms of the as-carburized AISI 316L powders are given in Figure 5.12. A peak shift to lower diffraction angles as compared to uncarburized austenite is observed for all expanded austenite line profiles. This peak shift is a direct consequence of the solid solution of carbon atoms, i.e. the development of γ_C. The higher the carbon content, the larger is the shift to lower Bragg angle. The peak position is also influenced by the occurrence of (large) compressive stresses in some of the samples, which give rise to an hkl-dependent peak shift to lower diffraction angles and possibly to the presence of stacking faults [36].

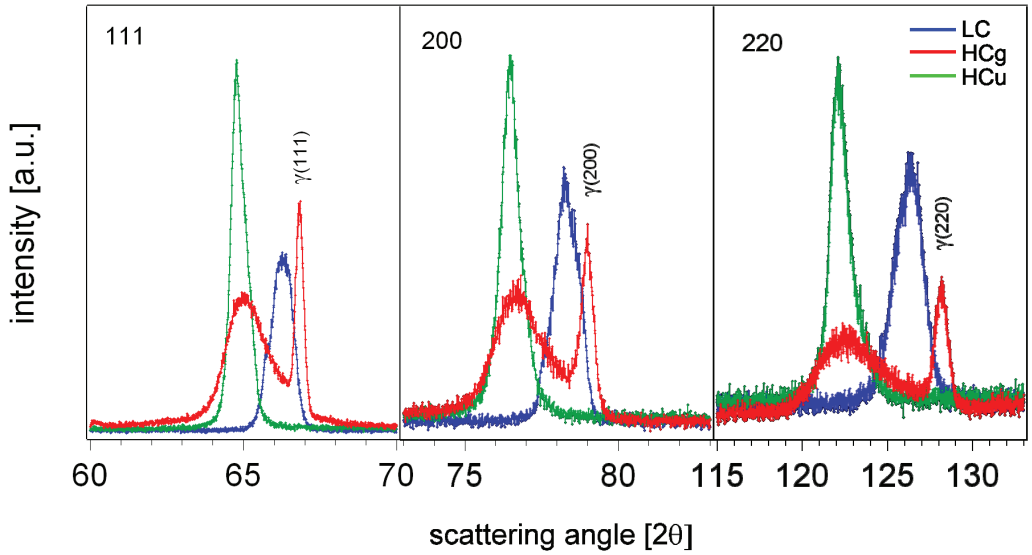

Figure 5.12: X-ray diffraction line profiles of carburized AISI 316L powder. The peak position of uncarburized austenite is indicated as γ(hkl).

The sample denoted as HCg shows X-ray line profiles for (111), (200) and (220) consisting of a narrow peak at relatively high scattering angle and a broad peak at a relatively high scattering angle. These peaks are attributed to the uncarburized austenite core and the expanded austenite case, respectively (cf. Figure 5.13). For the powders denoted as LC and HCu, diffracted intensity from the uncarburized core is absent. For the HCu sample the expanded austenite peak is narrow, indicating a relatively uniform C distribution in the powder and, consequently, only modest compositionally induced stress gradients in the individual grains. For the LC powder single, albeit asymmetrically broadened, line profiles of γ_C are observed, which indicates that the carbon content is not uniform, but the composition range is limited (in particular as compared to the HCg sample).

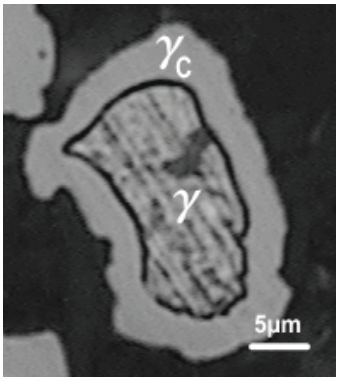

Figure 5.13: Reflected light microscopy image of as-carburized AISI 316L powder HCg with y_C=0.138 (averaged over the entire powder); the carbon-free core (γ) is encased by expanded austenite (γ_C).

Isochronal annealing of expanded austenite

The DTA curves recorded at a heating rate of 25 K/min for the three investigated powders are shown in Figure 5.14. All samples contain an exothermic signal solely related to the phase transformations in the powder. The temperature range wherein the exothermic reactions occur is rather broad and spans from 700 K to 1250 K. The exothermic signals have a main peak defining the temperature at which the maximum rate of transformation occurs in the material. The width of the main DTA-peak is affected by differences in the carbon content due to the powder size distribution: small particles are expected to have higher averaged carbon content than small particles. In the LC powder the decomposition of expanded austenite initiates at 700K and has a maximum at 1150K. For the sample obtained on prolonged carburization (HCu) two partly overlapping peaks occur in the temperature range 900-1100 K. In the HCg sample the decomposition is initiated at 950 K and has a maximum around 1100 K.

X-ray diffraction results of decomposed AISI 316L are given in Figure 5.15. The decomposed powders investigated with Xray diffraction had been heated twice to 1353 K, once for the actual decomposition and once to acquire the baseline. Generally, decomposed AISI 316L powders consist of carbides and austenite; expanded austenite is no longer present (compare to Figure 5.12). The X-ray diffractograms of decomposed LC sample indicates the presence of carbide of type $M_{23}C_6$ and a small amount of M_7C_3 type. In the two HC samples the only carbide present is of M_7C_3 type. As compared to the indicated peak positions for $M_{23}C_6$ and M_7C_3, the experimental Bragg peaks are shifted to higher scattering angles. This is ascribed to the presence of iron in the carbides (see Section 5.3.3). The presence of Hagg carbide, which was reported to occur on prolonged annealing [38], could not be confirmed by X-ray diffraction in our samples.

As previously shown in Section 5.3.3, equilibrium calculations for carburized samples with three carbon contents predicted the preferred decomposition products as a function of carbon content and temperature. Clearly, in the LC powder predominant precipitation of $M_{23}C_6$ can be expected during the DTA investigation (Section 5.3.3, Figure 5.5a). The content of M_7C_3 in these samples should be limited and its development could have occurred in regions with higher C content than average at the highest temperature reached, in accordance with the results given in Figure 5.15. For the HCu sample both $M_{23}C_6$ and M_7C_3 can develop at low temperatures up to approximately 1050 K. Beyond this temperature $M_{23}C_6$ is expected to be converted to M_7C_3. It is tempting to attribute the exothermal heat effect at about 1050 K in Figure 5.14 to this conversion of $M_{23}C_6$ developed at lower temperature. Then, the exothermic reaction at lower temperature for the HCu sample should be attributed to the simultaneous development of $M_{23}C_6$ and M_7C_3. This interpretation is consistent with dominance of M_7C_3 in the diffractogram for the decomposed HCu sample (Figure 5.15).

The exothermic reactions in the HCg sample are postponed to higher temperature as compared to those in the HCu sample. An obvious explanation for this observation would be that the driving force for decomposition of expanded austenite and associated carbide formation in-

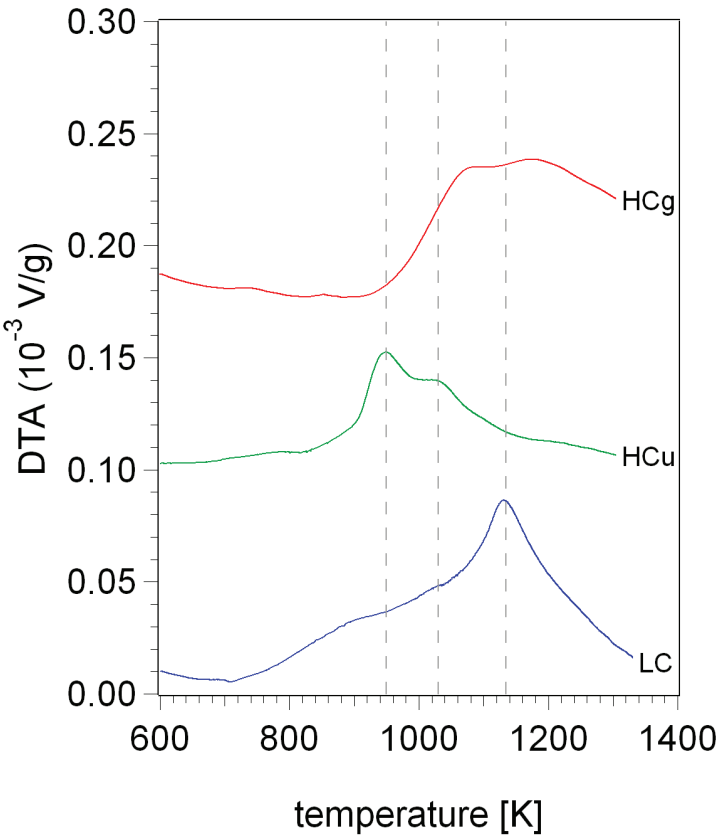

Figure 5.14: DTA experiments on AISI 316L 20μm powders with high carbon, with (HCg) and without (HCu) composition gradient, and with low carbon (LC). DTA curves correspond to a heating rate of 25K/min. The vertical lines mark the locations of peaks the DTA signals of in the LC and HCu samples.

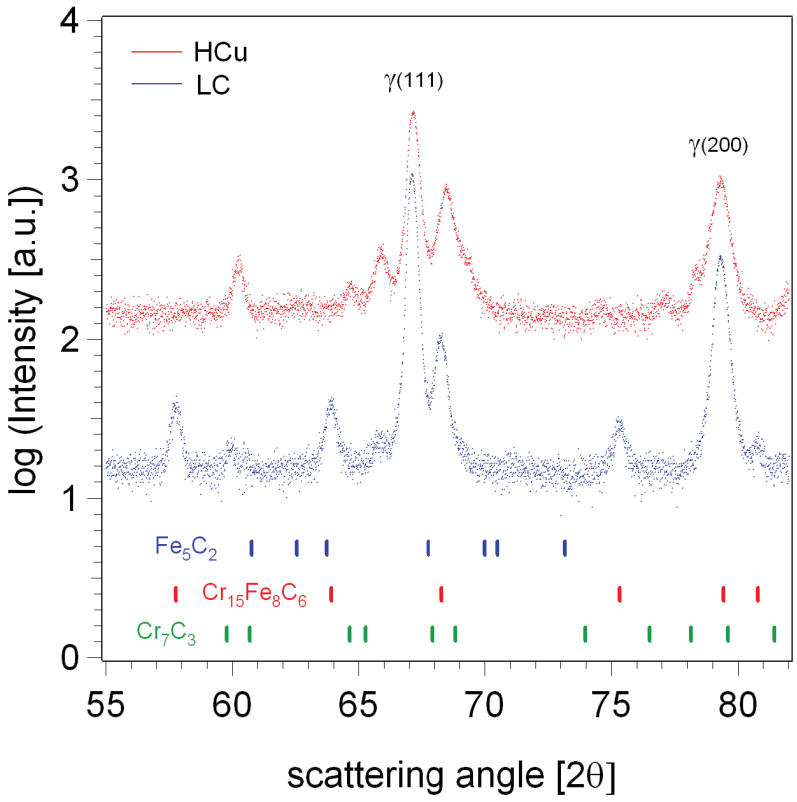

Figure 5.15: X-ray diffractograms of decomposed expanded austenite 20μm powder. The peak position of uncarburized austenite is indicated as γ(hkl).

creases with carbon content. Nevertheless, then decomposition would be expected to start at about the same, or even lower, temperature as in the uniform samples, i.e. about 800 K, because the highest C contents in HCg should be higher than in HCu as to reach the high average C content in HCg. Also, it would be expected that the DTA signal for HCg broadens towards the temperature region where the LC sample decomposes, because the lower C contents in the HCg sample are of comparable magnitude (cf. Figure 5.12). Clearly, decomposition is postponed until reaching about 950 K, where the HCu sample has its maximum heat effect. This difference in starting temperature of the transformation could have its origin in the presence of compressive residual stresses in the HCg powder or a consequence of the shorter thermal exposure as reflected by the short carburizing time (Table 5.4).

5.6.3 Discussion

As to predict the qualitative effect of a state of compressive stress in expanded austenite on carbide formation, the volume changes occurring during transformation were calculated. In the calculations it was presumed that carbon expanded austenite with different carbon contents is transformed into the carbides $Cr_{23}C_6$ or Cr_7C_3 and carbon-free austenite. The presence of Fe in the carbides was omitted in the calculations, which has as a consequence that the specific volume of the carbides is overestimated. Assuming that only the Cr originally present in the alloy transforms into $Cr_{23}C_6$ (and carbon-free austenite), the equivalent carbon content that can be accommodated as $Cr_{23}C_6$ corresponds to y_C=0.0496, which is smaller than the carbon content in LC (Table 5.4). Incorporating Fe in $Cr_{23}C_6$ up to 30% (see Figure 5.5a), the maximum carbon content that can be accommodated as $M_{23}C_6$ carbide corresponds to y_C=0.076, which is higher than the carbon content in the LC powder (Table 5.4) and thus consistent with predominant $M_{23}C_6$ in the LC sample. Similarly, if all Cr precipitates as Cr_7C_3 the equivalent carbon content amounts to γ_C=0.081, which is significantly smaller than the carbon content in the HCu powder. Incorporating Fe in Cr_7C_3 up to 50% (see Figure 5.5c) the equivalent carbon content is y_C=0.18, which is beyond the solubility of carbon in expanded austenite in HCu, i.e. yc=0.15 (Table 5.4). Seen in the light of the above discussion the calculations below should be considered approximate.

The volume change associated with the transformation of expanded austenite was calculated as a function of the carbon content released from expanded austenite and precipitated as carbide of type Cr_xC_y. These calculations for two initial carbon contents y_C=0.056 and y_C=0.15, reflecting the contents in samples LC and HCu (cf. Table 5.4). The lattice parameter of expanded austenite was taken as [see Chapter 3 of this thesis]:

$$a = 0.3596 + 0.0603 y_c (nm), \tag{5.1}$$

Data used for the carbides are listed in Table 5.5.

Compound	Crystal structure	Vol./ unit cell ($10^{-30} m^3$)	C atoms/unit cell
$Cr_{23}C_6$	$D8_4{}^2$	1191.016	24
Cr_7C_3	P31C	765.55	24

Table 5.5: Crystallographic data used for the calculation of volume changes upon carbide formation from expanded austenite [3].

The volume changes calculated are given in Figure 5.16. Apparently, the volume reduction associated with the development of $Cr_{23}C_6$ is largest for lower C content; for higher C contents the volume reduction is largest upon precipitation of Cr_7C_3. The carbon content where equal volume reductions were found for both carbides depends on the initial carbon content in expanded austenite.

Qualitatively, the calculated volume reductions during carbide precipitation would be favoured by the presence of compressive stresses. This result of the calculations is opposite to the observation of postponed decomposition of the gradient sample. It would be expected that the presence of a compressive residual stress gradient in sample HCg would promote the precipitation of carbides. Evidently, this effect is obscured by other effects as could be introduced on

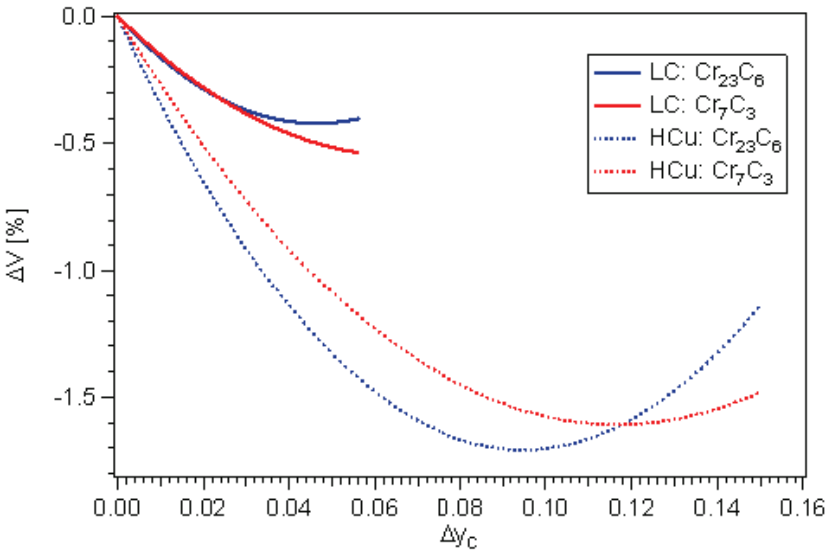

Figure 5.16: Relative volume change, δV, associated with the precipitation of an amount of carbon from expanded austenite, δy_C, as carbide Cr_xC_y. The maximum amount δy_C that can precipitate from LC and HCu is 0.056 and 0.150, respectively (cf. Table 5.4).

sample preparation. The most obvious would be the thermal exposure. It is therefore anticipated that the relatively long carburizing time of the HCu samples (16 h) has lead to precursors, as for example C clusters, that affect the subsequent carbide precipitation as observed on the DTA investigations.

5.6.4 Conclusion

The hypothesis that compositionally induced stresses affect the decomposition kinetics of carbon expanded austenite was tested. Volume changes associated with the formation of carbides and austenite from expanded austenite could not solely explain the observed influence on carbide precipitation. On the other hand, thermal exposure prior to decomposition is anticipated to be more important than stress.

6 Systematic study of metal dusting corrosion

In this chapter, a systematic study of AISI 316 stainless steel foils exposed to a mixture of C_2H_2 and H_2 at 823K (550°C) is described. The applied metal dusting conditions result in dissolution of carbon atoms in the surface region by carburization and the formation of carbon expanded austenite, γ_C. Surface nucleation of $M_{23}C_6$ occurs on prolonged exposure, designated as *stage I*. This first stage of carbide development is followed by a simultaneous transformation of the $M_{23}C_6$ carbides and the supersaturated alloy, into a carbide network with a two-phase/lamellar morphology, designated as *stage II*. Transmission electron microscopy revealed that the lamellar structure consists of $M_{23}C_6$ and austenite. Eventually, the foils are converted into metal dust accompanied by a thinning and disappearance of the foils.

6.1 Introduction

Fe-based (steel) and Ni-based high chromium alloys are widely applied as high temperature materials in the petrochemical industry. All Fe-based and Ni-based metals in high temperature processes that are exposed to carbon-bearing gases, like syngas, in the temperature range 723K-1123K are subjected to carburization, i.e. dissolution of carbon in the alloy and the development of carbides. Generally, such carburization may lead to an aggressive corrosion phenomenon known as metal dusting (MD) or catastrophic carburizing [5, 32]. The metal dusting corrosion manifests itself as a mixture of fine carbides, metal particles and carbon dust (including carbon filaments). It is macroscopically observed as pitting or general metal wastage. Incubation time may vary from hours to years and has greatly complicated, and has as yet, hindered an systematic investigation of the parameters influencing the kinetics of the catastrophic carburizing process on commercially applied materials. In this study, an unorthodox approach for the investigation of metal dusting is followed. A recently patented method [40] developed for surface hardening of stainless steels is applied to "by-pass" the incubation time. The advantage of this method is that the passive oxide film covering the stainless steel surface is removed instantaneously during the gaseous treatment. Consequently, the kinetics of pit initiation and carburizing kinetics are separated and can be studied individually. Another advantage is the non-stochastic attack, which practically means that the entire surface acts as a pit, thereby dramatically facilitating microstructure investigations. The reducing atmosphere further simplifies matters, in that the competition between metal dusting and oxidation which introduce complicating kinetics is avoided. However, it is realized that in addition to its role in forming protective oxide scales, oxygen may play an active role in the metal dusting mechanism. This subject will be treated in the next chapter.

6.2 Experimental

6.2.1 Gaseous carburizing by thermogravimetry

Gaseous carburizing of 100μm foils was performed in a Netzsch 449C simultaneous thermal analyzer, which allows thermogravimetric analysis (TGA). For recrystallization and austenization,

foils were heated to 1353K at a heating rate of 30 K/min and upon reaching this temperature immediately cooled in pure H_2. During austenitization deformation-induced martensite formed during manufacturing of the foil was completely transformed to austenite. Gaseous carburizing was performed in atmospheres of acetylene, hydrogen and nitrogen. The flows were adjusted by Brooks electronic mass flow controllers to: 2mL, 5mL or 50mL C_2H_2/min, 50mL H_2/min and 5mL N_2/min. The carburization was performed at 823K. Heating to carburizing temperature was performed at a rate of 30K/min in the carburizing atmosphere.

6.2.2 Scanning electron microscopy

Scanning electron microcopy (SEM) was carried out at Haldor Topsøe A/S with a FEI XL30 instrument, equipped with a field emission gun. The instrument incorporates Energy Dispersive X-ray Spectrometry (EDS) for compositional analysis.

6.2.3 Focused ion beam lift-out

Preparation of samples for transmission electron microscopy was done by focused ion beam (FIB) lift-out. The lift-out was carried out at Center for Electron Nanoscopy at DTU (CEN), with a Quanta 200 3D FIB SEM Dual Beam instrument.

6.2.4 Transmission electron microscopy

For transmission electron microscopy (TEM), a Jeol 3000, located at Materials Research Division, Risø National Laboratory for Sustainable Energy, was applied. The instrument incorporates Energy Dispersive X-ray Spectrometry (EDS) for compositional analysis.

6.2.5 X-ray diffraction

X-ray diffraction (XRD) was applied for the identification of the as-prepared and carburized material. The applied instrument was a Bruker AXS (Bruker AXS GmbH, Germany) D8 X-ray diffractometer, equipped with a Cr anode and a set of Göbel mirrors in the incident beam. The carburized foils were mounted on carbon tape and placed in the instrument.

6.3 Results and interpretation

6.3.1 Metal dusting sequence

In Figure 6.1, reflected light micrographs of 100μm stainless steel foils exposed to metal dusting conditions for various durations are presented. The carburizing time ranges from 2 hours to 337 hours. The sequence of the cross sectional images ranges from the beneficial state of carbon expanded austenite in the surface region in Figure 6.1a and b, through the sporadic precipitation of carbides in the outer surface first identified in Figure 6.1c after 48 hours, eventually to the disappearance of the foil by metal dusting after 337 hours (Figure 6.1p). The precipitation of carbides in the outer surface, develops through the sequence to a continuous and compact carbide layer. The carbide layer front meets from both sides of the foil after 141 hours (Figure 6.1m) whereafter a clear thinning and disappearance of the foil is observed. The thinning of the foil is accompanied by heavy dust formation as in particular observed after 337 hours in Figure 6.1o and p marked by the white arrows. The precipitation of carbides along grain boundaries becomes evident as the centre of the foil is increasingly affected by the etching agent. The sequence of micrographs shows clearly that carbide formation occurs heterogeneously at the surface and along grain boundaries. Grain boundary development of carbides occurs later than surface nucleation. After 48h (Figure 6.1c) grain boundaries are only faintly visible. The distinct delay of the appearance of carbides along the grain boundaries can be explained from the first appearance of γ_C at the surface and the higher content of carbon close to the surface. Furthermore, volume effects associated with the γ_C to carbide conversion are easier accommodated close to the surface than along grain boundaries in the bulk.

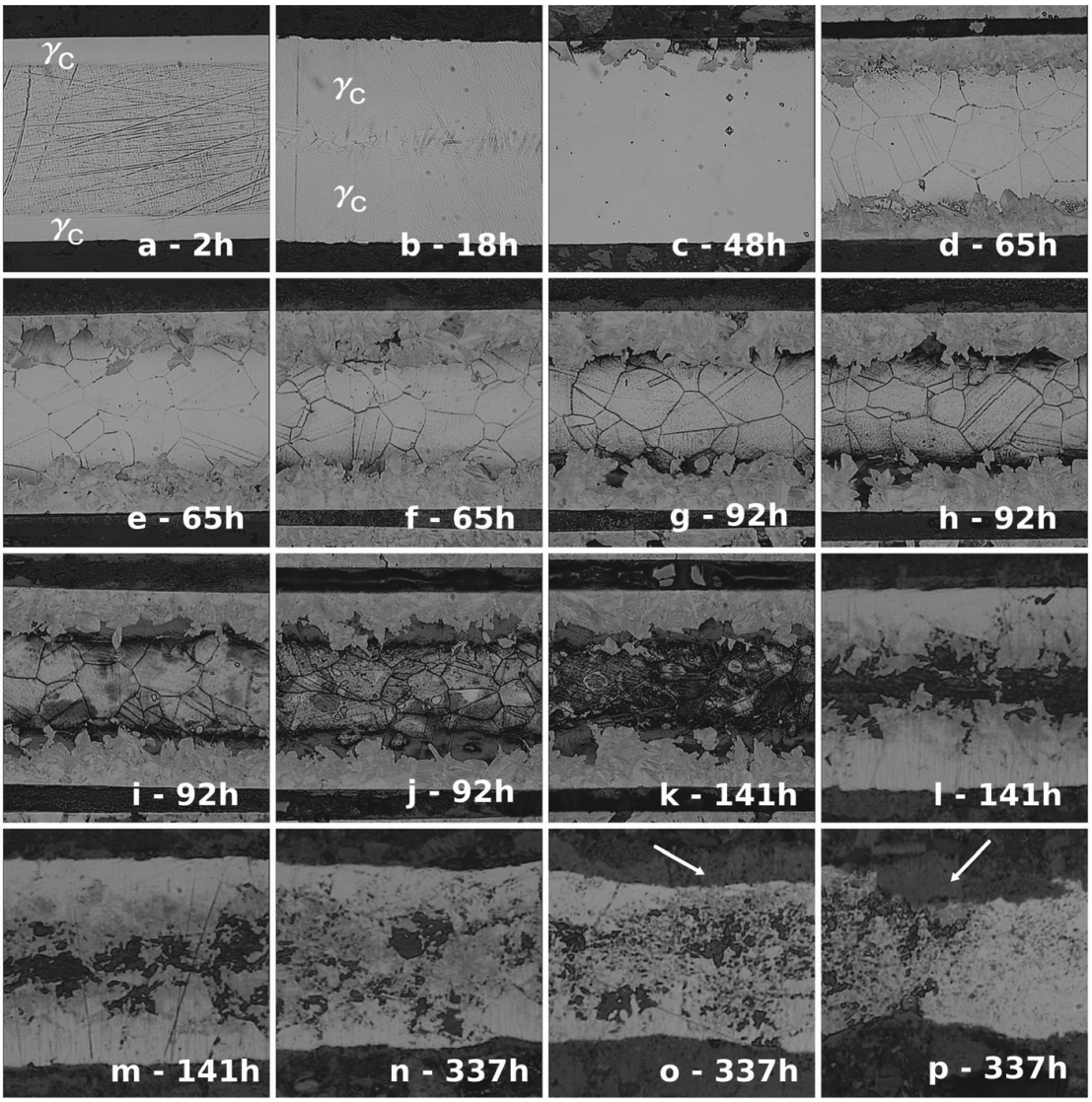

Figure 6.1: Light optical micrographs of metal dusting sequence on AISI 316 100μm foils. Exposure is from 2h to 337h at 823K in a gas mixture of C_2H_2(5mL/min)+H_2(50mL/min). Metal dust is marked with white arrows (o, p).

6.3.2 X-ray diffraction

X-ray diffraction was applied to determine the phases developing in the near surface zone as a consequence of carburization (Figure 6.2). The diffractogram collected after 2 hours of exposure shows the presence of carbon expanded austenite by a shift of the austenite peaks to lower diffraction angles. The right shoulder of the $\gamma_C(111)$ reflection indicates a carbon gradient with the largest carbon content near the surface. Only a weak signal from the underlying austenite ($\gamma(111)$) is visible. This is due to an information depth not surpassing the depth of the carbon expanded zone of 12μm. Based on the established relation between lattice parameter and carbon content [see Chapter 3], the maximal carbon content in the carburized zone is estimated as approximately 2.5wt.% after 2 hours. After 18 hours, $M_{23}C_6$ precipitates become visible by X-ray diffraction. At 48 hours the $M_{23}C_6$ precipitates have grown in size and become visible by reflected light microscopy in the outer surface, as seen in Figure 6.1c. The X-ray diffractograms indicate the decomposition of carbon expanded austenite (a shift to higher diffraction angles) with the simultaneous appearance of $M_{23}C_6$ reflections. The presence of the $\gamma(111)$ and $\gamma_C(111)$ as well as $\gamma(200)$ and $\gamma_C(200)$ peaks reflects that areas are present in which no carbon expanded austenite remains and areas in which the carbon expanded austenite is only partly decomposed. Upon prolonged exposure from 48 hours to 337 hours, decomposition proceeds and the end product in the surface and subsurface region is carbide of the form $M_{23}C_6$ and austenite. Notice that the information depth only allows identification of carbides in the surface and subsurface regions. In the sequence the surface nucleation of $M_{23}C_6$ will be referred to as *stage I*. A few metal dusting experiments on an AISI 316 bulk samples were carried out under similar conditions as for the just described 100μm foils. The objective was to verify that the observed surface phenomena were not restricted to foils, but also occurred on bulk samples. From Figure 6.3 it is evident that the development of carbides at the surface as well as γ_C also occur after prolonged carburization of bulk samples. Thus the sample geometry is assumed to alter the mechanism only marginally.

6.3.3 Thermogravimetry

Additional information is revealed by inspection of the mass-gain curve collected during the metal dusting experiment with a duration of 337 hours (Figure 6.4). Three distinct events in the mass-gain curve are observed. After approximately 20 hours a steep rise in uptake occurs. The increase in mass gain cannot be related to surface depositions since no such were observed. On the other hand, the increase in mass gain may be associated to the simultaneous appearance of $M_{23}C_6$ as evident from the X-ray diffractogram collected after 18 hours (cf. Figure 6.2). It is, however, unclear why the precipitation of $M_{23}C_6$ gives rise to an increased solubility of carbon in austenite and/or carbides. The second distinct event occurs after approximately 50 hours, where a decrease in the uptake rate is observed. This observation is consistent with the formation of a massive $M_{23}C_6$ layer in the surface (cf. Figure 6.1c and d). It is anticipated that formation of the massive $M_{23}C_6$ layer slow down the carbon ingress. After approximately 220 hours, an increase in uptake occurs again. The increase in mass is inconsistent with the apparent material loss and thinning of the foil (Figure 6.1o and p). However, it cannot be excluded that the observed mass-gain is attributed to the heavy graphite deposition (arrows in Figure 6.1o,p) and that an actual mass loss would be observed for longer periods.

6.3.4 Scanning electron microscopy

Scanning electron microscopy was applied to obtain higher resolution imaging of the foils in the metal dusting sequence. EDS-analysis was employed to qualitatively outline the different morphologies and their composition. Examination of the SEM micrographs shows that the surface and subsurface consists of a complicated network of carbides. Four regions are identified which differ significantly in microstructure (Figure 6.5). With a view to establish the order of appearance of the different identified morphologies, all foils in the sequence were analysed by means of scanning electron microscopy; occasionally microhardness values were used as supplement.

Microhardness indents obtained in the near-surface zone, just after the initial development of carbides of the form $M_{23}C_6$ (*stage I*), are depicted in Figure 6.6. Approaching the surface of

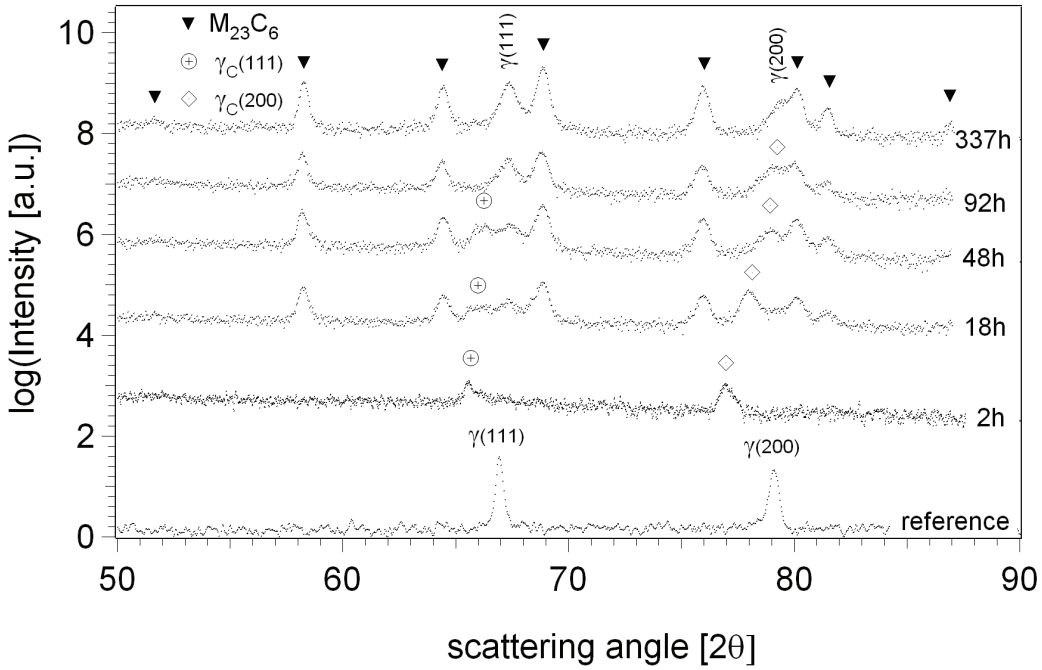

Figure 6.2: X-ray diffraction analysis of selected foils in the metal dusting sequence on AISI 316 100μm foils. Exposure is from 2 hours to 337 hours at 823K. The diffractograms of the carburized samples are shifted to higher angles as compared to the reference diffractogram (approximately $2theta$=2° for $\gamma_C(111)$) due to a misalignment of the sample height during these particular measurements.

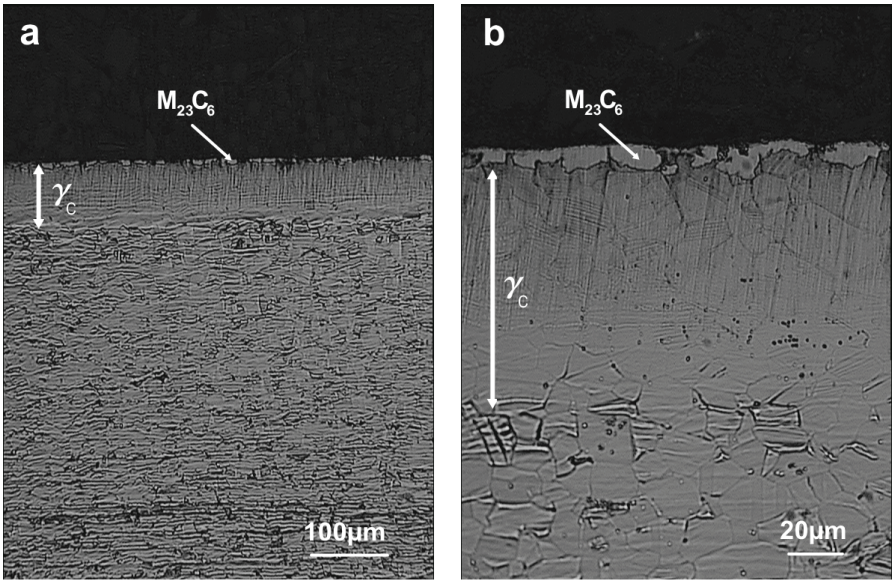

Figure 6.3: Light optical micrographs of AISI 316 bulk specimens exposed to metal dusting conditions at 823K for 18 hours. (a) low magnification, (b) higher magnification. The carbon expanded zone (γ_C) of approximately 70μm thickness and the surface nucleations of $M_{23}C_6$ (*stage I*) are indicated in the figure.

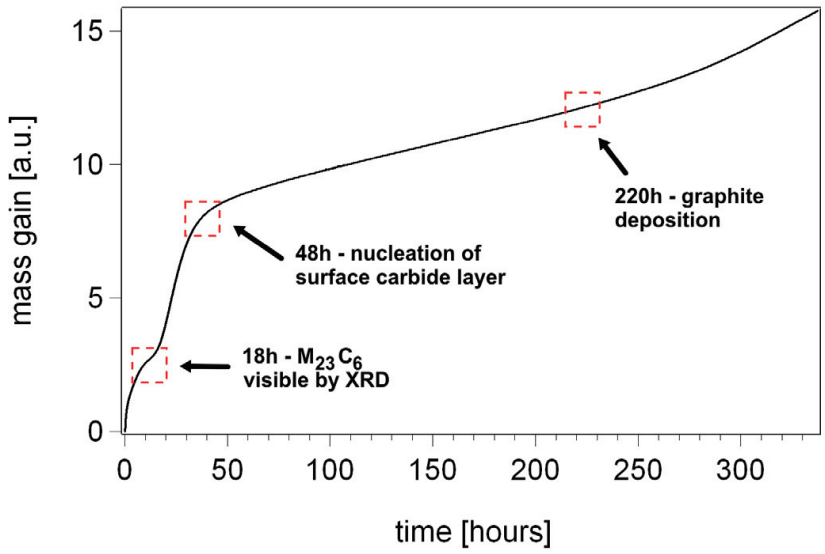

Figure 6.4: Thermogravimetric mass-gain curve collected during carburization of stainless steel 100μm foils in a gas mixture of C_2H_2 and H_2 at 823K. Three distinct events are indicated in the figure.

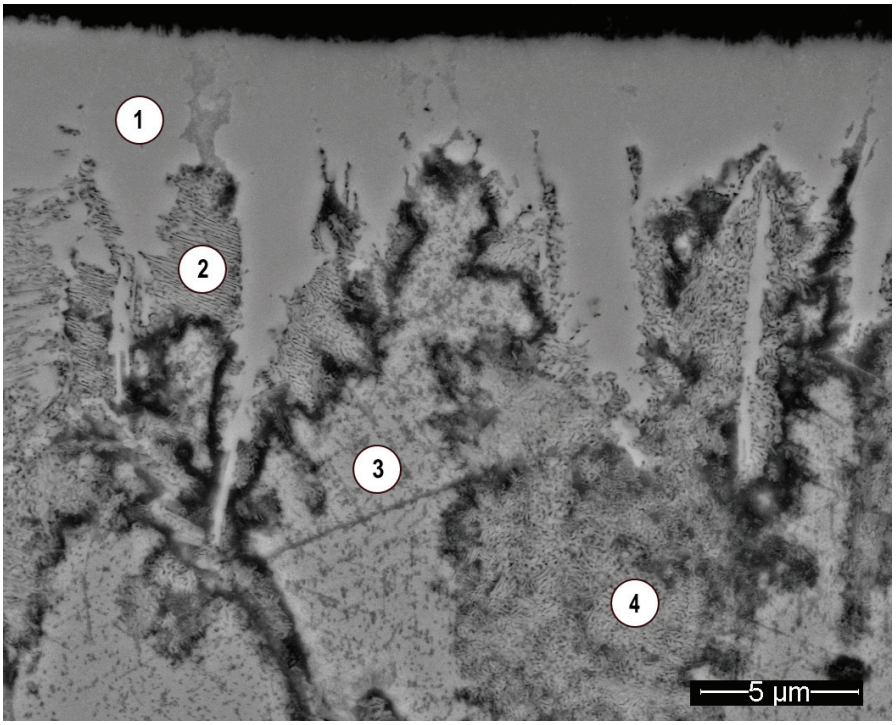

Figure 6.5: Back scattered electron image of different carbide morphologies in the near-surface region on AISI 316 100μm foil exposed for 92 hours at 823K. 1) the $M_{23}C_6$ carbide layer formed in *stage I*. 2) a two-phase morphology/carbide network, 3) Carbon expanded austenite, maybe with tiny carbides, 4) another morphology of the carbide network.

the foil, the first four microhardness indents are similar in size indicating no steep carbon concentration gradient. The microhardness indent number five, corresponding to the area marked 2 in Figure 6.5, shows a significantly decreased hardness. It is anticipated that the decreased hardness is a consequence of the decomposition of the carbon expanded austenite. The microhardness indent number 6 in Figure 6.6 obtained in the $M_{23}C_6$ layer measures approximately 2000HV5. The high hardness evidence that carbides are indeed present.

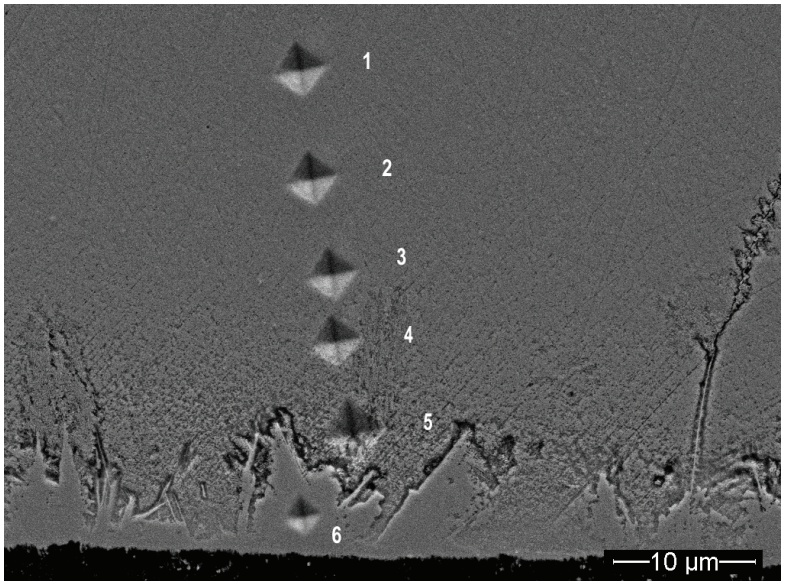

Figure 6.6: Secondary electron image of the surface of the carbon supersaturated AISI 316 foil exposed for 48 hours at 823K. The hardness indents were measured with microhardness equipment.

The $M_{23}C_6$ layer formed during *stage I* is rather featureless. Indications of a two-phase morphology, presumably originating from the $M_{23}C_6$ layer, are observed in Figure 6.7a and designated *carbide network*. The transformation of the $M_{23}C_6$ layer into a carbide network progresses with thermal exposure and eventually leads to the total transformation and disappearance of the $M_{23}C_6$ layer. The transformation step will be referred to as *stage II*. Figure 6.7b illustrates surface areas where the $M_{23}C_6$ layer is entirely replaced by the carbide network.

Nucleation of $M_{23}C_6$ in *stage I* is not restricted to the outermost surface alone, also in the grain boundaries $M_{23}C_6$ are formed (Figure 6.8a). Simultaneously with the transformation of $M_{23}C_6$ into the carbide network in the surface region and in grain boundaries, transformation of the expanded austenite occurs. The expanded austenite is directly transformed into the carbide network along the interface marked with the dotted line in Figure 6.8b. The interface between the carbide network and the expanded austenite has a fern-like structure and will be the subject for further TEM investigation treated in the following section.

6.3.5 Transmission electron microscopy

A TEM sample was prepared by focused ion beam (FIB) milling on a AISI 316 100 μ foil exposed for 48 hours at 823K. The selected area to be lifted out is depicted in Figure 6.9a. The objective of the TEM study is to investigate the interface between the expanded austenite and the fern-structured front (Figure 6.9b)

TEM analyses of the interface/lamellar structure are presented In Figure 6.10. The bright field image (Figure 6.10a) shows the lamellar morphology in the decomposed/transformed region from were the selected area diffraction pattern (Figure 6.10b) is obtained. Generally, two series of spots are observed as marked ′A′ and ′B′ (Figure 6.10b). From electron diffraction patterns obtained for three tilt angles in the decomposed region, it was confirmed that the phase corresponding to the spots marked ′A′ is $M_{23}C_6$ and the phase giving rise to the series of diffraction

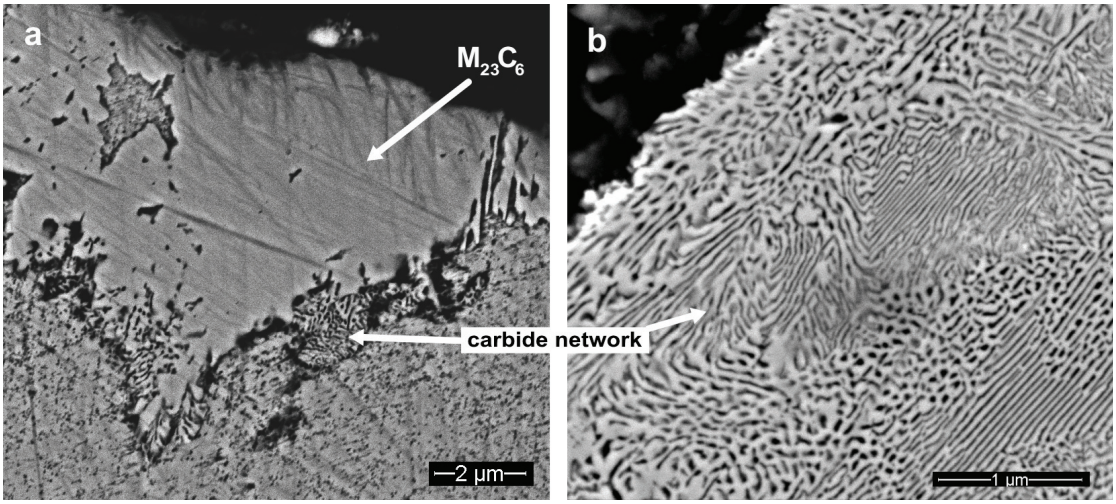

Figure 6.7: (a) Back scattered electron image of the carbide network originating from the $M_{23}C_6$ layer. (b) Secondary electron image of the former $M_{23}C_6$ layer in the outermost surface region, which eventually is entirely transformed into a carbide network.

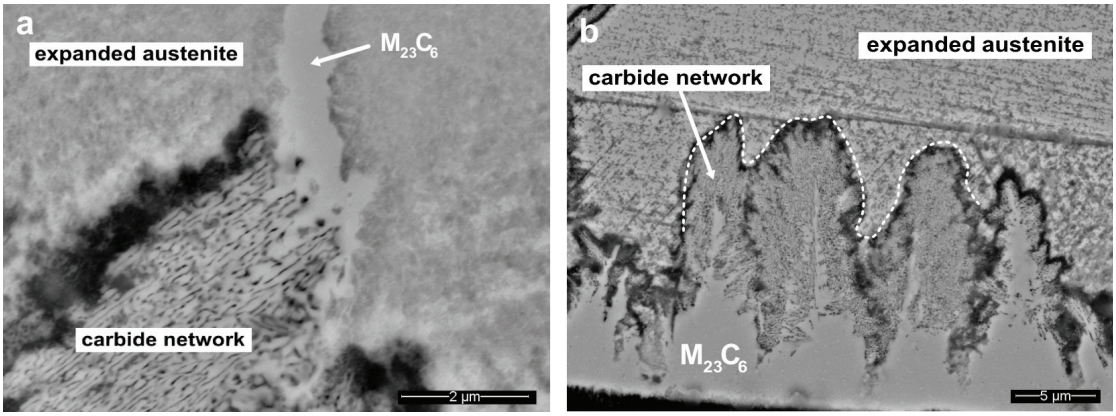

Figure 6.8: (a) backscattered electron image of the transformation of the $M_{23}C_6$ preferably formed in the outermost surface region and in grain boundaries into a carbide network. (b) backscattered electron image of the fern-like front (dotted line) in which expanded austenite is transformed into the carbide network.

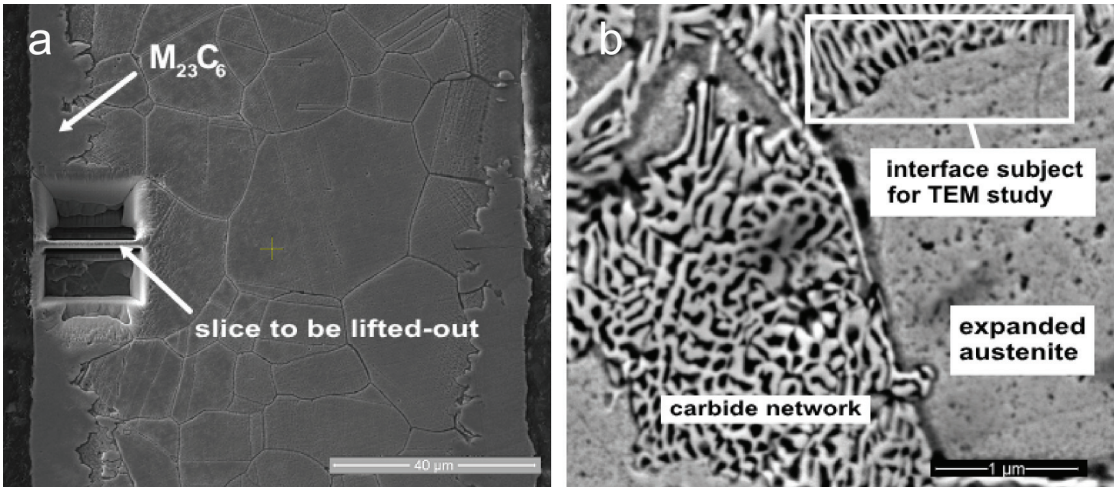

Figure 6.9: (a) secondary image of the TEM sample before lift out of an AISI 316 100μm foil exposed for 48 hours at 823K. (b) secondary electron image of the lamellar-type of interface (marked in the figure) investigated with TEM.

spots marked ′B′, is carbon free austenite.

Diffraction analysis on the austenite (marked expanded austenite in Figure 6.10a), shows a linear expansion of the lattice of 2.8% as compared to pure austenite which corresponds to a carbon content of approximately 3.5wt.%. It was previously shown (Chapter 3) that precipitation of chromium carbides is unavoidable for carbon contents above approximately 3.5wt.% at 693K. Therefore it is probable that carbides are present in the expanded austenite zone, considering the increased thermal exposure in this case. The estimated value of the carbon content is in contradiction to the predicted stable carbide at this carbon concentration (see Thermocalc in Chapter 5.3.3). From Thermocalc calculations the preferred carbide is of type M_7C_3. However, if Fe is incorporated in the carbide and the estimated lattice expansion is slightly overestimated, it is reasonable to expect the presence of $M_{23}C_6$.

Dark field imaging of $M_{23}C_6$ (spot ′A′ in Figure 6.10b) is presented in Figure 6.10d. It is observed that the bright areas in the dark field image coincide with the bright areas of the lamella structure observed in the bright field image. The anticipated presence of carbides in the expanded austenite is not observed by dark field imaging, accordingly they are presumed to be coherent and small. Furthermore, dark field imaging of carbon free austenite (spot ′B′ in Figure 6.10b), presented in Figure 6.10c, shows that the bright areas in the dark field image coincide with the dark areas of the lamella structure observed in the bright field image. This indicates a decomposition of the expanded austenite into carbide and carbon free austenite with a lamellar morphology.

It was further observed that for all three tilt angles, an orientation relationship existed; the determined zone axis for $M_{23}C_6$ and austenite in the lamella structure is identical. However there does not appear to be an orientation relation between expanded austenite in the grain into which the lamellar structure grows and the carbon free austenite in the lamellae. This is further emphasized in Figure 6.11 in which a dark field image of expanded austenite is depicted. The only austenite phase present in the lamellae which has a similar orientation as the expanded austenite is small areas of retained expanded austenite, marked with arrows in Figure 6.11.

6.3.6 Energy dispersive X-ray spectrometry

EDS analysis was carried out in selected points on the lamella structure as depicted in Figure 6.12. The result is shown in Table 6.1. EDS shows that the carbide regions are enriched in Cr and Mo as compared to γ_C, while the austenite regions are enriched in Fe and Ni. The main redistribution of alloying elements over $M_{23}C_6$ and austenite applies for Ni and Cr. The rate-determining step

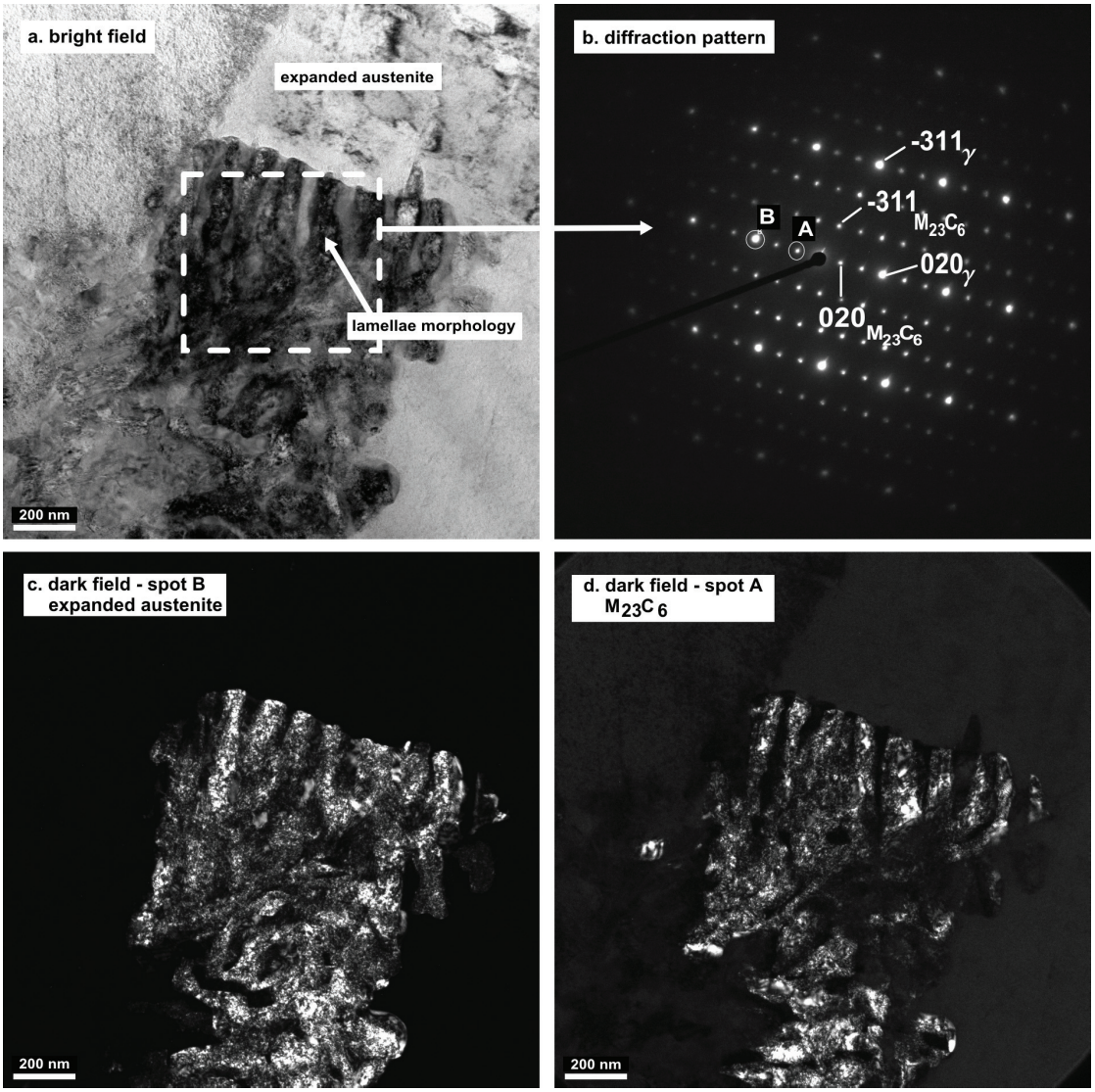

Figure 6.10: (a)conventional TEM bright field image, (b) selected area diffraction pattern marked with spot ′A′ and ′B′, and (c) and (d) the associated dark field images of the lamellar transformation front and the interface to the saturated alloy of an AISI 316 100μm foil exposed to metal dusting conditions for 48 hours. The diffraction pattern constitutes a superposition of a [103] zone axis pattern of $M_{23}C_6$ and a [103] zone axis pattern of γ.

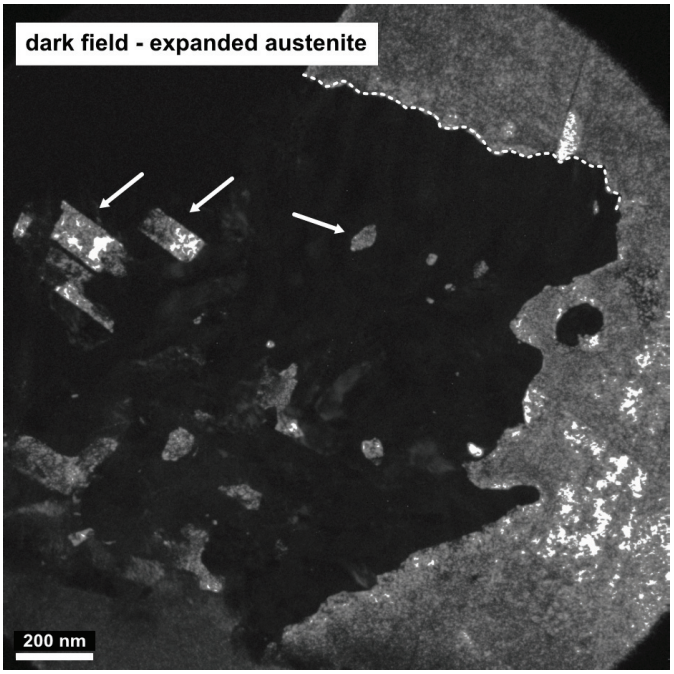

Figure 6.11: TEM dark field image of expanded austenite (bright areas). The interface between the lamella structure and the expanded austenite is indicated with the dotted line. Areas of retained expanded austenite in the lamellar zone with the original orientation are marked with arrows.

in the decomposition is most likely the partitioning of Ni and Cr atoms. The carbon atoms partition relatively fast and will mainly follow Cr and Mo.

Analysis point	Cr	Mn	Fe	Ni	Mo
1	31.77	2.09	56.47	5.01	4.66
2	12.13	1.59	66.46	17.74	2.07
3	24.15	1.82	60.70	9.70	3.63
4	7.37	1.60	69.43	20.25	1.35
5	26.37	1.98	59.31	8.61	3.74
6	11.78	1.67	67.10	17.87	1.57
7	33.54	1.78	55.53	3.97	5.18
8	19.54	1.82	62.50	12.91	3.22

Table 6.1: EDS analyses (wt.%) of the lamellae structure in the sample carburized for 48 hours at 823K.

6.4 Discussion

A lamellar morphology was also found in [61] in which Hagg carbide was embedded between austenite. It was shown that precipitation of Hagg carbide only occurs when a favorable coherent orientation relationship between the austenite and the Hagg carbide is obtained. Nucleation of Hagg carbide requires Ni to diffuse out of the corresponding regions and Fe and Cr to diffuse in. The observed orientation relationship between $M_{23}C_6$ and austenite in the decomposed region in the present work is trivial as compared to the orientation relation found in [61]. This means that an energitic favorable interface between $M_{23}C_6$ and austenite is more easily achieved. This can explain why Hagg carbide is not found in the present work.

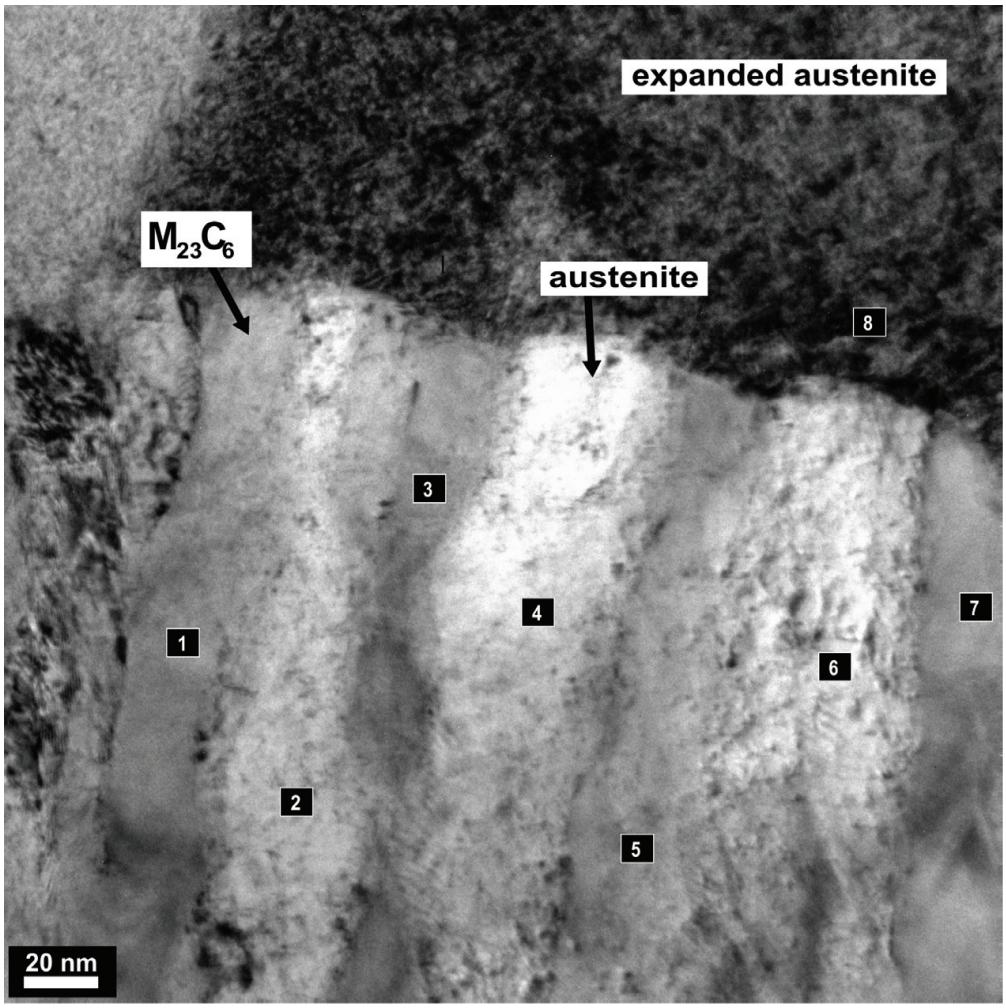

Figure 6.12: TEM bright field image of the lamella structure on the AISI 316 100μm foil exposed for 48 hours at 823K. EDS analysis points are marked in the image.

There appears to be no orientation relation between γ in the decomposed/lamellar region and γ_C. This may indicate that the lamellar structure is developed by decomposition of $M_{23}C_6$ rather than by decomposition of γ_C. This is in accordance with the hypothesis that the featureless $M_{23}C_6$ layer developed in the surface and in grain boundaries during *stage I* precedes the transformation into the lamellar morphology in *stage II*.

The observation of an axial orientation relation between $M_{23}C_6$ and austenite in the decomposed/lamellar region without a sharp interface (cf. Figure 6.12) suggests that a more or less diffuse interface exists between these phases. This would imply that the superlattice reflections as compared to f.c.c. are a consequence of ordering of carbon atoms. It is tempting to ascribe this to spinodal decomposition in $M_{23}C_6$, rather than discontinuous precipitation in γ_C. This would be reconcilable with the absence of a crystallographic orientation relationship between γ_C and γ.

6.5 Conclusion

From the analysis, several stages in the initiation of metal dusting in an environment of C_2H_2 and H_2 at 823K were remarked. The observations can be summarized in a proposed metal dusting mechanism in a reducing environment of C_2H_2/H_2 at 823K:

1. The protective oxide scale fails at some weak point in the surface.
2. Formation of carbon expanded austenite by dissolution of carbon in the metal phase.
3. Decomposition of carbon expanded austenite and precipitation of tiny $M_{23}C_6$ carbides and subsequent massive precipitates along the surface and in grain boundaries, designated as *stage I*.
4. Decomposition of $M_{23}C_6$ into a lamellar morphology by spinodal decomposition in $M_{23}C_6$, designated *stage II*.

Further studies are needed to characterize the subsequent stage(s). A possible route could be by disintegration of the austenite part of the lamellar morphology by graphite formation into small austenitic metal dust particles (Type II mechanism).

7

On the mutual influence of oxygen and carbon on metal dusting corrosion

In this chapter, AISI 316 bulk specimens are exposed to oxidation in a high steam environment composed of Ar-46% H_2O(g) prior and subsequently to metal dusting conditions. Internal oxidation results in a metallic nano network with a presumed catalytic effect on the decomposition of the carburizing gases. Moreover, the network structure could enhance the diffusion of carbon/oxygen into the alloy, explaining the established mutual accelerating/catalyzing effect of oxidation and metal dusting leading to the degradation of the material.

7.1 Introduction

According to the classification by Szakalos, the possible active role of oxygen during metal dusting is the fundamental concept of Type III metal dusting mechanism in which carbon reacts with metal and metal carbides are formed, these carbides dissolve and oxidize selectively and carbon is released which forms new carbides/graphite which at their turn oxidize etc [30, 13, 32]. The mechanism has initially been indicated by several researchers, who have discussed the possible active role of oxygen during metal dusting conditions in combination with high steam contents of 30−50% [27, 28]. The phenomenon was first mentioned by Schmid et al. [29] in gas atmospheres with low steam content (23%). De Bruyn et al. [31] took the idea further and drew attention to the occurrence of internal oxidation during metal dusting, at least in reformer gas with high water vapour content, and suggested that the phenomenon may also occur with low water vapour content. As Schmid et al. expressed "The hypothesis of alternating carburizing and oxidizing conditions is in our view a promising starting point for the elucidation of additional facets of the metal dusting mechanism" [29]. On oxidizing stainless steel in steam internal oxidation occurs, such that nano-sized spinel particles develop coherently with the f.c.c matrix. The austenite matrix can be considered as a nano-network of metallic phases [62]. It is postulated that the metallic nano-network enhances the initiation of the metal dusting stage in carburizing. This hypothesis is tested in the present chapter. First, the microstructure occurring as a result of an oxidation experiment at 973K is explored. Afterwards two comparisons are made; i) a stainless steel AISI 316 sample is oxidized at 873K and subsequently carburized at 873K. The outcome is compared to a sample which is solely carburized at 873K. ii) a stainless steel AISI 316 sample is carburized at 923K and subsequently oxidized at 923K. The outcome is compared to a sample which is solely oxidized at 923K.

7.2 Experimental

Samples of austenitic stainless steel type 316 were used to conduct different types of heat treatments at various temperatures. The applied metal dusting conditions were a gas mixture of C_2H_2/H_2 for 24 hours. The applied oxidizing conditions were a gas mixture of Ar- 46% H_2O(g) for 169 hours.

7.2.1 Sample preparation

Bulk specimens of stainless steel AISI 316, with thickness 1mm, were used for carburization. The samples were ground on a Struers Abramin using successive finer sandpapers. Afterwards the samples were polished using 3μm- and finally 1μm diamond covered cloths. For recrystallization and austenitization, the specimens were heated to 1353K at a heating rate of 30K/min and upon reaching this temperature immediately cooled in pure H_2. During austenitization any deformation-induced martensite formed by manufacturing of the material was totally transformed to austenite. The furnace used for austenization was a horizontal laboratory tube furnace. After ended carburization/oxidation, the samples were mounted in resin and prepared by standard metallographic techniques. Finally, in order to emphasize the microstructures, samples were etched in Kallings reagent no.1.

7.2.2 Gaseous carburizing

Gaseous carburizing was performed in a custom built metal dusting furnace. Basically the furnace is a horizontal ceramic tube with the gas entering the furnace at one end and exiting at the other. Gaseous carburizing was performed in atmospheres of acetylene and hydrogen. The flows were adjusted by Brooks electronic mass flow controllers to: 5mL/min C_2H_2 and 15mL/min H_2. The carburization was performed at 773K, 823K, 873K and 923K. Heating to carburizing temperature was performed at a rate of 20K/min.

7.2.3 Oxidation

Oxidation of the bulk specimens was performed in a horizontal laboratory furnace with a gas mixture of argon and 46% H_2O(g). A water vapour content of 46 %H_2O(g) in argon was obtained by leading the argon through a distilled water bath which was kept at 353K. The overall pressure was approximately 1 bar. After passing the water bath, the gas mixture was lead immediately through the furnace without the possibility for condensation of water from the vapour phase. The oxidations were performed at 773K, 823K, 873K, 923K and 973K.

7.2.4 Scanning electron microscopy

Scanning electron microcopy (SEM) was carried out at Haldor Topsøe A/S with a FEI XL30 instrument, equipped with a field emission gun. The instrument incorporates energy dispersive X-ray spectrometry (EDS) for compositional analysis. The microscope was operated in high vacuum mode. SEM investigations were made on embedded samples for cross sectional analysis.

7.3 Results and interpretation

7.3.1 Oxidation

AISI 316 bulk specimens oxidized at four temperatures for 169 hours are depicted In Figure 7.1. It is evident that the layer thickness increases with temperature. The increasing oxide layer thickness is attributed to faster oxygen diffusion with temperature, but also to a change in the composition of the external oxide layer [62].

A backscattered electron (BSE) image of the sample oxidized at 973K (Figure 7.1d) for 169 hours is given in Figure 7.2. The thickness of the oxidized layer is about 35μm. The amount of for back scattered electrons increases with the atomic number. This implies that regions which are rich in transition metal elements such as chromium iron and nickel appear light when using the BSE detector, while regions with a high content of light elements such as carbon and oxygen appear dark. By inspection of the oxidized zone (Figure 7.2), it is clear that a an inner and an outer oxide zone have formed. The outer oxide layer is approximately 5μm in thickness while the inner oxide zone is approximately 30μm. The dark grayish color marking the grainboundaries in the inner oxide layer indicates that the grain boundary adjacent regions are heavily oxidized. Similarly, the outermost grains in the inner oxide scale appear to be more oxidized within the

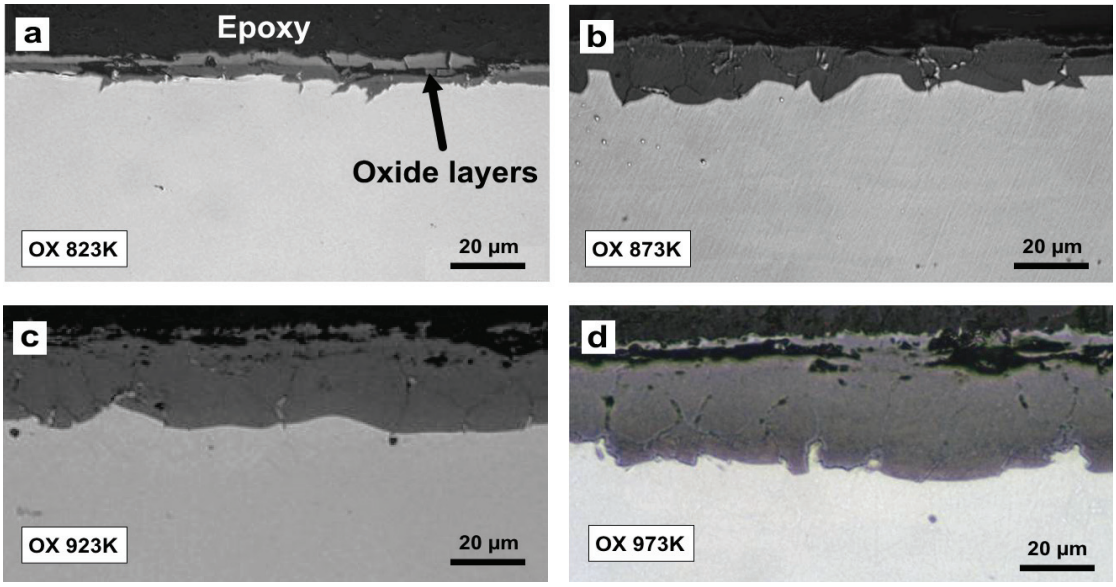

Figure 7.1: Reflected light microscopy images of the oxide layers formed as a consequence of oxidation in Ar-46%H_2O mixture for 169 hours at four different temperatures.

grains compared to the grains nearer the interface between the inner oxide scale and the alloy. A detailed explanation of the morphology in the inner oxide zone was provided in [62]. It appears as if the heavy oxidized grain boundaries slow down the oxide formation of the grains as indicated in Figure 7.2. Small enclosures limited to grain boundaries appear light and may be large particles of the alloy that has not or is modestly oxidized (analysis 7). EDS analyses of selected areas of the oxidized sample are presented in Table 7.1 in wt.%.

Analysis point	Cr	Fe	Ni
1	17.3	70.0	9.8
2	26.2	45.9	12.5
3	21.7	43.7	16.3
4	23.1	43.1	14.4
5	29.7	45.6	0.0
6	26.7	42.1	5.9
7	13.1	53.7	23.8
8	1.5	73.7	0.0
9	12.5	65.3	18.0

Table 7.1: EDS analyses (wt.%) of the sample oxidized at 973K for 169 hours. The applied acceleration voltage was 5kV, probing the surface.

According to the EDS analysis, the composition of elements in area 1 corresponds to the expected base alloy composition. In areas 2 and 3, a significant increase in chromium and nickel content is measured. The relative abundance of iron in these zones (2 and 3) accounts for the relative increase in nickel and chromium. By comparing the detected elements in the light area 4 with the dark area 5, it is observed that more chromium and less nickel are found in the dark area 5. This is explained from a redistribution of Ni (and Fe and Cr) associated with the occurrence of regions which are depleted in Ni (cf. region 5). The triple point in area six, appears dark and consists mainly of chromium and iron, with low amount of nickel. Additionally analysis 9 shows that the alloy is chromium depleted near the grain boundaries. The chromium depletion is caused by the diffusion of chromium from the nearby alloy towards the grain boundaries.

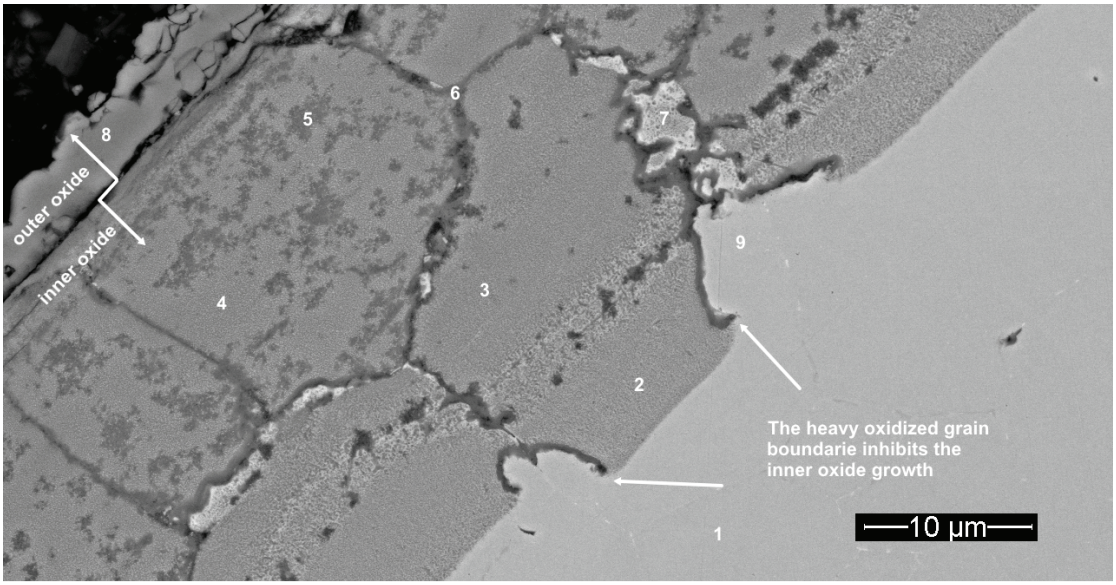

Figure 7.2: BSE image of the sample oxidized at 973K for 169 hours. The outer and inner oxide zones are clearly distinguished. The numbers represent selected areas analyzed with EDS. The numbers refer to the analysis number in Table 7.1

This indicates that the oxides at the grain boundaries most likely consist of mostly chromia or chromium rich spinel. Area 7, a small enclosure limited by grain boundaries, shows enrichment in nickel as well as chromium depletion. The analysis from area 8 shows that the outer oxide scale does not contain nickel and only very small amounts of chromium. One can conclude that the outer oxide scale is essentially an iron-based oxide. There is a distinct difference in the microstructures of the outer and the inner oxide layers. The outer layer appears homogenous (cf. Figure 7.2) while the metallic nano-network and oxide particles are present in the inner oxide layer as depicted in Figure 7.3. The oxide in the nano-network consists of a chromium-iron spinel as confirmed by the analysis of area 5. The analysis in area 5 is made in one of the large oxide particles inside a grain and has approximately the same element distribution as the smaller oxide on which the nano-network is build upon. This oxide does not contain any nickel and the metallic nano-network is therefore expected to be nickel-rich and most likely also contains iron.

From the SEM examinations and EDS it can be concluded that after oxidation of austenitic stainless steel type 316 in a gas mixture of argon and 46% water vapour at 973K, a consistent double layer is formed. The outer layer consists of iron oxides, while the inner oxide layer has oxidized grain boundaries of chromium- iron spinel and a metallic nano-network and oxide nano-particles inside the grains. The relatively fast growth of the inner oxide zone is possible by an internal oxidation mechanism. Comparing the reflected light images of the sample with an identified nano-network with reflected light images of samples exposed to the same conditions but at temperatures of 773K (not included), 823K, 873K and 923K, it was found that a similar layer was present at the samples exposed at 873K and 923K. The layer was not present on the sample exposed at 773K instead the sample was covered by a thin oxide layer consisting of $Cr_2O_3/FeCr_2O_4$ oxides, which effectively hinders oxygen transfer. The metallic nano network found on the sample oxidized at 973K was confirmed by SEM to be present on samples containing an internal oxidized zone, hence also on the samples oxidized at 923K.

7.3.2 The effect of oxidation and metal dusting at 773K

To evaluate the effect of oxidation and metal dusting on material degradation a sample that has been exposed to metal dusting conditions was subsequently exposed to oxidizing conditions and vice versa. The carburization and oxidation were conducted at 773K for 24 hours and 169 hours,

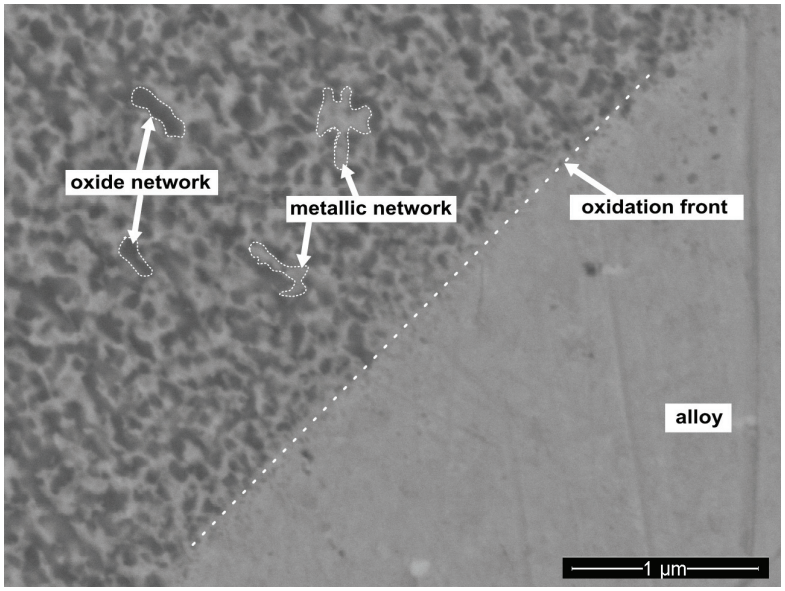

Figure 7.3: BSE image of the sample oxidized at 973K for 169 hours. The oxidation front, the oxide particles and metallic nano-network are indicated in the figure. The image area corresponds to the analysis 2 in Figure 7.2.

respectively. Reflected light images of the samples are presented in Figure 7.4.

Comparing the thickness of the carbon expanded zone (γ_C) on the carburized sample (Figure 7.4c) with the thickness on the oxidized and subsequently carburized sample (Figure 7.4b) shows that the oxide layer formed during the oxidation has hindered the carbon transfer from the atmosphere into the material. This observation is interpreted such that the time for the acetylene gas to breakdown the surface oxide layer, and thereby activating the surface, is prolonged for the pre-oxidized surface. The oxide layer formed during the oxidation is so thin that it is not visible on the micrograph in Figure 7.4a. It was shown in previous work [62] that the oxide layer developed under the applied oxidizing conditions is a $Cr_2O_3/FeCr_2O_4$ oxide layer, which effectively hinders the oxygen transfer and apparently, also the carbon transfer, albeit to a lesser extent. Exposing the sample to metal dusting conditions prior to oxidation strongly accelerates the oxidation of the sample surface. This is verified by inspection of the micrograph in Figure 7.4d, where a dark zone has developed and material from the surface has spalled off. The nature of the dark zone has not been established in the present work, but could be interpreted as internal oxidation. The reason why an internally oxidized zone develops on the pre-carburized sample while such a zone does not develop on direct oxidation under the present conditions, could be explained as follows; the pre-carburization in C_2H_2 has effectively removed, or transformed, the native oxide layer on stainless steel, such that the surface allows the incorporation of carbon from the gas phase. Evidently, after carburization and during oxidation a protective oxide layer, most likely Cr_2O_3, is not restored, thus allowing internal oxidation of the previously carburized zone. Also a thin external oxide layer develops. These results indicate that exposure to metal dusting conditions has a detrimental effect on the resistance against oxidation in Ar-46% H_2O(g).

7.3.3 The effect of oxidation and metal dusting at 923K

As previously discussed the oxide layer formed during pre-oxidation at 773K, acts as a barrier for carbon transfer from the atmosphere into the material, thus effectively delaying the onset of metal dusting. Results, not presented here, showed the same tendency for pre-oxidation and subsequent carburization at 823K, although the carbon ingress was more pronounced than at 773K. As will be shown in the following, for temperatures at 923K, the oxide layer formed during oxidation is no longer inhibiting the carbon transfer from the atmosphere into the material, just as it no longer hinders transfer of oxygen into the steel and causes internal oxidation [62]. The

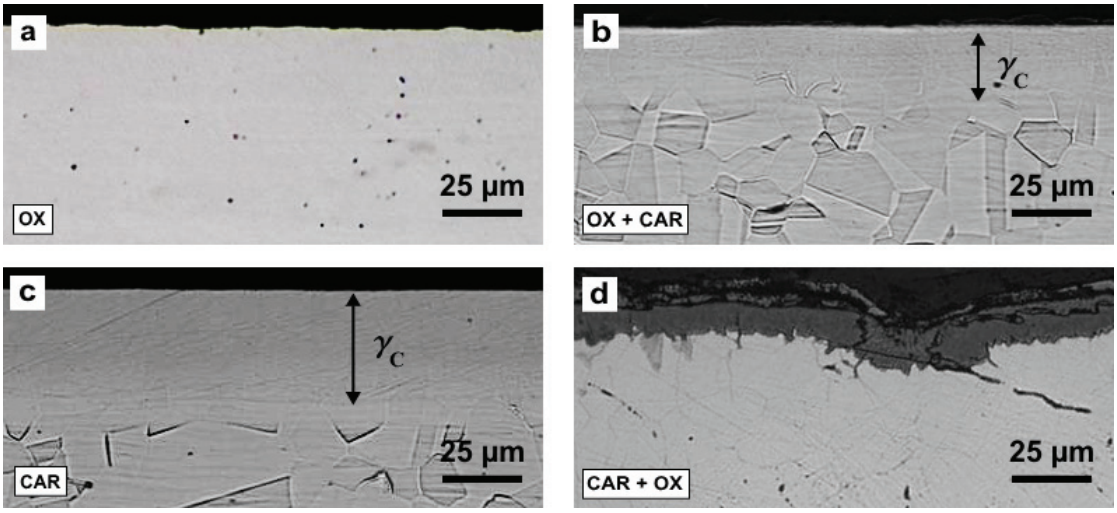

Figure 7.4: Reflected light images of an oxidized sample (a), carburized sample (c) and combinations thereof (b and d). The carburization and oxidation were conducted at 773K for 24 hours and 169 hours, respectively.

carburization and oxidation were conducted at 923K for 24 hours and 169 hours, respectively.

In Figure 7.5 reflected light images of an oxidized sample, a carburized sample and combinations thereof are shown for temperatures at 923K. In the oxidized sample (Figure 7.5a) an internal oxide zone is present. In the carburized sample (Figure 7.5c) indications of carbide formation along the grain boundaries and formation of, what is most likely a carbide rich surface layer as observed previously in the metal dusting sequence on foils, albeit at 823K, is observed. In the oxidized and subsequently carburized sample (Figure 7.5b), the former inner oxide layer (see Figure 7.5a) is transformed, or replaced by, a hard and brittle phase in which indications of the former alloy grain boundaries are present. It is clear that carbon has been transferred through the oxide layer and has formed carbides in a comparative way to the carburized sample (Figure 7.5c) which has not been oxidized. In the carburized and subsequently oxidized sample (Figure 7.5d), a banded morphology is again observed. Outmost, a columnar structured oxide phase is present. Underneath a hard zone is present. In the following a detailed SEM analysis of the samples in Figure 7.5b and d is presented.

SEM investigation of oxidized subsequently carburized samples

A SEM investigation of the oxidized and subsequently carburized sample (Figure 7.5b) is presented in Figure 7.6. The internally oxidized zone that developed during oxidation is replaced by a phase in which indications of the former alloy grain boundaries are present. By inspection of Figure 7.6a and b it is clear that entire grains falls out of, and the original surface is marked with a white line in Figure 7.6a. Due to the BSE signal heavy elements will appear light, evidently, from Figure 7.6b, the grain boundaries separating the repelled grains from the base alloy are populated with light elements and consequently appear dark. EDS analysis was made in locations near these dark areas adjacent to a grain boundary as depicted in Figure 7.6c. The result of the EDS measurements is shown in Table 7.2.

The measurement in location 1, obtained inside the metallic nano-network adjacent to a grain boundary, shows a significantly increased amount of carbon as compared to the unaffected metallic nano-network in location 2. Although light elements (C and O) are not precisely quantifiable with EDS, the measured difference is assumed to surpass the associated uncertainty. The increased concentration of carbon, not only indicates the presence of the C_2H_2 gas, but also a decomposition of C_2H_2. Porosity at grain boundaries could be a possible way for C_2H_2 to get in. Such porosities are actually observed in or adjacent to Ni-rich regions. The apparent carbon ingress into the metallic nano-network (EDS location 1 vs. EDS location 2 in Figure 7.6c) is

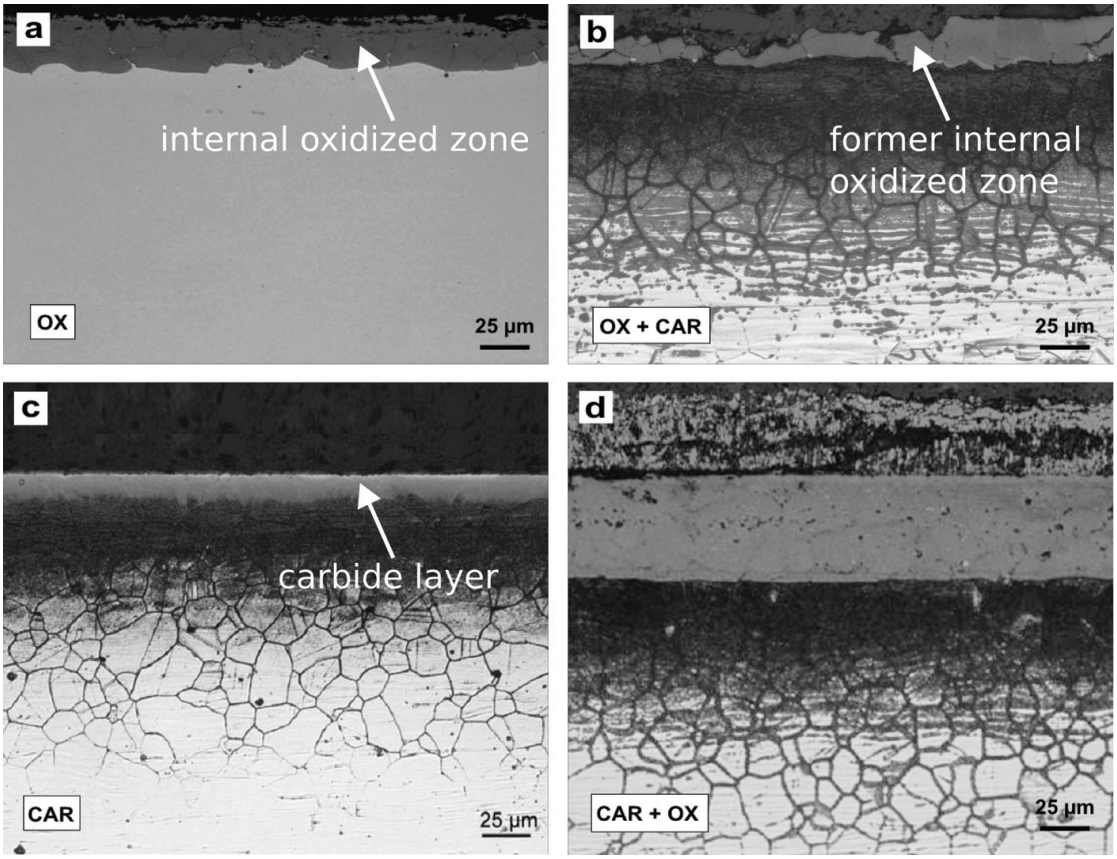

Figure 7.5: Reflected light images of an oxidized sample (a), carburized sample (c) and combinations thereof (b and d). The carburization and oxidation were conducted at 923K for 24 hours and 169 hours, respectively.

Analysis point	Cr	Fe	Ni	O	C
1	27.7	25.8	4.4	18.1	17.5
2	20.9	39.9	19.4	12.8	2.4
3	16.0	62.3	10.5	0.1	6.4
4	8.2	67.3	17.6	0.0	3.6
5	21.7	38.7	18.2	14.8	1.7

Table 7.2: EDS results obtained in the locations indicated in Figure 7.6c and d. Compositions are given in wt.%. The applied acceleration voltage was 5kV.

anticipated to be accelerated by; i) an enhanced decomposition of the acetylene gas catalyzed by the metallic particles present in the internal oxide zone, ii) a considerably enhanced carbon transport due to the metallic nano-network. The carbon ingress into grain boundary adjacent areas is assumed to assist the de-attachment of the entire grains, explaining the observed repelling of the grains from the surface. It is believed that the metal dusting mechanism occurring when the sample has been pre-oxidized at 923K is one of the new models which rely on the presence of a nano-network consisting of oxides and metallic nano-particles into which the carbon can diffuse rapidly.

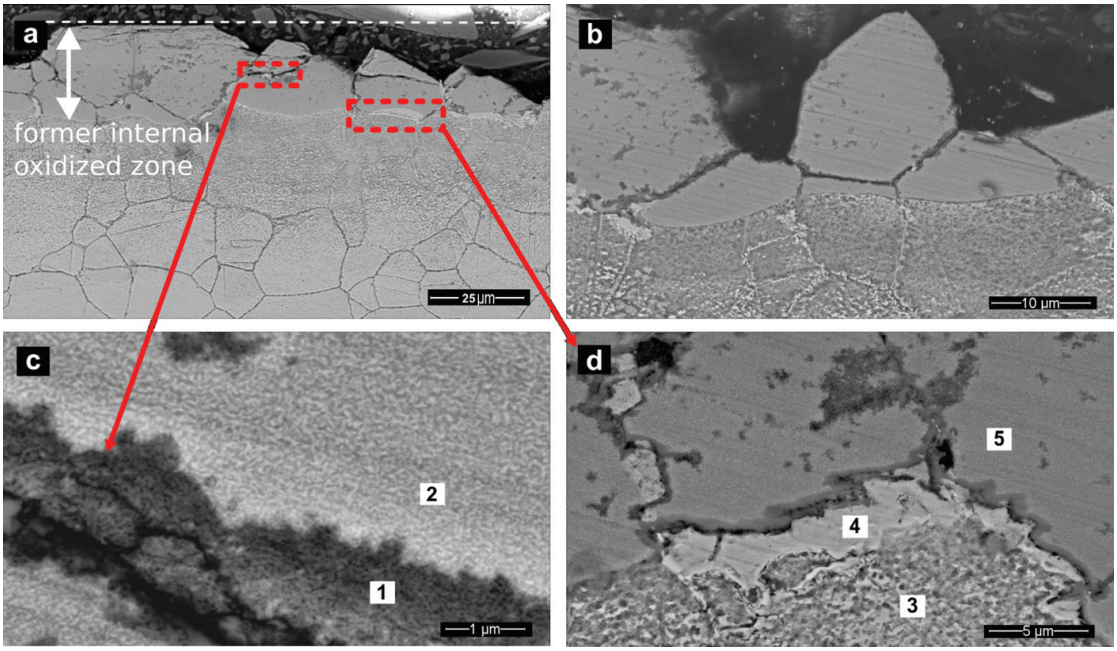

Figure 7.6: SEM, BSE micrographs of the oxidized and subsequently carburized sample (Figure 7.5b). The carburization and oxidation was conducted at 923K for 24 hours and 169 hours, respectively. The white line in (a) marks the level of the original surface from where whole grains are repelled. EDS analysis was performed in the numbered areas in (c) and (d).

As observed in Figure 7.6a, a bright zone is located underneath the former internal oxidized zone. EDS analysis in the bright zone (point 4 in Figure 7.6d), shows a high amount of metallic species. The composition measured in location 5 is similar to the composition measured in location 2. In location 3 beneath the bright zone and past the former internal oxidized zone a lower Ni content is measured as expected as we are no longer inside the metallic nano-network area.

From the above analysis it is evident that carburization of an oxidized sample at 923K results in an increased material wastage as observed by the spalling-off of entire grains from the surface. This is contrary to the observations for lower temperatures, and can be explained from the change in composition of the external oxide layer and the associated internal oxidation.

SEM investigation of carburized subsequently oxidized samples

A SEM investigation of the carburized and subsequently oxidized sample (Figure 7.5d) is presented in Figure 7.7 in which a banded morphology is distinctively visible. In Figure 7.7a numbers 1-3 indicate the main features in the surface and subsurface zones. It is presumed that area 1 marks the internal carburized zone with carbide precipitations along grain boundaries. Area 2 marks an internal oxidation zone probably formed by internal oxidation of the carbide rich zone formed during carburization. Former grain boundaries of austenite is visible in this region. Area 3 is an outer oxide scale. Results of EDS analysis made in location 1-3 are given in Table 7.3.

In location 2 an increased Ni content and decreased Fe content is found as compared to location 1 and 3. This is consistent with the presence of a Ni-rich metallic nano-network. From EDS analysis point 3 it is evident that the outer scale is Cr depleted and consist of Fe and O. By closer inspection of the outmost layer (Figure 7.7b), repelling of material from the surface is observed. The composition in location 5 shows that the sample material loss consists of Fe. The loss of Fe explains the relative abundance of Ni in location 2. The composition in location 4 indicates the presence of a carbon/graphite protrusion. Embedding of graphite particles is found in the entire of area 3. The graphite particles are further investigated in Figure 7.8 in which the secondary electron detector was applied to enhance the morphology.

The outer scale is essentially composed of Fe-based oxides and is subdivided in three layers: a thin layer at the surface, a slightly thicker layer underneath and a relatively broad zone on top of the internal oxidation zone. These three oxide layers are (at the oxidation temperature) Fe_2O_3, Fe_3O_4 and $Fe_{1-\delta}O$, respectively (on cooling $Fe_{1-\delta}O$ transforms to Fe_3O_4). The occurrence of porosity in the wustite layer (cf. Figure 7.7b) is consistent with general observations on the oxidation of iron [63]. On oxidation and growth of the outer scale it is expected that carbon is removed by CO/CO_2 development. In the internal oxidation zone carbon is pushed ahead of the oxidation front, which is very sharp. Apparently, no $(Fe,Cr)_3O_4$ layers develop along grain boundaries as is the case for direct oxidation. This is explained from the presence of carbides ($M_{23}C_6$) after the pre-carburization treatment, which formed a mere uniform layer at the surface (cf. Figure 7.5c). During oxidation these carbides are transformed to oxides, Fe leaves this region for the development of the iron oxide outer scale, and carbon is partly removed by $CO/CO_2/CH_4$ formation and partly pushed ahead of the growing internal oxide zone. The presence of carbon rich particle, most likely graphite, in the outer scale is explained from the presence of porosity in the wustite layer, where graphite apparently can nucleate.

Analysis point	Cr	Fe	Ni	O	C
1	17.9	57.1	8.5	1.5	11.1
2	22.1	38.2	15.8	16.2	2.8
3	0.8	62.5	1.4	22.9	11.2
4	7.0	2.1	0.0	1.0	89.8
5	0.3	66.1	0.5	26.5	5.5

Table 7.3: EDS results obtained in the locations indicated in Figure 7.7. Compositions are given in wt.%. The applied acceleration voltage was 5kV.

7.4 Conclusion

From this preliminary study of the mutual accelerating/catalyzing effect of oxidation and carburization on metal dusting corrosion, several important findings are noted. At low temperatures (773K), pre-oxidation retards the carbon uptake. However, pre-carburization in C_2H_2 removes the native oxide layer on stainless steel which means that formation of an internal oxidation zone is formed during subsequent oxidation, which was shown not to be possible without pre-carburization. At elevated temperatures (923K) pre-oxidation accelerates the subsequent carburization because of internal oxidation and other composition of external oxide layer. It can be concluded that, the mutual influence of carbon and oxygen accelerates the material degradation.

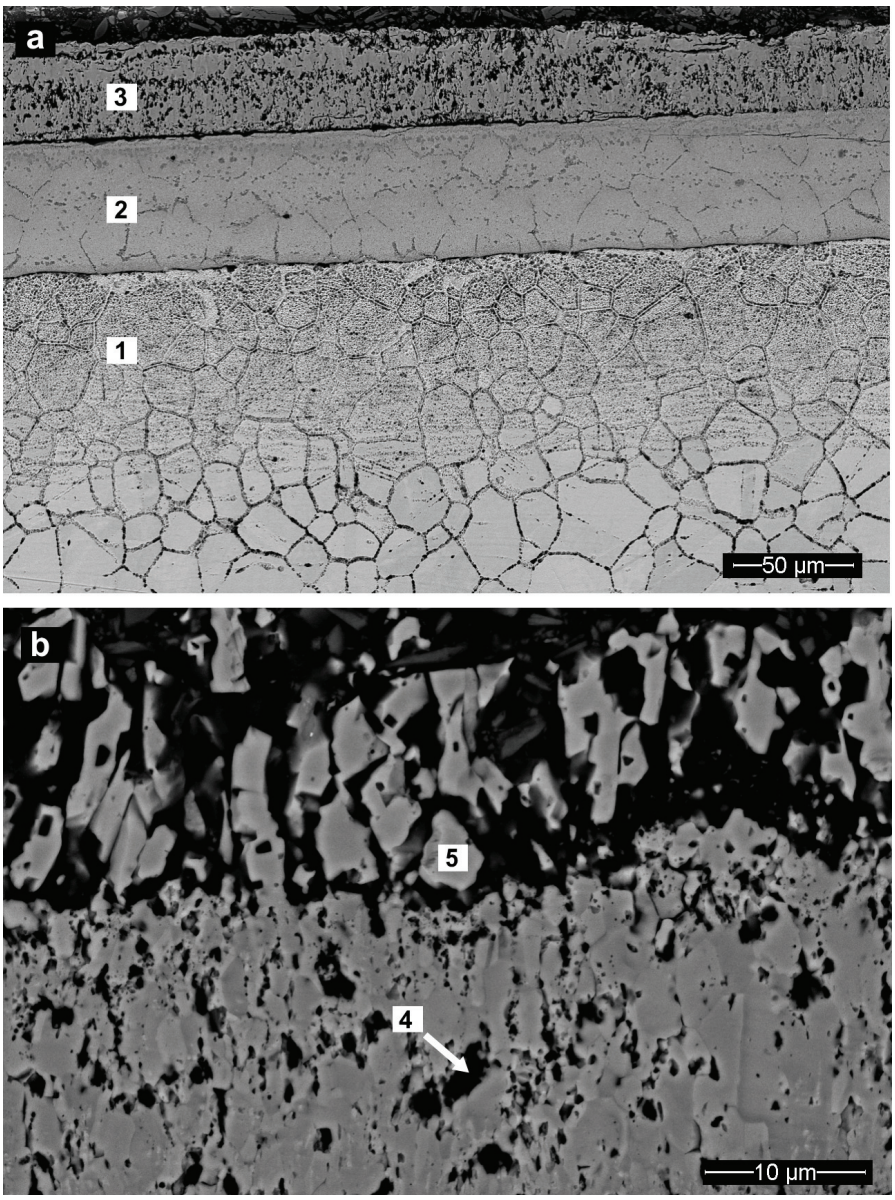

Figure 7.7: SEM, BSE micrographs of the carburized and subsequently oxidized sample (Figure 5d). The carburization and oxidation was conducted at 923K for 24 hours and 169 hours, respectively. EDS analysis was performed in the numbered areas in 1 to 5.

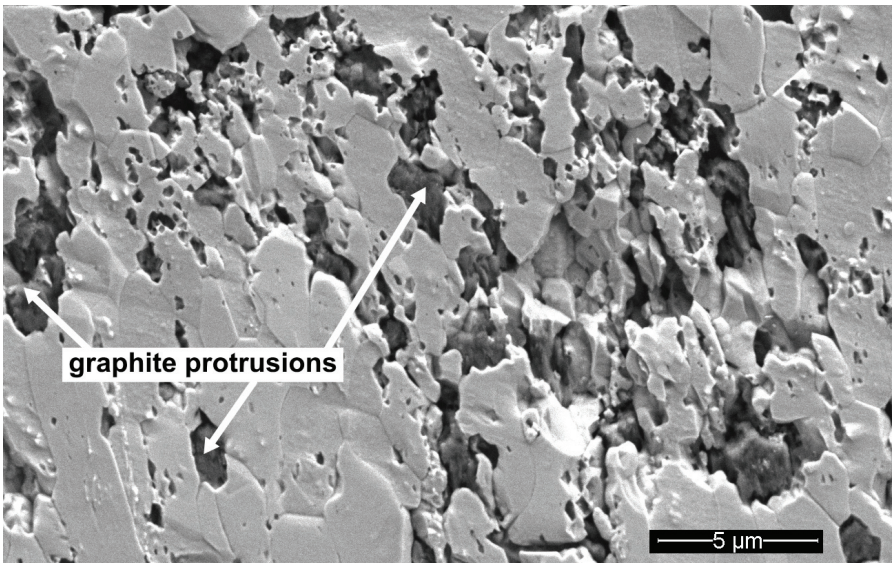

Figure 7.8: SEM, SE micrograph of the graphite particles embedded in the outmost columnar zone (area 3 in Figure 7.7).

8 Summary and outlook

8.1 Summary

The initial steps of the catastrophic carburizing corrosion, metal dusting, were explored. It was found that the formation of carbon expanded austenite and the subsequent decomposition hereof is significantly involved in the mechanism. This has to be incorporated in a complete description of metal dusting corrosion. By applying a carburizing gas of C_2H_2, a superior surface activation of the stainless steel was accomplished. Combined with the simultaneous high carburizing potential, it was possible to by-pass the incubation time allowing fast and systematic investigations. The unorthodox approach resulted in fundamental insight into the formation and decomposition of carbon expanded austenite. Kinetic and thermodynamical parameters were assessed. The main findings in the present work can be summarized as follows:

- The lattice parameter of expanded austenite as a function of interstitially dissolved carbon was determined by carburization of thin stainless steel foils. For the first time this dependency was determined on unstrained austenite at room temperature. The lattice parameter was found be linear dependent on the occupancy of the octahedral interstices, y_C.
- The concentration dependent diffusion coefficient of carbon in expanded austenite was determined by a boost-carburization and subsequent homogenization strategy of thin foils. It was found that the diffusion coefficient of carbon in expanded austenite increases with carbon concentration. However the obtained diffusion coefficients may be interpreted as an effective diffusion coefficient under the influence of surface kinetics (CO carburization) and the presence of tiny coherent carbides (C_2H_2 carburization).
- Detailed temperature resolved analysis of the decomposition of carbon expanded austenite was achieved. The influence of several parameters such as thermal history, carbon content, sample geometry and the presence of precursors and possibly the influence of compressive stresses were investigated. It was hypothesized that carbide precursors formed during carburization in C_2H_2, as low as 613K. This hypothesis was substantiated by several observations throughout the thesis.
- A systematic study of AISI 316 stainless steel foils exposed to a mixture of C_2H_2 and H_2 at 823K captured the entire metal dusting course from the initial stage of dissolution of carbon atoms in the surface region by carburization and the formation of carbon expanded austenite, γ_C, to the eventual disappearance of the foils. Investigations of TEM samples, prepared by means of FIB, revealed a lamellar structure with $M_{23}C_6$ carbides and austenite.
- Finally, the mutual influence of oxygen and carbon on the metal dusting corrosion was explored. The results indicate that exposure to metal dusting conditions has a detrimental effect on the resistance against oxidation and, conversely, that exposure to oxidation has a detrimental effect on the resistance towards metal dusting. Consequently, a combination of carburizing and oxidizing conditions has a strong mutual catalyzing effect on the metal dusting corrosion.

8.2 Outlook

The formation and decomposition of carbon expanded austenite precede the metal dusting corrosion. Fundamental insight into its development and to the parameters influencing its decomposition, can be valuable in the design of metal dusting resistant materials. Until now, the systematic investigation of metal dusting and the influence of alloying elements on the metal dusting resistance, has been obscured by the long incubation times. Following the approach provided in this thesis, fast and effective alloy screening studies can be carried out.

Let me end this thesis by presenting a snapshot from a very preliminary screening study of Ni-based stainless steels, in which a Nimonic 80 alloy has been exposed to metal dusting conditions of C_2H_2 and H_2 at 823K for 60 hours. The metal dusting attack is clearly identifiable, In Figure 8.1.

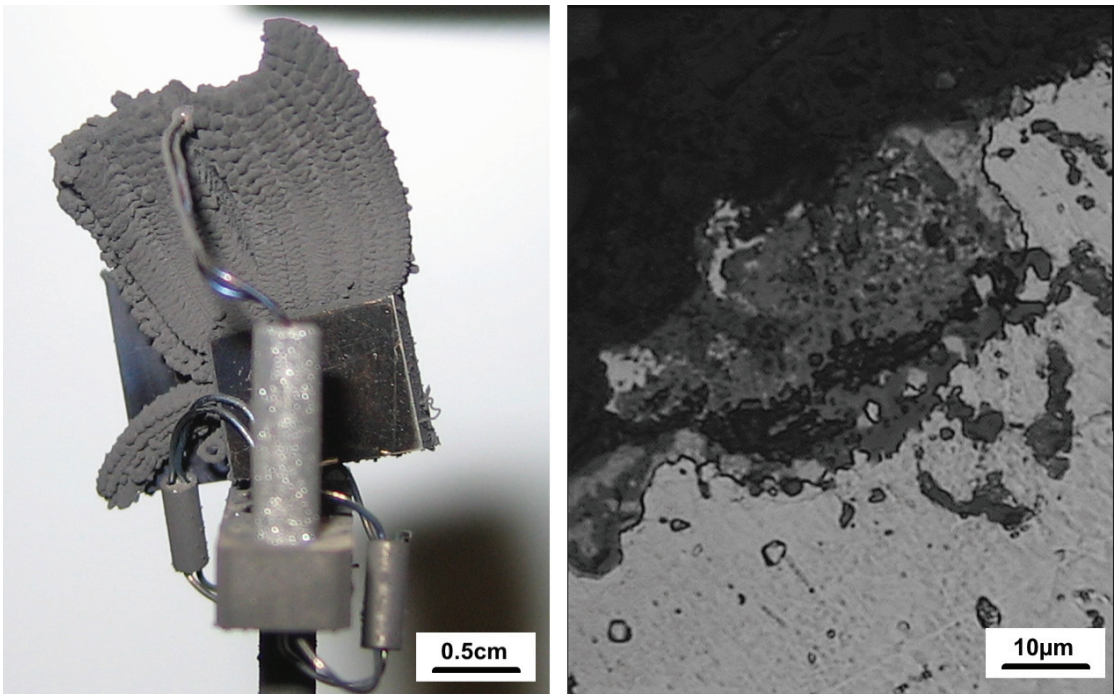

Figure 8.1: Metal dusting corrosion of Nimonic 80, occurring already after 60 hours in a gas mixture of C_2H_2 and H_2 at 823K. Heavy formation of filamentous carbon is visible. (left) image is acquired just after opening the thermobalance, (right) reflected light image of the polished cross section of the attacked area.

Bibliography

[1] Perkins, R., Padgett, R., and Tunali, N. *Metallurgical and Materials Transactions B* **4**(11), 2535–2540 (1973).

[2] Perkins, R. *Metallurgical and Materials Transactions B* **4**(7), 1665–1669 (1973).

[3] Goldschmidt, HJ, B. and CO. LTD, L. *Interstitial alloys*. (1967).

[4] Grabke, H. *Materials and Corrosion* **54**(10), 736–746 (2003).

[5] Grabke, H. *Materials and Corrosion* **49**(5), 303–308 (1998).

[6] Grabke, H. J. *Diffusion and Defect Data - Solid State Data - Part B - Solid State Phenomena* **41**, 3 (1995).

[7] Zeng, Z., Natesan, K., and Maroni, V. *Oxidation of Metals* **58**(1), 147–170 (2002).

[8] Hochman, R. and Burson III, J. *API Division of Refining Proc* **46**, 331–44 (1966).

[9] Grabke, H., Krajak, R., and Paz, J. *Corrosion science* **35**(5-8), 1141–1150 (1993).

[10] Helveg, S., López-Cartes, C., Sehested, J., Hansen, P., Clausen, B., Rostrup-Nielsen, J., Abild-Pedersen, F., and Nørskov, J. *Nature* **427**(6973), 426–429 (2004).

[11] Zhang, J., Schneider, A., and Inden, G. *Corrosion Science* **45**(6), 1329–1341 (2003).

[12] Inden, J. *Werkstoffe und Korrosion* **54**(10) (2003).

[13] Szakalos, P. *Materials and Corrosion* **54**(10), 752–762 (2003).

[14] Motin, M., Munroe, P., Brady, M., and Young, D. *Scripta materialia* **56**(4), 281–284 (2007).

[15] Zhang, J., Schneider, A., and Inden, G. *Materials and Corrosion* **54**(10), 763–769 (2003).

[16] Toh, C., Munroe, P., and Young, D. *Materials at high temperatures* **20**(4), 527–534 (2003).

[17] Chun, C., Mumford, J., and Ramanarayanan, T. *Journal of the Electrochemical Society* **149**, B348 (2002).

[18] Young, D. *Materials Science Forum* **522-523**, 15–26 (2006).

[19] Pippel, E., Woltersdorf, J., and Schneider, R. *Materials and Corrosion* **49**(5), 309–316 (1998).

[20] Schneider, R., Pippel, E., Woltersdorf, J., Strauss, S., and Grabke, H. *steel research* **68**(7), 326–332 (1997).

[21] Chun, C., Mumford, J., and Ramanarayanan, T. *Journal of the Electrochemical Society* **147**, 3680 (2000).

[22] Zeng, Z. and Natesan, K. *Chem. Mater* **15**(4), 872–878 (2003).

[23] Bernst, R., Schneider, A., and Spiegel, M. *Materials and Corrosion-Werkstoffe und Korrosion* **57**(9), 724–728 (2006).

[24] Bloch, B., Ravi, B., and Chaim, R. *Materials Letters* **42**(1-2), 61–65 (2000).

[25] Chun, C. and Ramanarayanan, T. *Oxidation of Metals* **62**(1), 71–92 (2004).

[26] Toh, C., Munroe, P., and Young, D. *Oxidation of Metals* **58**(1), 1–21 (2002).

[27] Perkins, R., Coons, W., and Radd, F. *The Electrochemical Society, Inc* , 733–749 (1976).

[28] Eberle, F. and Wylie, R. *Corrosion* **15**, 622–626 (1959).

[29] Schmid, B., Grong, Ø., and Ødegård, R. *Materials and Corrosion* **50**(11), 647–653 (1999).

[30] Szakalos, P., Pettersson, R., and Hertzman, S. *Corrosion Science* **44**(10), 2253–2270 (2002).

[31] de Bruyn, H., Brendryen, S., and Edwin, E. *CORROSION 2001* (2001).

[32] Szakalos, P. In *Materials science forum*, volume 522, 571. Transtec Publications; 1999, (2006).

[33] Z.I. Zhang, T. B. *surface enginnering* **1**, 131–136 (1985).

[34] Sun, Y., Li, X., and Bell, T. *Materials Science and Technology* **15**(10), 1171–1178 (1999).

[35] Ichii, K., Fujimura, K., and Takase, T. *Technol. Rep. Kansai Univ.* (27), 135–144 (1986).

[36] Christiansen, T. and Somers, M. *Scripta Materialia* **50**(1), 35–37 (2004).

[37] Christiansen, T. L. and Somers, M. A. *Metallurgical and Materials Transactions A: Physical Metallurgy and Materials Science* **40**(8), 1791–1798 (2009).

[38] Ernst, F., Cao, Y., and Michal, G. *Acta Materialia* **52**(6), 1469–1477 (2004).

[39] Albertsen, J. *Experimental and theoretical investigations of metal dusting corrosion in plant exposed nickel-based alloys*. PhD thesis, Norwegian University of Science and Technology, Faculty of Natural Sciences and Technology, (2007).

[40] Somers, M. and Christiansen, T. *PCT/DK2006/000363* (2006).

[41] Blazek, A. *Thermal Analysis*. Van Nostrand Reinhold, (1973).

[42] Wendlandt, W. *Thermal methods of analysis*. Wiley Interscience, (1974).

[43] Somers, M., Christiansen, T., and Møller, P. (Danish Patent DK174707 B1 and PCTDK03/00497).

[44] Detroye, M., Reniers, F., Buess-Herman, C., and Vereecken, J. *Applied Surface Science* **144**, 78–82 (1999).

[45] of Materials, I. *Stainless Steel 2000: Thermochemical Surface Engineering Of Stainless Steel*. Institute of Materials, (2001).

[46] Christiansen, T. and Somers, M. *Surface Engineering, 21* **5**(6), 445–455 (2005).

[47] Hummelshøj, T. *Surface Modification Technologies XXII, Proc. 22nd Inter. Conf. Surface Modification Technologies* , 199–206 (2009).

[48] Christiansen, T. and Somers, M. *International Journal of Materials Research* **99**(9), 999–1005 (2008).

[49] Hummelshøj, T. S., Christiansen, T., and Somers, M. A. *Diffusion and Defect Data. Pt A Defect and Diffusion Forum* **273-276**, 306–311 (2008).

[50] Cheng, L., Bottger, A., de Keijser, T., and Mittemeijer, E. *Scr. Metall. Mater.* **24**(3), 509–514 (1990).

[51] Kahn, H., Michal, G., Ernst, F., and Heuer, A. *Metallurgical and Materials Transactions A* **40**(8), 1799–1804 (2009).

[52] Ridley, N., Stuart, H., and Zwell, L. *TRANS MET SOC AIME* **245**(8), 1834–1836 (1969).

[53] Michal, G., Gu, X., Jennings, W., Kahn, H., Ernst, F., and Heuer, A. *Metallurgical and Materials Transactions A* **40**(8), 1781–1790 (2009).

[54] Christiansen, T., Dahl, K., and Somers, M. *Materials Science and Technology* **24**(2), 159–167 (2008).

[55] Strauss, S., Krajak, R., and Grabke, H. *Materials and Corrosion* **50**(11), 622–627 (1999).

[56] Crank, J. *The mathematics of diffusion.* Oxford University Press, USA, (1979).

[57] Christiansen, T., Dahl, K., and Somers, M. *Diffusion and Defect Data. Pt A Defect and Diffusion Forum* **258-260**, 378–383 (2006).

[58] Wells, C., Batz, W., and Mehl, R. *American Institute of Mining and Metallurgical Engineers – Journal of Metals* **188**(3), 553–560 (1950).

[59] Erley, W. and Wagner, H. *Surface Science* **74**(2), 333–341 (1978).

[60] *ThermoCalc; version S, database TCFE6.1.*

[61] Ernst, F., Cao, Y., Michal, G., and Heuer, A. *Acta Materialia* **55**(6), 1895–1906 (2007).

[62] Hansson, A. N., Panthelon, K., Grumsen, F. B., and Somers, M. A. J. *Oxidation of Metals* , DOI 10.1007/11085–009–9182–x pp. 289–209 (2010).

[63] Kofstad, P. *High temperature oxidation of metals* , 179 (1966).

Paper I

Defect and Diffusion Forum Vols. 273-276 (2008) pp 306-311
online at http://www.scientific.net

Online available since 2008/Feb/11

Determination of Concentration Dependent Diffusion Coefficients of Carbon in Expanded Austenite

Thomas S. Hummelshøj[a], Thomas Christiansen[b] and Marcel A.J. Somers[c]

Technical University of Denmark
Department of Manufacturing Engineering and Management
Kemitorvet b. 204
DK-2800 Kgs. Lyngby
Denmark

[a]tsh@ipl.dtu.dk, [b]tc@ipl.dtu.dk, [c]somers@ipl.dtu.dk

Keywords: Stainless steel; Kinetics; Diffusion

Abstract. In the present paper various experimental procedures to experimentally determine the concentration dependent diffusion coefficient of carbon in expanded austenite are evaluated. To this end thermogravimetric carburization was simulated for various experimental conditions and the evaluated composition dependent diffusivity of carbon derived from the simulated experiments was compared with the input data. The most promising procedure for an accurate determination is shown to be stepwise gaseous carburizing of thin foils in a gaseous atmosphere; the finer the stepsize, the more accurate the approximation of the diffusivity. Thermogravimetry was applied to continuously monitor the weight change of thin foils of AISI 316 during carburizing in CO-H_2 gas mixtures for one of the simulated experimental procedures.

Introduction

Austenitic stainless steels are widely applied for their corrosion-resistant performance, both at atmospheric temperature and at elevated temperature. Engineering these materials towards an improvement of the wear resistance while maintaining the corrosion resistance has been accomplished by deliberately dissolving large amounts of carbon into the surface by carburizing at a temperature below which effectively no carbides develop [1-3]. The resultant carburized layer is characterized by a supersaturated solid solution of carbon atoms residing in the octahedral interstices of the austenite lattice. In order to tailor the properties and thermochemical carburizing treatment conditions it is necessary to be able to simulate the evolution of the carbon concentration profile in the solid state during treatment and to prevent the development of alloying element carbides that would impair the corrosion resistant performance of stainless steels.
On the other hand application of austenitic stainless steels at elevated temperature in a carburizing environment may lead to unintended catastrophic carburization known as metal dusting, i.e. the dissolution of carbon in the solid state and the subsequent development of carbides eventually leading to a degradation of the material by coking [4,5]. Process equipment in the petrochemical industry commonly suffers from metal dusting. This aggressive interaction between stainless steels (as well as nickel alloys) and carbon-bearing gases has been subjected to many studies [6,7], however, so far, no accurate simulation of the carburizing stage prior to the actual metal dusting stage has been presented. A prediction of the carburizing kinetics involved in surface engineering as well as metal dusting of stainless steels demands fundamental knowledge concerning the diffusion of carbon in expanded austenite, i.e. austenite with a high supersaturation of carbon. So far very few

studies have focused on and succeeded in obtaining reliable thermodynamic (i.e. carbon solubility in terms of carbon activity) and kinetic (i.e. diffusion) data on expanded austenite stabilized by carbon.

Generally, under practical circumstances the protective oxide scale on stainless steel delays the onset of the carburizing reaction. This implies that the initiation of so-called metal dusting pits is stochastic in nature. One of the strategies in materials design is therefore the improvement of the oxide layer's stability in a carburizing environment and thereby prolong the incubation time for metal dusting initiation. The stochastic nature of oxide layer breakthrough also implies that deliberate carburizing of stainless steel surfaces requires an activation step, wherein the protective oxide layer is removed or by-passed. A successful pretreatment method was recently patented: the native oxide layer was electrochemically replaced by a very thin (10-20 nm) metal layer, which prevents the surface from forming a protective oxide scale and which catalyzes the surface reaction necessary to liberate carbon atoms from carbon-containing species in the gas mixture [8].
The present work is devoted to the evaluation of the composition dependent diffusion coefficient of carbon in expanded austenite from sorption curves determined on thin foils of austenitic stainless steel with thermogravimetry. Firstly, the initial rate method originally proposed by Crank is briefly discussed. Thereafter three measurement strategies for an experimental assessment are evaluated by simulation of the sorption curves and determination of the diffusion coefficients according the initial rate method applied to these sorption curves. Finally, the concentration dependent diffusivity of carbon in expanded austenite is experimentally determined for one of the three evaluated measurement strategies.

Theory and simulation of sorption curves

Initial rate method for determination of diffusion coefficient

Consider a slab of material with thickness l, wherein the diffusion coefficient of the diffusing species j is designated by D_j. For the early stages of diffusion-controlled sorption of component j, the total amount of component j, M_t, incorporated in the slab at time t, amounts to [9]:

$$\frac{M_t}{M_\infty} = \frac{4}{\pi^{\frac{1}{2}}}\left(\frac{D_j t}{l^2}\right)^{\frac{1}{2}} \qquad (1)$$

where M_{inf} is the total amount of component j that has entered the sample after infinitely long sorption time. In a sorption (carburizing) experiment the initial slope in a plot of $\left(M_t/M_\infty\right) vs. \left(t/l^2\right)^{1/2}$ is directly proportional to the diffusion coefficient D_j. If the diffusivity D_j depends on the concentration, C, of component j and the concentrations of component j prior to and after sorption are C_0 and C_s, respectively, the value obtained can be conceived as an average diffusion coefficient $\overline{D}_j$ [9]:

$$\overline{D}_j\left((C_s + C_0)/2\right) = \frac{1}{C_s - C_0}\int_{C_0}^{C_s} D_j(C)dC \qquad (2)$$

Obviously, the narrower the composition range C_s-C_0, the closer the value for $\overline{D}_j\left((C_s + C_0)/2\right)$

approaches the actual diffusivity $D_j((C_s + C_0)/2)$.

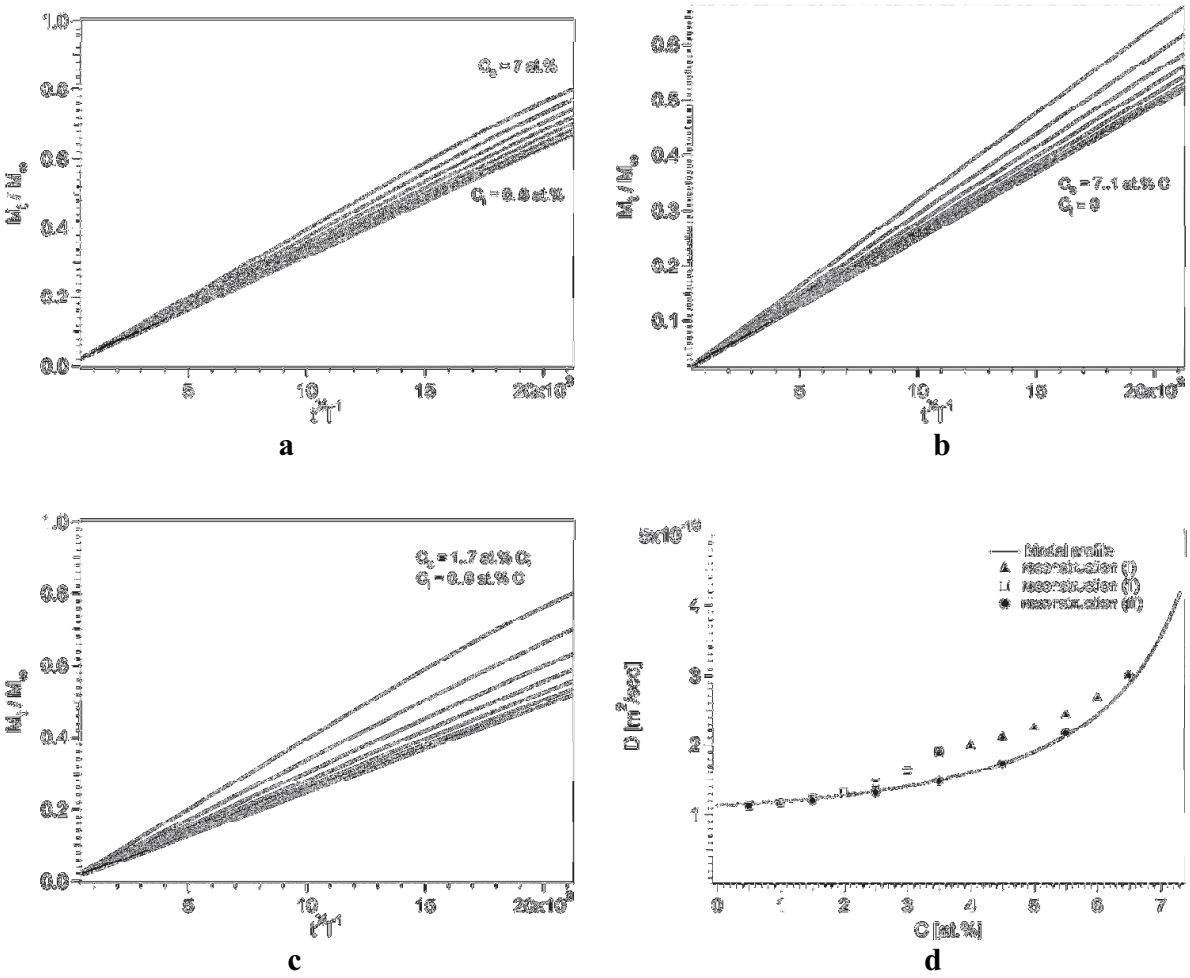

Figure 1: Simulated sorption curves for C in iron at 1400 K for cases a) i, b) ii and c) iii (see text). D) Evaluated diffusion coefficients from applying the initial rate method to the sorption curves in a)-c) are compared to composition dependent coefficient used as input data for the simulated sorption curves.

Simulation of thermogravimetric sorption curves and reconstruction of composition dependent diffusivity of carbon in expanded austenite

Thermogravimetric sorption curves of carbon during carburizing of iron were simulated by solving Fick's second law and adopting a concentration dependent diffusivity of carbon in austenite. For the computational details see [10]. To the sorption curves the initial rate method was applied to evaluate the (presumed constant) carbon diffusivity in various composition ranges, in order to simulate the determination of the composition dependence of the diffusivity of carbon. Three different cases were investigated:

i. the surface concentration was held constant at 7 at.% C and the starting concentration of carbon in the slab was stepwisely increased by 1 at.% C in each step.
ii. a series of slabs with initially no carbon were combined with surface concentrations ranging from 1 to 7 at.% C.
iii. the maximum difference between C_s and C_0 was taken as 1 at.% C and the composition range was stepwisely changed from C_s=1 to C_s=7 at. % with a stepsize of 1 at. %.

In the simulations the concentration dependent diffusivity of carbon in austenitic slabs with a thickness of $2e10^{-3}$ m was taken as that determined for Fe-C austenite at 1400 K [11]. The sorption curves for these cases are given in Fig.1a-c. The composition dependent diffusivity of C in austenite used as input data in the simulations is compared with the values for $\overline{D_C}$ $((C_s + C_0)/2)$ derived with the initial rate method from the sorption curves. Obviously, an excellent agreement is obtained for case iii, whereas cases i and ii yield carbon diffusivities which deviate the more from the input data the larger the composition range used for the sorption curve.

Experimental

Thin foils of stainless steel AISI 316, with thickness 7.5 um were used for carburizing. The composition of the steel is given in Table 1. Gaseous carburizing was performed in a Netzsch 449C simultaneous thermal analyzer, which allows simultaneous thermogravimetric analysis (TGA) and differential thermal analysis (DTA). The thin foils were austenitized by heating to 1353 K at a heating rate of 20 K/s in pure H_2 followed by immediate cooling to fully transform all deformation induced martensite, originating from cold rolling, into austenite. After austenitization the passive oxide film covering the stainless steel surface was electrochemically replaced by a thin Ni-deposit in a Woods nickel bath, consisting of $NiCl_2$, $NiSO_4$ and H_2SO_4. The thickness of the deposited Ni layer was in the order of 20 nm and contributes to maximally 0.5 % of the total sample mass. The solubility of carbon in the deposited Ni layer is negligible compared to the solubility in austenite. The foils were heated to a carburizing temperature of 793 K in pure H_2. Upon reaching the carburizing temperature, the gas composition was changed to a mixture of 20% CO and 80% H_2. Carburizing was continued until the weight gain of the sample corresponded to approximately 1.9 at.%. Subsequently the gas composition was changed to pure H_2 for 30 min as to redistribute the absorbed carbon atoms over the entire thickness of the foil. The homogenization time was estimated with the model in [9] using the anticipated value for the diffusion coefficients to be determined in the present work, i.e. 4e-16 m^2/s. The cycle of boost carburizing and homogenization of the carbon profile was repeated until a total mass gain corresponding to ca. 16 at.% carbon was reached.

Table 1. Composition of stainless steel AISI 316 in atomic %.

Alloy	Cr	Ni	Mo	Mn	Si	Fe
AISI 316	19.11	12.70	1.40	1.74	1.45	63.60

Results and Discussion

During the sorption experiment nine carburizing steps were realized. All carbon sorption curves determined at 793 K are presented in Fig. 2a. The values for D determined from the sorption curves are given Fig. 2b for various average carbon contents in the foils.

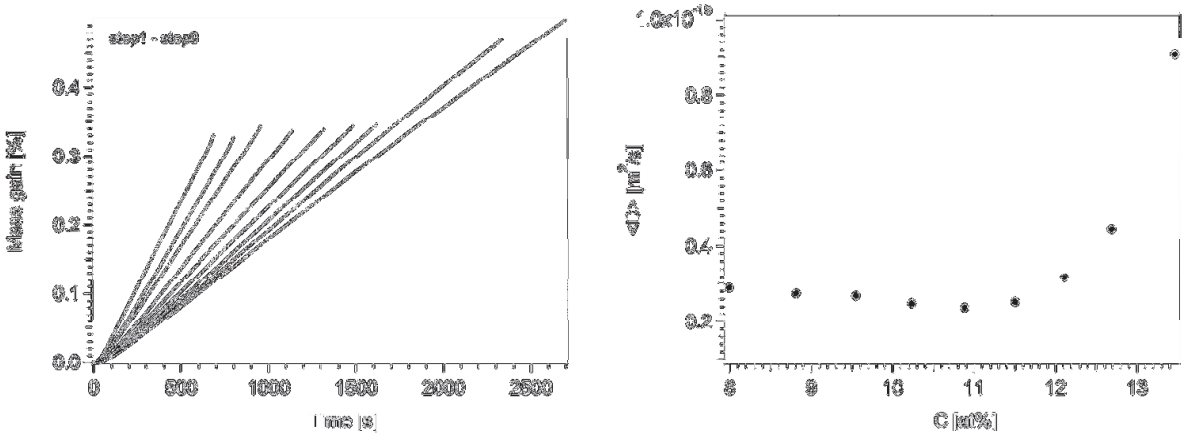

a **b**

Fig. 2. a) Initial part of sorption curves obtained during carburizing in CO-H_2. Each sorption stage was succeeded by a homogenization stage in H_2 before the next carburizing stage. b)Weighted-diffusion coefficients (cf. Eq.(2)) of carbon in 316 stainless steel at 793 K obtained from the initial rates of carburizing (method i).

The applicability of the method presented in Section 2 relies on the presumption that diffusion controlled kinetics prevail during carburization, i.e. local equilibrium between the gas phase and the solid state is obtained instantaneously upon changing the gas composition. The sorption curves show that a linear relationship between M_t/M_{inf} and $t^{1/2}/l$ is obtained shortly after adjusting the gas composition (at t=0), which suggests that fast local equilibrium at the surface is obtained indeed. This would be expected since the heterogeneous water shift reaction occurring at the catalyzing Ni-surface and providing C to the sample is known to proceed fast [12]. If surface kinetics would (partially) govern the carbon uptake, the diffusion coefficient will be underestimated. The slight decrease of the diffusion coefficients in the composition range 8-11 at. % might indicate that some influence of the surface kinetics on the carbon uptake cannot be neglected.

Strictly speaking the temperature ranges used in the simulations in section 2 and the experiments described in section 3 are incompatible and consequently the diffusivities in Fig. 1d and Fig. 2b differ by a factor 10^6. In this respect it should be mentioned that the thickness of the slab in the simulations (2 mm) and the thickness of the foils used in the experiments (7.5 µm) differ accordingly. Hence, the assumption lying at the basis of Eq. 1 is justified in both the simulations and in the experimental part. Then the conclusions drawn from the simulations in section 2 have general validity, despite incompatible temperature ranges in simulations and experiments. As compared to the simulations in section 2, the method pursued in the experimental part will provide an overestimation of the diffusivity of carbon in expanded austenite.

The obtained values for the diffusion constant are compared to the very few reported literature values. In Fig. 1d (model profile) diffusion data of carbon in austenite at high temperatures is depicted [11]. Generally, the same trend in composition dependence is observed in Fig. 1d and Fig. 2b. Similarly diffusion of nitrogen in expanded austenite shows similar trends, i.e. the diffusivity increases with the interstitial content in expanded austenite [13]. The dissolution of carbon (or nitrogen) atoms in the octahedral interstices of the f.c.c. lattice causes an isotropic expansion of the lattice. Accordingly the distance between the metal atoms in the closed packed lattice will increase

thereby lowering the activation energy for migration of C atoms from one octahedral interstice to a tetrahedral interstice, which is considered the activated state of interstitial diffusion in an f.c.c. lattice. Consequently, the diffusion coefficient increases with the carbon content in the lattice.

Conclusion

Three methods for the determination of composition dependent diffusion coefficients by measuring the initial rate of sorption were analyzed by simulation of the sorption behavior at high temperature. The simulations revealed that the best approximation of the composition dependent diffusivity is obtained for an incremental sorption method, in which the surface composition is successively increased by small increments and where the each increment is preceded by a homogenization of the carbon profile in the sample.

The presented experimental results indicate that the diffusion coefficient of carbon in expanded austenite increases with carbon concentration, in agreement with trends observed in the literature for diffusion of carbon in Fe-C austenite and the diffusion of nitrogen in expanded austenite.

Acknowledgement

Financial support of the Danish Research Council for Technology and Production Sciences under grants 274-05-0230 and 274-05-0367 is gratefully acknowledged.

References

[1] Y. Sun: Materials Processing Technology Vol. 168 (2005), p. 189.
[2] Y. Cao, F. Ernst, G.M. Michal: Acta Materialia Vol. 51 (2003), p. 4171.
[3] T. Christiansen, M.A.J. Somers: Surface Engineering Vol. 21 (5-6) (2005), p. 445.
[4] H.J. Grabke, I. Wolf: Materials Science and Engineering Vol. 87 (1987), p. 23.
[5] H.J. Grabke: Materials and Corrosion Vol. 54 (2003) No10.
[6] P. Szakálos, M. Lundberg, R. Petterson: Corrosion Science Vol. 48 (2006), p. 1679.
[7] Strauss, Krajak, Grabke: Materials and Corrosion Vol. 50 (1999), p. 622.
[8] M.A.J. Somers, T. Christiansen, P. Møller: Case hardening of stainless steel Danish Patent DK174707 B1 and PCT/DK03/00497.
[9] J. Crank: *The Mathematics of Diffusion* (Oxford University Press, Ely House, London W, 1970)
[10] T. Christiansen, K.V. Dahl, M.A.J. Somers: Defect and Diffusion Forum Vol. 258-260 (2006) p. 378.
[11] C.Wells, W. Batz, R. F. Mehl: Journal of Metals Vol. 188 (1950), p. 533.
[12] W. Erley, H. Wagner: Surface Science, Vol. 74 (1978), p. 333.
[13] T. Christiansen, M.A.J. Somers: Determination of concentration dependent diffusion coefficients of nitrogen in expanded austenite, to be published.

DTU Mechanical Engineering
Section of Solid Mechanics
Technical University of Denmark

Nils Koppels Allé, Bld. 404
DK- 2800 Kgs. Lyngby
Denmark
Phone (+45) 45 25 42 50
Fax (+45) 45 93 14 75
www.mek.dtu.dk
ISBN: 978-87-90416-28-7

DCAMM
Danish Center for Applied Mathematics and Mechanics

Nils Koppels Allé, Bld. 404
DK-2800 Kgs. Lyngby
Denmark
Phone (+45) 4525 4250
Fax (+45) 4593 1475
www.dcamm.dk
ISSN: 0903-1685